The Dissertation Committee for Tejas Umesh Kulkarni
certifies that this is the approved version of the following dissertation:

Evolution of reactive surfaces in turbulent flows

Committee:

Fabrizio Bisetti, Supervisor

Noel Clemens

David Goldstein

Robert Moser

Evolution of reactive surfaces in turbulent flows

by

Tejas Umesh Kulkarni

DISSERTATION

Presented to the Faculty of the Graduate School of

The University of Texas at Austin

in Partial Fulfillment

of the Requirements

for the Degree of

DOCTOR OF PHILOSOPHY

THE UNIVERSITY OF TEXAS AT AUSTIN

December 2021

Dedicated to my parents and my brother

Acknowledgments

This dissertation would not have been possible without the support of several people who I wish to thank.

First, I wish to express my sincere gratitude to my advisor Dr. Fabrizio Bisetti for his guidance during my graduate studies and research. Regular interactions with him over the past five years helped me develop research etiquette and shape my scientific judgment. I would like to thank my dissertation committee members, Prof. Noel Clemens, Prof. David Goldstein and Prof. Robert Moser. Their valuable feedback certainly helped me improve my dissertation.

I had the privilege to interact with some brilliant and helpful peers. I was fortunate to work closely and be motored by two exceptional post-doctoral researchers, Dr. Houssem Kasbaoui and Dr. Aurélie Bellemans. I thank my fellow graduate students Alfredo Duarte-Gomez, Evrim Solmaz, Mitchell Hollander, Stefano Luca, and others, for their help. In particular, I acknowledge the contributions of Aditya Vinod and Nicholas Deak in my success by serving as a test audience to all my technical presentations and as internal reviewers for my manuscripts. I would also like to sincerely thank Tina Woods, Geetha Rajagopal, Scott Messec, and the ASE staff for their support during my graduate studies.

This research was funded by the National Science Foundation (NSF) grant # 1805921. The direct numerical simulations used in this research were conducted on `Stampede2` supercomputer at the Texas Advanced Computing Center (TACC) and on `Shaheen` supercomputer at the King Abdullah University of Science and Technology (KAUST), Saudi Arabia. I am grateful to the NSF for their funding support and to TACC and KAUST Scientific Laboratory (KSL) for allowing me to use their computational resources.

Finally, I want to thank my family and friends for their support and love throughout my graduate studies. My parents encouraged me to pursue doctoral degree and kept me focused on completing my dissertation in time.

Evolution of reactive surfaces in turbulent flows

Publication No. _____

Tejas Umesh Kulkarni, Ph.D.
The University of Texas at Austin, 2021

Supervisor: Fabrizio Bisetti

The growth of reactive surfaces in turbulent flows is of intrinsic interest to turbulent premixed combustion modeling. In the regimes of turbulent combustion relevant to technological flows, the global fuel burning rate is directly proportional to the area of the propagating reactive front. This dissertation aims to investigate the growth rate of the area of reactive surfaces in unsteady flow configurations and identify its functional dependence on various parameters, particularly the Reynolds number.

First, a canonical flow configuration of spherical turbulent premixed flame in decaying isotropic turbulence is considered. A mathematical framework based on the flame surface density function is developed to analyze a database of large-scale direct numerical simulations. The surface area enhancement through turbulent wrinkling is found to be proportional to the product of the thickness of the turbulent flame brush; a region of space where the flame is found over repeated experiments, and the peak flame surface den-

sity within the brush. Both these quantities are studied in detail through their evolution equation derived within the proposed framework.

Subsequently, the analysis is extended to the investigation of a more realistic flow configuration of the swirling von-Kármán flow device. The device consists of a set of counter-rotating impellers that generate intense turbulence through mean shear. In particular, the Reynolds number dependence of the evolution of large surfaces in shear-generated turbulence is addressed briefly.

Table of Contents

List of Tables

List of Figures

Chapter 1

Introduction

When two fluids of dissimilar thermo-physical properties interact, the transfer of mass, momentum, and heat takes place across a thin interface separating the two. The area of the interface determines the rate of the exchanges between the two fluids. The rate of growth of the area is thus critical for a quantitative investigation of the phenomena.

In turbulent flows, the prediction of the growth rate of an interface is complicated by the presence of turbulent motion consisting of a wide range of scales that contribute to stretching, folding, and wrinkling of the interface. Of particular interest to this dissertation is the evolution of diffusive-reactive surfaces in turbulence, i.e. interfaces representing propagating combustion fronts in premixed mixtures.

A propagating combustion front, commonly referred to as a 'flame', is a region of space where chemical reactions convert reactants into products. In most practically relevant flow conditions, the flame is assumed to be a thin interface separating the reactants and products, propagating into the reactants [87]. The interface is typically an iso-surface of the reaction progress variable, which refers to a normalized reactive scalar field that varies mono-

tonically from zero in the reactants to unity in the products.

The propagation of the iso-surface occurs in the direction of its normal with a characteristic speed referred to as the *displacement speed*. The displacement speed is set by the local balance between chemical reactions and diffusive transport [123].

The concept of a propagating surface lies at the basis of several closures for turbulent premixed combustion, such as the level set method [122, 87], the flame surface density [74, 92, 17], and the extended flame surface density formalism [119]. The quantitative characterization and understanding of the statistics of the flame surface area in relevant flame configurations are necessary to support the development of accurate modeling approaches and to the interpretation of experimental data also.

Turbulent premixed flames can be broadly classified into several regimes based on the ratios u'/S_L and l/δ_L of characteristic velocity and length scales of turbulence and the flame [12, 86]. Here u' and l refer to the root mean squared (RMS) velocity fluctuation and the integral length scale of turbulence, whereas S_L and δ_L refer to the unstretched laminar flame speed and the thickness of the flame, respectively. Technological combustion devices often feature high turbulence intensities compared to the laminar flame speed ($u'/S_L \gg 1$). High operating pressures also lead to a thin flame front compared to the device length scale ($l/\delta_L \gg 1$).

These conditions correspond to the 'flamelet regimes' wherein an en-

hancement of the burning rate arises from a proportional increase in the reactive front's surface area through turbulent wrinkling. The functional dependence of the turbulent flame speed S_T on relevant dimensionless groups such as u'/S_L, l/δ_L, and the Reynolds, Karlovitz, and Damköhler numbers is of great interest for efficient design of compact combustion devices. Here, the turbulent flame speed S_T is defined based on the total volumetric rate of consumption of fuel, normalized by a suitable reference area.

This dissertation addresses the question of evolution of the surface area of propagating reactive-diffusive fronts and its functional dependence on the Reynolds number through the flame surface density formalism. The flame surface density function is the expected flame surface area per unit volume and allows for a statistical treatment of the burning rate enhancement.

The investigation focuses on how *scale separation* affects the growth and development of the turbulent flame surface area. The terminology 'scale separation' refers to the distinguishing feature of a turbulent flow, whereby coherent motions in a turbulent flow are organized over a range length scales that widens with increasing Reynolds number [41]. The following questions motivate the work: Does scale separation, as parameterized by the Reynolds number, affect the burning rates of turbulent premixed flames? If so, what are the mechanisms?

The investigation considers two flow configurations. First, a canonical configuration of expanding turbulent spherical flames in decaying isotropic turbulence is considered. A database of carefully designed direct numerical

simulations is analyzed and a mathematical framework for analyzing the unsteady growth of the turbulent flame surface area is developed. The framework is then leveraged for the examination of a turbulent von Kármán flow device. Consequently, the effects of mean shear, inhomogeneous, and anisotropic turbulence on the evolution of surfaces are examined.

1.1 Literature review

1.1.1 Scaling of turbulent burning rates

Hydrodynamic theories of the turbulent wrinkling of the flame surface in flamelet regimes originate from the seminal work of Damköhler [28]. By approximating the wrinkled flame surface as a collection of conical structures, he proposed a linear relation $S_T \sim u'$ for thin flames.

With a more careful calculation of the surface area, Shelkin [99] proposed the modification $S_T/S_L \sim (1+b(u'/S_L)^2)^{1/2}$, where b is a constant of order unity. The modified expression correctly accounts for the limit $S_T/S_L \to 1$ at low intensities ($u'/S_L \to 0$). Pocheau [90] demonstrated later on that to satisfy the scale invariance of the influence of turbulence on flame surface the normalized burning rate must follow the general expression $S_T/S_L = (1 + (u'/S_L)^n)^{1/n}$. While S_T/S_L is commonly assumed to depend on u'/S_L, recent experimental evidence points to a far more complex dependence on various dimensionless groups, in particular the Reynolds number.

Liu *et. al.* [67] investigated the dependence of turbulent flame speeds in pressurized premixed methane/air mixtures propagating in homogeneous

isotropic turbulence up to $\mathrm{Re}_\lambda \approx 100$. The Taylor Reynolds number $\mathrm{Re}_\lambda = u'\lambda/\nu$ is defined based on the Taylor length scale $\lambda = u'(15\nu/\epsilon)^{1/2}$ and scales as $\mathrm{Re}_\lambda \sim \mathrm{Re}^{1/2}$, the large scale Reynolds number. By controlling independently u' and l (via fan speed) and the reactants' kinematic viscosity ν (via pressure), Liu *et. al.* [67] were able to measure burning rates for various values of u'/S_L, while holding Re_λ constant and experiments were repeated for several values of the Reynolds number. The turbulent flame speed S_T/S_L was found to increase with Reynolds number, remaining nearly constant as u'/S_L varied. Data across multiple experiments suggest that the Reynolds number, not u'/S_L, is the primary controlling parameter in spherical turbulent premixed flames.

Numerous experimental studies of turbulent spherical premixed flames at the University of Leeds postulated and explored the dependence of S_T/S_L from $\mathrm{Re} \sim u'l$ or $\mathrm{Re}_\lambda \sim u'\lambda$ [1, 2, 4], although this proposition was later deferred in favor of relating turbulent flame speeds to u'/S_L instead.

The Reynolds scaling of turbulent burning rates and the surface area is broadly observed in other geometries also. Kobayashi et. al. [57, 56] measured mean burning rates in pressurized Bunsen burners equipped with turbulence generating grids, finding increasing values of S_T/S_L for increasing pressures at constant values of u'/S_L. Since u'/S_L was held constant alongside the geometry of the burner and grids, giving a nearly constant integral scale l also, the increase in S_T/S_L may be due to the increase in Reynolds number brought by the decreasing kinematic viscosity with increasing pressure.

Moreover, support for the Reynolds number dependence of normalized

burning rates is found in Damköhler's theory for small scale turbulence [28, 87], whereby the normalized burning rate should scale as $(u'l)^{1/2} \sim \mathrm{Re}^{1/2}$. It is important to highlight that the argument put forth by Damköhler in support of the Reynolds scaling does not rely on scale separation as advanced in this work, rather on enhancements to flame propagation brought by turbulent transport of heat and mass ahead of the flame's reaction zone.

Further theoretical support for the dependence of turbulent burning rates on the Reynolds number was recently presented by Chaudhuri et. al. [20]. Starting from the spectral closure of the level-set equation [85], the authors proposed and later confirmed experimentally [21] a $\mathrm{Re}^{1/2}$ scaling for S_T/S_L in turbulent spherical premixed flames, where Re is based on the turbulent flame radius and the reactants' thermal diffusivity. Their experimental evidence in favor of a $\mathrm{Re}^{1/2}$ scaling includes measurements for a variety of reactive mixtures, pressures, and turbulence parameters.

1.1.2 Theoretical arguments for a Reynolds scaling

In this dissertation, theoretical arguments in support of the dependence of the turbulent flame speed S_T/S_L on the Reynolds number are made within the formalism of the surface density function. The surface density function (SDF) is a statistical measure of the area of the flame surface per unit volume.

For turbulent premixed flames, the SDF characterizes the statistics of the area of a wrinkled flame and overall burning rate. The turbulent flame brush is the region of space where the flame is most likely to be located and

the SDF is found to peak in the middle of the brush, decreasing rapidly on its periphery [33].

It can be shown that the mean area of a turbulent premixed flame is proportional to the product of the peak value of the SDF across the brush and the linear extent of the brush, or its thickness [17]. Thus, the surface area and burning rates may be increased by increasing the peak SDF or the brush thickness, or both. Both these quantities are studied in detail for developing spherical turbulent flames in Chap. 3 and Chap. 4, respectively.

The flame brush thickness is defined as the inverse of the peak gradient magnitude of the Reynolds-averaged progress variable. Since the thickness of the flame brush depends on the Reynolds-averaged field, the flame brush may be expected to depend primarily on the largest scales of turbulent fluid motion, the geometry of the flow, and boundary and initial conditions [62].

The relationship between the brush thickness and the integral scale of the flow becomes clear if Taylor's theory of turbulent diffusion of material points [109] is applied to the evolution of the turbulent flame brush thickness [64]. Within the confines of the analysis, the thickness scales with the integral length scale as verified experimentally and via direct numerical simulations of turbulent premixed flames [65].

The flame surface density function is the second quantity of interest to the argument that burning rates increase with increasing Reynolds number. When the flame surface is taken to coincide with a specific iso-surface of the

progress variable [92], the SDF obeys a transport equation [117, 113], which includes terms that describe turbulent transport by velocity fluctuations, transport by flame propagation, and production and destruction of flame surface by two processes, one kinematic and the other associated with flame propagation in the presence of curvature. Data from experiments and simulations suggest that the rates of flame surface production and destruction may be proportional to the inverse of the Kolmogorov time scale $\tau_\eta = (\nu/\epsilon)^{1/2}$ [70].

The kinematic mechanism applies to propagating and material surfaces alike as velocity gradients induce positive (stretch) and negative (compression) tangential strain on the surface. It is well known [8, 24] that tangential strain on surfaces is, on average, positive, so that surface elements in turbulent flows are preferentially stretched and flattened, leading to an increase in their area [43, 35, 44, 34, 107]. This result is connected with the statistics of the alignment of the principal eigenvectors of the velocity gradient tensor with the normal to the surface.

The surface normal is aligned preferentially with the eigenvector associated with the most compressive eigenvalue of the rate of strain tensor [114]. The alignment statistics and preferential stretching of surfaces are universal across diverse turbulent flows and occur even in Gaussian random velocity fields, i.e. surface stretching does not require the velocity field to be the solution to the Navier-Stokes equations [114]. Further, Attili & Bisetti [6] showed that the mixture fraction field displays the same alignment statistics in turbulent non-premixed jet flames as in many other isothermal turbulent flows with

or without mean shear [5, 98, 115, 120].

In homogeneous isotropic turbulence, the mean tangential stretch rate of infinitesimal material surface elements was shown to scale with the inverse of τ_η, independently of the Reynolds number [43]. The same Kolmogorov scaling was found to hold for the net rate of tangential strain of the surface of turbulent premixed jet flames over a range of Reynolds numbers [70], implying that the kinematic mechanism may also apply to surfaces in turbulent flows with density gradients and variable transport properties. Experiments with spherically expanding turbulent flames with varying density ratios, defined as the ratio between the density of the unburnt to burnt gases, demonstrated that turbulent flame speeds are not affected significantly by the density ratio [66], further supporting the conclusion that mechanisms of surface generation by stretch may be largely insensitive to density gradients.

The second mechanism contributing to the generation and destruction of flame surface requires propagation in the presence of curvature and the rate of change of the surface area is proportional to the product of the displacement speed and the curvature of the surface [17]. If a surface propagates in the normal direction with a speed relative to the local fluid velocity, then surface generation and destruction occur when the surface's curvature is not zero [17]. The propagative mechanism is responsible for the destruction of surface area on average as confirmed by recent data from direct numerical simulations of planar [82] and jet [70] turbulent premixed flames.

The scaling of the propagative term, which is proportional to the prod-

uct of the local flame curvature and displacement speed, is far from established, although data from simulations of turbulent premixed jet flames suggest that the net rate of destruction of flame surface by the propagative mechanism may be proportional to the inverse of the Kolmogorov time scale as well [70].

Numerical studies of the curvature of infinitesimal material surface elements showed that the first five moments of the probability density function of curvature scale with the Kolmogorov length scale to a very good approximation [42]. Support for a relation between curvature and the surface density function in turbulent flames was advanced by Huh et. al. [49], who argued that the peak value of the surface density function is proportional to the mean of the absolute value of the flame curvature and investigated such postulate via simulations of statistically stationary planar turbulent premixed flames. The mean magnitude of the curvature was shown to scale proportionally to the inverse of the Kolmogorov length scale in agreement with Girimaji [42]. Similar results for the statistics of curvature of propagating surfaces in isotropic turbulence were reported by Zheng et. al. [126] also. Despite the lack of a comprehensive theory, it appears reasonable to expect that the smallest scales of turbulence and their characteristic time are involved in the propagative mechanism.

If surface generation and destruction occur at the smallest scales of the flow, it is possible that the entire spectrum of turbulence contributes to the wrinkling, stretching, and folding of surfaces. Further support for this hypothesis comes from the fractal geometry of interfaces and scalar iso-surfaces in

turbulence [73, 106, 105]. Recent experiments focusing on the turbulent/non-turbulent (T/NT) interface in a turbulent boundary layer at high Reynolds number have shown conclusively that the T/NT interface is fractal with power-law behavior over nearly two decades in the inertial range [30]. Thus, the geometrical features of an interface embedded in a turbulent field reflect all motions of turbulence in the inertial range, down to a fractal cut-off length scale similar in size to the Kolmogorov length.

In summary, there is convincing evidence that the mean rate of stretch of a surface in turbulent flow scales with the inverse of the Kolmogorov time scale, so that, the smaller the Kolmogorov time scale, the higher the net rate of production of surface area. It is also likely that the greater the source term, the greater the values taken by the surface density function itself, although the contribution of the source term relative to those of the unsteady and convective terms is specific to the flow configuration and dependent on the location in the flame.

Based on the discussion above, the thickness of the brush of a turbulent premixed flame is found to scale proportionally to the integral scale of the flow, while there is evidence that rates of surface generation (and destruction) may increase as the dissipative scales of turbulence become smaller. Thus, it is certainly possible that the higher the Reynolds number and the broader the separation between the large and small scales of turbulence, the greater the value of the dimensionless product between the brush thickness and the peak SDF, leading to greater values of S_T/S_L and enhancement to the burning

rates. Then, an argument could be made on the dependence of the SDF, and of burning rates, on the Reynolds number, which is a measure of scale separation in a turbulent flow [41].

The remainder of this dissertation is organized as follows. The governing equations, mathematical models and parameters for the database of the direct numerical simulations (DNS) of spherical turbulent flames are described in Chap. 2. A framework for analyzing the DNS database based on the surface density formalism is developed and discussed in Sec. 2.4. In particular, the framework provides integral and differential equations for key quantities that describe the temporal evolution of spherical flames, such as burning rates, flame radius, flame surface area and turbulent flame brush thickness. In chapters 3 and 4, the evolution of turbulent flame brush thickness and peak flame surface density is considered and scaling laws for various mechanisms are discussed. Chapter 5 discusses the implications of these results on the evolution of flame surface area and its scaling with Reynolds number. Finally, Chap. 6 seeks to apply the scaling relations to a practically relevant flow configuration and analyzes the role of Reynolds number in development of reactive fronts. Prominent findings of the dissertation are included in Chap. 7, along with the author's recommendations for future work.

Chapter 2

Spherical turbulent flames in isotropic turbulence

To analyze the dependence of growth rate of the surface area of reactive-diffusive fronts on the flow Reynolds number, spherically expanding premixed turbulent flames in decaying isotropic turbulence are considered first. Spherical turbulent premixed flame is a canonical configuration in the experimental studies of turbulent premixed combustion [21, 36, 67, 96].

For the purpose of conducting numerical simulations and analyzing the growth of reactive surfaces, this configuration offers the following two advantages. Firstly, turbulence statistics are a function of time and radial distance from the center of the spherical flame only, so that ensemble averages are gathered over the polar and azimuthal angles at each instance in time. Secondly, in the absence of externally imposed mean shear, the statistical state of turbulence encountered by the propagating flame is characterized by the RMS velocity fluctuation u', integral length scale l, and kinematic viscosity

The content presented in this chapter has been originally published in the following article:

Kulkarni, T., Buttay, R., Kasbaoui, M., Attili, A., & Bisetti, F. (2021). Reynolds number scaling of burning rates in spherical turbulent premixed flames. Journal of Fluid Mechanics, 906, A2. https://doi.org/10.1017/jfm.2020.784

ν alone. Further, the Reynolds number based on the Taylor microscale Re_λ is a unique measure of the ratio of the integral length scale to other length scales in the turbulence kinetic energy spectrum.

2.1 Governing equations

The evolution of reactive flow in this configuration is described by reactive, multi-component Navier-Stokes equations, which are considered here in the limit of a low Mach number [112, 80]. The continuity and momentum conservation equations read

$$\frac{\partial \rho}{\partial t} + \nabla \cdot (\rho \mathbf{u}) = 0 \tag{2.1}$$

and

$$\rho \frac{\partial \mathbf{u}}{\partial t} + \rho \mathbf{u} \cdot \nabla \mathbf{u} = -\nabla \pi + \nabla \cdot \mathsf{T}, \tag{2.2}$$

where ρ denotes the fluid density, $\mathbf{u}$ the mass-averaged bulk velocity, and T the viscous shear stress tensor. The hydrodynamic pressure $\pi = \pi(\mathbf{x}, t)$ is assumed to be small compared to the background thermodynamic pressure $p = p(t)$.

The mixture density ρ is related to the thermodynamic pressure according to the equation of state for an ideal gas mixture,

$$p = \rho \mathcal{R} T / W, \tag{2.3}$$

where $\mathcal{R}$ is the universal gas constant, T the temperature and W the molar mass of the mixture.

The viscous shear stress tensor T in Eq. (2.2) is modeled with a Newtonian fluid model,

$$\mathsf{T} = \mu\left(\nabla\mathbf{u} + (\nabla\mathbf{u})^T\right) - \frac{2}{3}\mu(\nabla\cdot\mathbf{u})\mathsf{I}, \tag{2.4}$$

where $\nabla\mathbf{u}$ is the velocity gradient tensor, I the identity tensor and μ the mixture-averaged dynamic viscosity [121, 11].

The reactive mixture is comprised of M different species and their mass fractions Y_i $(i = 1, \cdots, M)$ obey the following transport equation

$$\rho\frac{\partial Y_i}{\partial t} + \rho\mathbf{u}\cdot\nabla Y_i = -\nabla\cdot(\rho Y_i\mathbf{V}_i) + \dot{\omega}_i, \tag{2.5}$$

where $\dot{\omega}_i$ is the net rate of production of species i due to chemical reactions and $\mathbf{V}_i$ the mass diffusion velocity.

Diffusive transport of species is modeled with the Hirschfelder-Curtiss approximation [47, 91], which reads

$$\mathbf{V}_i X_i = -\mathcal{D}_i\nabla X_i, \tag{2.6}$$

where

$$\mathcal{D}_i \equiv (1 - Y_i)\left(\sum_{\substack{j=1\\ j\neq i}}^{M} X_j/\mathcal{D}_{ij}\right)^{-1} \tag{2.7}$$

is the species diffusion coefficient and X_i the mole fraction of i^{th} species. In the equation above, D_{ij} denote the binary diffusion coefficients for distinct pairs of species.

With this approximation, the closure for species diffusion velocity reads

$$\rho \mathbf{V}_i = -\rho D_i \frac{Y_i}{X_i} \nabla X_i = -\rho D_i \frac{\nabla (W Y_i)}{W}. \tag{2.8}$$

This approximation of species diffusion velocity is complemented by a small correction velocity $\mathbf{u}^c$ in the convective term in order to ensure total mass conservation. The final equations for species mass fractions read

$$\frac{\partial \rho Y_i}{\partial t} + \nabla \cdot (\rho Y_i (\mathbf{u} + \mathbf{u}^c)) = -\nabla \cdot (\rho Y_i \mathbf{V}_i) + \dot{\omega}_i, \tag{2.9}$$

where the correction velocity $\mathbf{u}^c$ is given by

$$\mathbf{u}^c \equiv -\sum_{i=1}^{M} Y_i \mathbf{V}_i = \sum_{i=1}^{M} \mathcal{D}_i Y_i \frac{\nabla W}{W} + \sum_{i=1}^{M} \mathcal{D}_i \nabla Y_i. \tag{2.10}$$

The equation for the conservation of enthalpy is manipulated into a differential equation for temperature, which reads

$$\rho c_p \frac{\partial T}{\partial t} + \rho c_p \mathbf{u} \cdot \nabla T = \frac{dp}{dt} + \nabla \cdot (\Lambda \nabla T) - \sum_{i=1}^{M} c_{p,i} \rho_i \mathbf{V}_i \cdot \nabla T - \sum_{i=1}^{M} h_i \dot{\omega}_i. \tag{2.11}$$

The equation above assumes that viscous heating is negligible on account of the low speed of the fluid and the fact that the pressure field p is spatially homogeneous.

The thermal conductivity Λ is evaluated with a mixture-averaged approach [76]. The specific enthalpy $h_i = h_i(T)$ and specific heat at constant pressure $c_{p,i} = c_{p,i}(T)$ for species i are evaluated from NASA tables [78].

Closure for chemical reaction terms $\dot{\omega}_i$ is provided by a skeletal chemical kinetics mechanism featuring 16 species and 73 elementary reactions of

Arrhenius type [69]. The skeletal mechanism was obtained from GRI-mech 3.0 [104] and reduces the computational costs significantly while modeling key mixture properties such as ignition delay time, laminar flame speed and thickness accurately.

Since the flow configuration is a closed vessel of a constant volume V, the background pressure $p(t)$ evolves so that the total mass m in the domain is constant:

$$p = \left(\int_V \frac{W}{T} \, dV \right)^{-1} m\mathcal{R}. \tag{2.12}$$

2.1.1 Numerical methods

Equations (2.1), (2.2), (2.9) and (2.11) are integrated in time with finite difference solver 'NGA' [32] on a homogeneous Cartesian grid.

The convective and viscous terms in the momentum equation are discretized with second-order centered finite difference formulas on a staggered grid. Mass conservation is enforced by solving a Poisson equation for the hydrodynamic pressure π instead of solving the continuity equation. The discrete form of the pressure equation is obtained using second order accurate finite difference formulas and solved with library HYPRE [37]. In particular, the preconditioned conjugate gradient (PCG) iterative solver is used along with the parallel alternating semi-coarsening multi-grid preconditioner (PFMG).

The advancement in time of the governing equations follows an operator splitting approach [89]. The momentum and pressure equations are coupled

with a pressure correction method [22]. The momentum equation is integrated in time with a semi-implicit method featuring the explicit second-order Adam-Bashforth scheme for convective terms and the implicit Crank-Nicolson method for linear viscous terms [55]. The linear system ensuing from the viscous terms is solved in a factored form with the alternating-direction implicit (ADI) method [83].

The third-order weighted essentially non-oscillatory (WENO) scheme of Liu et. al. [68] is employed for the convective terms in the scalar equations. The time advancement of temperature and species mass fractions is performed with a first-order Lie splitting approach, in which the integration of the convective and diffusive terms is performed first for each scalar field independently. Next, the reactive source terms are handled at each grid point with adaptive backward difference formulas through the CVODE solver [45]. The temporal integration of the scalar equations is semi-implicit, with the convective terms treated explicitly and the linear diffusive terms with implicit Crank-Nicolson method and ADI factorization.

All governing equations are coupled together with an outer iteration loop and convergence is found to be adequate after two iterations. The Cartesian grid is homogeneous and isotropic with spacing $\Delta = 20$ μm and a constant time step of $\Delta t = 0.2$ μs is taken. The spatial and temporal resolutions are adequate, since $\eta/\Delta \geq 0.5$ and $\tau_\eta/\Delta t \geq 20$, where η and τ_η denote the Kolmogorov length and time scale, respectively. Moreover, $\delta_L/\Delta \geq 5.5$, where δ_L is the thermal thickness of laminar flame. Extensive numerical tests to con-

firm the adequacy of spatial resolution of the reactive front were carried out elsewhere for turbulent premixed jet flames [69] for the same mixture.

2.2 Database of Direct Numerical Simulations

The spherical turbulent flame configuration consists of a cubic box filled with a premixed mixture of reactants and initialized with homogeneous isotropic turbulence at the target Taylor Reynolds number Re_λ. A spherical kernel of burnt gases is initialized at the center of the computational domain and ensuing turbulent premixed flame propagates radially outwards into the reactants, where turbulence decays freely. Periodic boundary conditions are imposed in all three directions so that the configuration represents a closed cubic domain. Figure 2.1 shows a schematic representation of the flame configuration.

As the reactants are converted to the products, the thermodynamic pressure $p = p(t)$ increases in time. The compression of reactants and products is isentropic since effects of radiation and viscous heating are ignored.

The reactants are a fully premixed lean mixture of methane and air with an equivalence ratio equal to 0.7 and are initialized at an elevated temperature $T_{u,0} = 800$ K and pressure $p_0 = 4$ atm. The thermo-chemical conditions were chosen to control certain dimensionless groups that determine the regime of turbulent premixed combustion, as discussed later.

At the chosen initial conditions for the reactants, the laminar flame

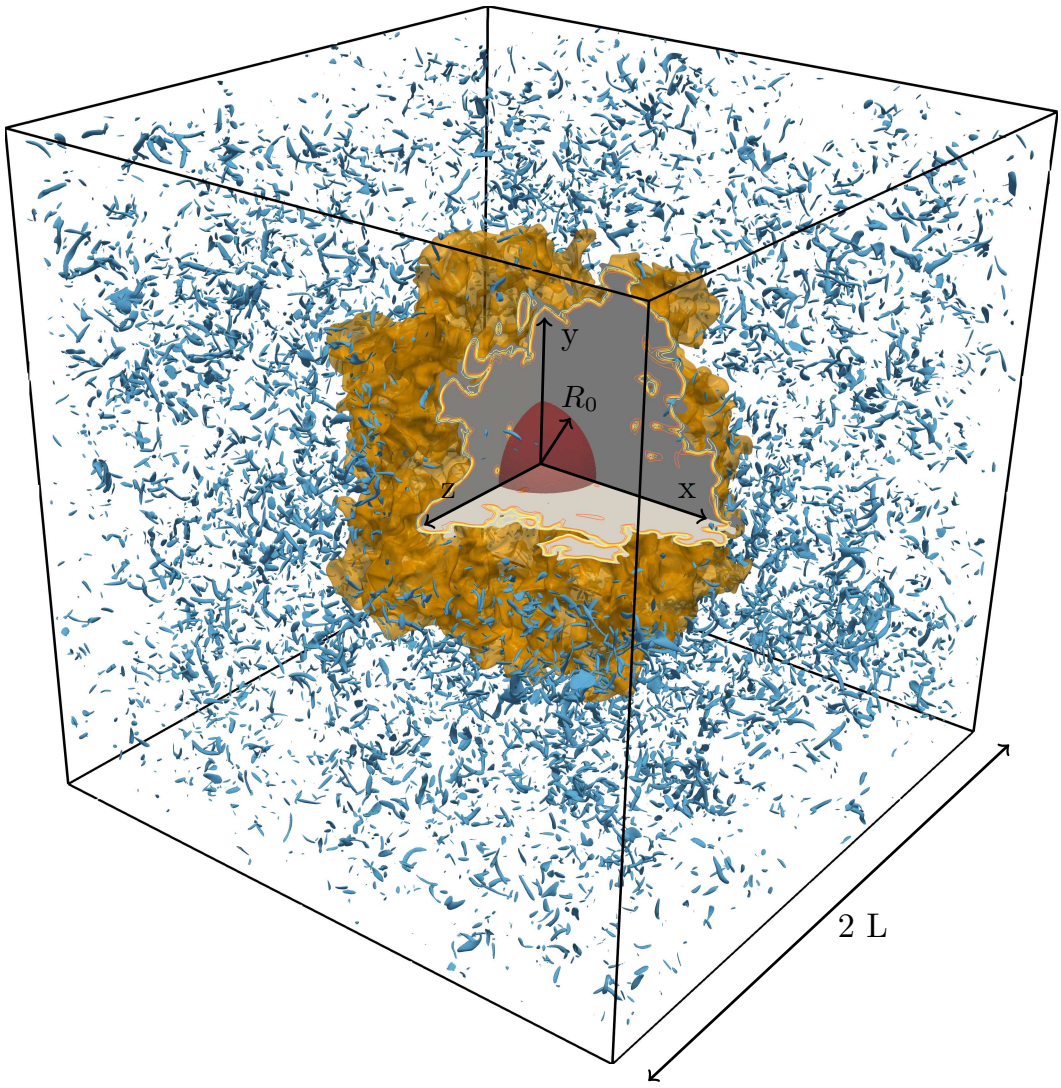

Figure 2.1: Turbulent spherical premixed flame in a cubic box of side $2L$ with periodic boundary conditions. The instantaneous flame surface (orange color) is surrounded by homogeneous isotropic turbulence, represented by iso-surfaces of vorticity (blue color). The flame surface is shown as a collection of iso-surfaces of reaction progress variable defined based on mass fraction of molecular oxygen (see Eq. (2.15)). The kernel of burnt gases at the onset of the simulation is shown as a sphere of radius R_0 in the cut-out (red color).

Name	N	$2R_L/l_0$	$2R_0/l_0$	u_0'/S_L	l_0/δ_L	δ_L/η	Re_λ	Ka	τ_0/τ_L
R1K1	512^3	33.8	6.9	7.4	3.4	11.3	44	25	0.69
R2K1	1024^3	43.8	6.7	8.5	5.2	11.3	59	25	0.91
R3K1	2048^3	59.4	6.3	9.8	7.8	11.5	77	25	1.18
R4K1	1728^3	68.9	6.9	12.1	12.1	11.2	102	25	1.62
R3K1s	1024^3	29.7	6.3	9.8	7.8	11.5	77	25	1.18
R3K2	1024^3	29.7	6.3	14.7	5.2	17.25	77	56	0.52
R2a	1024^3	36.7	6.7	7.4	6.3	9.65	59	18	1.29

Table 2.1: Turbulence parameters at the onset of the simulations. N is the number of grid points. The *effective* domain radius $R_L = 2(3/4\pi)^{1/3}L \approx 1.24L$ is defined based on L, half the length of the side of the cubic domain. The flame properties are $\delta_L = 0.11$ mm, $S_L = 1$ m s^{-1}, and $\tau_L = 0.11$ ms. The Karlovitz number is defined as $\mathrm{Ka} = \tau_L/\tau_\eta$.

speed is 1 m/sec and the thermal thickness is $\delta_L = (T_b - T_u)/\max\{|\nabla T|\} = 0.11$ mm. Here, T_u and T_b denote the temperature of reactants and products at the initial time and $\max\{|\nabla T|\}$ the maximum temperature gradient across the initialized laminar flame.

Table 2.1 lists relevant parameters for the direct numerical simulations in the database. A set of four primary simulations, denoted as 'R1K1', 'R2K1', 'R3K1' and 'R4K1' are designed at increasing Reynolds number $\mathrm{Re}_\lambda = u'\lambda/\nu$, where u' is the root mean squared (RMS) velocity fluctuation, λ the Taylor length scale and ν the kinematic viscosity of reactants.

While increasing the Reynolds number, the ratios of velocity scales u'/S_L and length scales l/δ_L are increased also so that the Karlovitz number $\mathrm{Ka} = \tau_L/\tau_\eta$ remains constant. The Karlovitz number is the ratio of the characteristic flame time scale $\tau_L = \delta_L/s_L$ and the Kolmogorov time scale τ_η and

broadly determines the regime of turbulent premixed combustion. Based on the Borghi-Peters regime classification [87], all flames in the primary set belong to the 'thin reaction zone' regime, where turbulence modifies the pre-heat zone of the flame front but not the reactive layer.

All characteristic scales of turbulence are evaluated in the reactants and change in time due to decay of turbulence. Velocity fluctuations are evaluated by subtracting the mean velocity field, which is obtained by averaging along spherical shells consistently with the symmetry of the configuration (see more discussion in Sec. 2.3.2).

The computational domain is a cube with side of length $2L$. The radius of a sphere with volume equal to that of the computational domain is denoted as $R_L = 2L(3/4\pi)^{1/3}$. It is apparent from Tab. 2.1 that the size of the computational domain is large compared to the integral scale l. For example, $2R_L/l_0 \geq 30$ for all flames. As a result, the extent of the domain is much larger than typically considered for DNS of isothermal homogeneous isotropic turbulence at the same Reynolds number.

Since the computational domain is large compared to the integral scale, the linear size of the spherical flame, i.e. its mean radial distance R from the center of the domain, may be initialized to be large compared to the integral scale. A rigorous definition for the mean radius R will be given later in this chapter. Since $R \geq l$ throughout the evolution of the flame, the flame is wrinkled by many turbulent eddies, the statistical averages computed from spherical shells converge due to the availability of a large number of statistically

independent samples, and the flame remains centered in the middle of the domain.

As articulated by Chaudhuri *et. al.* [20], if the integral scale is larger than the mean radius of a turbulent spherical flame, the flame radius acts as a cut-off scale, limiting the interaction between the flame and turbulence to scales smaller than itself. Thus, the fact that the flame is always large compared to the integral scale ensures that the entire turbulence spectrum interacts with the surface. In keeping with the requirement that the initial flame kernel radius R_0 be large compared to the integral scale, the ratio $2R_0/l \approx 7$ across different flame configurations. On the other hand, the domain size R_L/l varies slightly across configurations but is always large.

Apart from the set of four primary simulations, three additional supporting simulations, denoted by 'R2a', 'R3K1s' and 'R3K2' were conducted. Simulation R2a features the same initial Reynolds number as R2K1 while matching the turbulence intensity u'/S_L with flame R1K1. The flame R2a thus has a lower Karlovitz number than the others. Comparisons between flames R1K1, R2K1 and R2a help explore the dependence of turbulent burning rates on u'/S_L and Re_λ.

Similarly, flame R3K2 is conducted at same Reynolds number as R3K1 but a higher Karlovitz number by increasing u'/S_L and decreasing l/δ_L to keep the Reynolds number constant. Comparison of turbulent burning rates and other statistics of flame surface across the configuration pairs (R3K1, R3K2) and (R2K1, R2a) allows us to explore their dependence on the Karlovitz

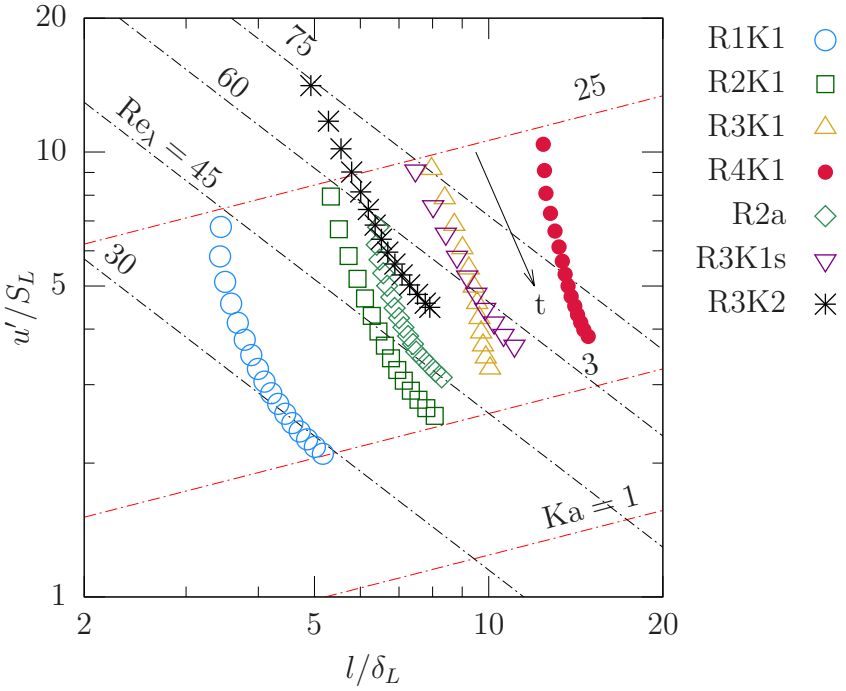

Figure 2.2: Borghi-Peters regime diagram [87] for all spherical turbulent flames. Temporal variation of quantities u'/S_L and l/δ_L is shown. Arrow points the direction of increasing time.

number.

Finally, in order to investigate the effect of domain size and pressure rise on propagation of turbulent flames, simulation R3K1 was repeated with a domain half its size and denoted by R3K1s. Comparison across flames R3K1 and R3K1s demonstrates that the domain size R_L/l does not have a noticeable effect on the statistics of flame surface, although the size does affect the mean radial velocity field induced by combustion as discussed in Sec. 2.3.2.

The temporal evolution of various dimensionless groups is presented on the Borghi-Peters regime diagram in Fig. 2.2. With time, the reactant side

turbulence decays and u'/S_L, Re_λ and Ka decrease while l/δ_L increases.

2.2.1 Flow-field initialization

The initial state of homogeneous isotropic turbulence (HIT) is obtained using a linear forcing scheme of Rosales & Meneveau [97]. The forcing scheme operates on the instantaneous velocity field through a fictitious body force field $\mathbf{g} = f\mathbf{u}$, which is added in the momentum equation. Here, $\mathbf{u}$ is the local velocity vector and f a parameter that may be controlled to achieve a desired Reynolds number.

Unlike spectral forcing schemes that add kinetic energy to a part of the range of wave-numbers of turbulence kinetic energy spectrum, the linear forcing scheme injects energy at all scales of turbulence. However, since the body force is proportional to the velocity itself, the kinetic energy addition is predominantly at large scales (small wave-numbers).

A statistically stationary turbulence is achieved when the mean rate of dissipation of turbulence kinetic energy ϵ matches the rate of injection, or

$$\epsilon = \overline{f\mathbf{u}\cdot\mathbf{u}} = f\overline{\mathbf{u}\cdot\mathbf{u}} = 3fu'^2, \tag{2.13}$$

where u' is the root-mean-squared (RMS) velocity fluctuation and the over-bar denotes a temporal average. Note that both ϵ and u' are temporally averaged statistics, as the balance of kinetic energy injection through forcing and dissipation is achieved only in the mean.

An empirical observation for stationary isotropic turbulence forced with

the linear forcing scheme is that the integral scale of turbulence $l = u'^3/\epsilon$ is always a fixed proportion of the domain size $\mathcal{L}$, $l/\mathcal{L} \approx 0.19$. Using $f = \epsilon/3u'^2$ and $l/\mathcal{L} = 0.19$, a relation between target Reynolds number $\mathrm{Re}_\lambda = u'\lambda/\nu$, where $\lambda = u'\sqrt{15\nu/\epsilon}$ is the Taylor scale, and the forcing parameter f is obtained as follows

$$\mathrm{Re}_\lambda = \left(\frac{45l^2 f}{\nu}\right)^{1/2} \approx 1.27456 \left(\frac{\mathcal{L}^2 f}{\nu}\right)^{1/2}. \tag{2.14}$$

For a given computational domain size and a target Reynolds number, the forcing parameter f is picked according to Eq. (2.14).

The ratios R_0/l of the initial kernel radius to the integral length scale and $\mathcal{L}/R_0$ of the domain size to the kernel radius are desired to be as large as possible. The former ensures that all scales of turbulent motion participate in wrinkling of flame surface from the onset [20] and also that a single simulation of a spherical turbulent flame contains a large number of independent realizations of turbulence-flame interactions. On the other hand, a large ratio $\mathcal{L}/R_0$ indicates that the initial flame kernel is small compared to the domain which allows for a large temporal observation window before boundary effects become significant.

Since the linear forcing strategy leads to $\mathcal{L}/l = (\mathcal{L}/R_0) \cdot (R_0/l) \approx 5$, both the ratios cannot be made large independently. To overcome this inherent limitation, first a statistically stationary state at the target Reynolds number was obtained on a smaller periodic domain and subsequently a number of statistically independent instances of the stationary turbulence were

concatenated in each direction to initiate the larger computational domain. In other words, the size of the computational domain $2L$ is much larger than $\mathcal{L}$, the size of a cube on which the target Reynolds number is forced through linear forcing scheme. Discontinuities in the concatenated velocity field were removed by advancing the flow field for $2\tau_\eta$ (twice the Kolmogorov time scale).

2.3 Basic characterization of spherical turbulent flames

The propagating flame surface is tracked as an iso-surface of the reaction progress variable C, which is defined as

$$C \equiv \frac{Y_{O_2} - Y_{O_2}^b}{Y_{O_2}^u - Y_{O_2}^b}, \tag{2.15}$$

where Y_{O_2} is the mass fraction of molecular oxygen and superscripts 'u' and 'b' denote its value in the unburnt and burnt mixtures, respectively. The progress variable increases monotonically from $C = 0$ in the reactants to $C = 1$ in the products. The iso-level $C = c^* = 0.73$ is taken to represent the flame surface. This particular value of the progress variable corresponds to the maximum value of heat release rate, thereby marking the middle of the reaction layer.

Figure 2.3 illustrates the evolution of the turbulent spherical premixed flames for flames R1K1, R2K1 and R3K1. The surface of the flame is visualized by the iso-surface $C(\mathbf{x}, t) = c^*$. The flame is initialized as a spherical kernel of products centered in the middle of the computational domain and propagates radially outwards into the premixed reactants.

It can be clearly seen that the flame surface is wrinkled and folded

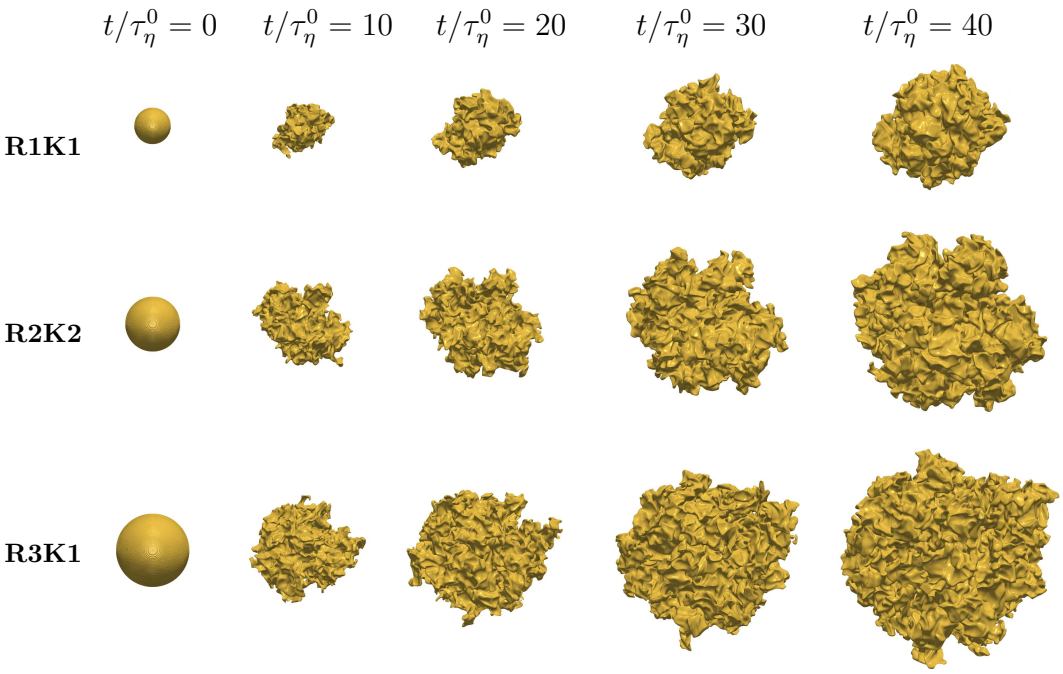

Figure 2.3: Evolution of flame kernels for flame configurations R1K1, R2K1 and R3K1. Four snapshots for each flame are presented at same dimensionless time t/τ_η^0.

by turbulence as the flame surface grows in size. Most patches of the surface are flat or posses only a slight curvature. Regions of high curvature are much less prevalent and are concentrated mainly in the regions of the flame surface ahead or behind the mean radial distance of the surface (the leading and trailing edges, respectively). These qualitative observations are consistent with established topological features of the surface of premixed turbulent flames [23].

If the flames are compared at times when they are of similar size, the

flame at the largest initial Reynolds number (R3K1) displays the highest density of folds and wrinkles, consistent with the qualitative interpretation that the range of scales of turbulent motion that wrinkle the flame surface widens with increasing Reynolds number.

2.3.1 Decay of turbulence

Upon the introduction of the kernel of burnt gases to initiate turbulent spherical flame, the reactant side turbulence is allowed to decay freely in the absence of numerical forcing. The turbulence kinetic energy k decays according to the power law [10, 9, 103]

$$k/k_0 = \left(1 + \frac{t}{t_0}\right)^{-n}, \tag{2.16}$$

where k_0 is the turbulence kinetic energy at the onset ($t = 0$), n the decay exponent and t_0 the virtual origin of the power-law decay.

The mean rate of dissipation of turbulence kinetic energy in the reactants follows the expression

$$\epsilon = -\frac{dk}{dt} = \frac{nk_0}{t_0}\left(1 + \frac{t}{t_0}\right)^{-n-1} \implies \epsilon/\epsilon_0 = \left(1 + \frac{t}{t_0}\right)^{-n-1}, \tag{2.17}$$

where $\epsilon_0 = nk_0/t_0$ is the initial value of the dissipation rate. As a result, the eddy turnover time $\tau = k/\epsilon$ increases linearly in time as

$$\tau = k/\epsilon = t/n + t_0/n. \tag{2.18}$$

The values of parameters n and t_0 for all flames are obtained from the least-squares linear fit to Eq. (2.18).

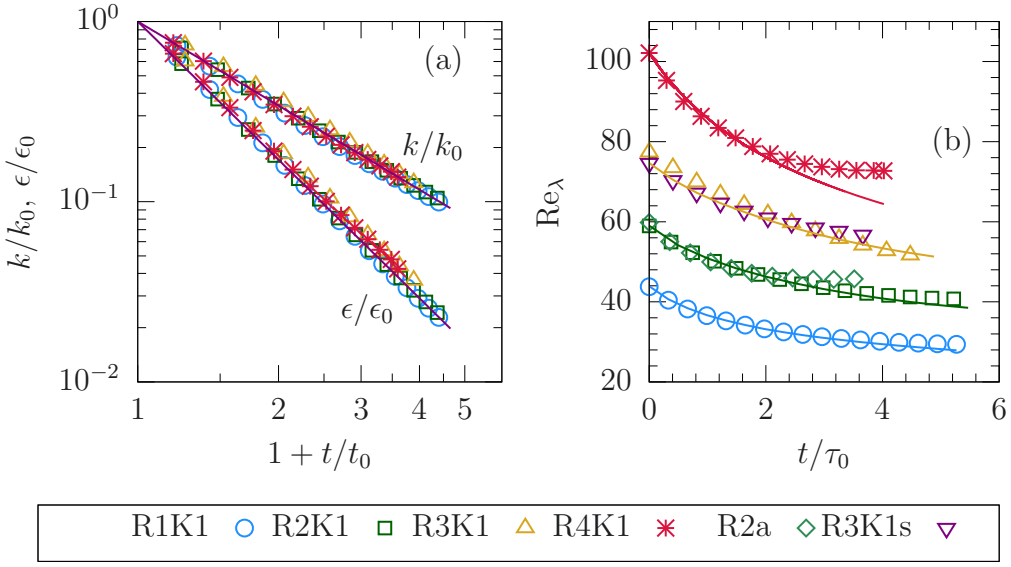

Figure 2.4: Statistics of the decaying isotropic turbulence in the reactants. (a) Power law decay of the turbulence kinetic energy k/k_0 and its mean rate of dissipation ϵ/ϵ_0 versus $1 + t/t_0$. Lines represent power law expression with $n = 1.55$. (b) Evolution of Taylor Reynolds number $\mathrm{Re}_\lambda = u'\lambda/\nu$.

Past experiments report values of the exponent n in the range 1.0 to 1.5. For decaying turbulence behind passive grids, Batchelor & Townsend [10] find $n = 1$, Comte-Bellot & Corrsin [25] report $1.16 \leq n \leq 1.37$, while Baines & Peterson [7] find a higher value of $n = 1.43$. Mohamed & Larue [79] report that $n = 1.25$ fitted their data best.

Figure 2.4(a) shows the fits and power laws for k/k_0 and ϵ/ϵ_0. A higher range of values for the decay exponent $1.55 \leq n \leq 1.78$ were found here for all turbulent spherical flames in the database. The discrepancy in the value of n may be due to low Reynolds number of the configurations or on the dependence of the exponent on the geometry, which differs between grid

generated turbulence and simulations of homogeneous isotropic turbulence.

Figure 2.4(b) compares the decay of Reynolds number in reactive and isothermal simulations from the same initial conditions. Statistics in the isothermal simulations are consistent with the power law decay, while for the the reactive simulations, the changes in background pressure and temperature cause minor deviations later on.

While the increase in pressure and temperature with time lead to modifications to the density and the viscosity of the mixture, they are minor on the account of the fact that the maximum pressure rise is less than 20% across all simulations. A significant deviation is only seen for flame R4K1 towards the end when changes to reactant viscosity are large due to a large increase in the temperature. The differences in Taylor Reynolds number between isothermal and reactive simulations may also be due in part to a decreasing number of samples available for statistics, since the reactants occupy a region that decreases in volume with time.

Since the data for flames R3K1 and R3K1s are approximately equal, it indicates that the size of the computational domain does not have a noticeable effect on the statistics of decaying turbulence with or without a propagating flame.

2.3.2 Spherical symmetry and statistical averaging

In the subsequent sections of this chapter, a statistical framework to analyze the growth of flame surface area is presented. The framework assumes

that all statistics are ergodic in the polar and azimuthal coordinates (denoted by Φ and Θ, respectively) and are averaged accordingly. Indeed, such symmetry is expected when the flame surface is far from the periodic boundaries. Verification of this assumption is critical to the analysis and is presented next in the context of the Reynolds-averaged radial velocity field.

Under the assumption of spherical symmetry of statistics, the Reynolds-averaged continuity equation reads

$$\frac{\partial \overline{\rho}}{\partial t} + \frac{1}{r^2}\frac{\partial r^2 \overline{\rho u_r}}{\partial r} = 0, \tag{2.19}$$

where $u_r = \mathbf{u} \cdot \hat{e}_r$ is the radial component of velocity and the turbulent mass flux $\overline{\rho u_r}$ is unclosed in general. Over-bar denotes the Reynolds average.

In the region occupied solely by reactants and products far away from the turbulent flame brush, density is spatially homogeneous and Eq. (2.19) simplifies to

$$\frac{1}{\rho}\frac{d\rho}{dt} + \frac{1}{r^2}\frac{\partial r^2 \overline{u}_r}{\partial r} = 0. \tag{2.20}$$

The reactants' and products' densities are taken to be functions of time alone due to compression and are not treated as random variables.

In absence of viscous heating and radiation terms in the Eq. (2.11), the gas compression in reactants and products is isentropic and the logarithmic rates of change of densities of reactants and products are related to the pressure as $\gamma d \ln \rho/dt = d \ln p/dt$, where γ is the ratio of specific heats. Substituting the isentropic relation in Eq. (2.20), the general solution for mean radial velocity

reads

$$\overline{u}_r = -\frac{1}{3\gamma}\frac{1}{p}\frac{dp}{dt}r + C_1 r^{-2}, \tag{2.21}$$

where C_1 is a constant that is determined by the boundary conditions.

In the region occupied by the products, the boundary condition $\overline{u}_r = 0$ at $r = 0$ leads to $C_1 = 0$ and the mean radial velocity is given by

$$\overline{u}_r = -\frac{1}{3\gamma_b}\frac{1}{p}\frac{dp}{dt}r, \tag{2.22}$$

where γ_b denotes the specific heat ratio in the burnt gases. Equation (2.22) indicates that $\overline{u}_r$ is negative since $dp/dt > 0$ and varies linearly with r in the region occupied by the products.

In the region occupied by the reactants, C_1 in Eq. (2.21) is determined by the condition $\overline{u}_r = 0$ at the domain boundary. However, the radial distance of the boundary depends on the polar and azimuthal coordinates since the domain is a cube. Yet, since the mean radial velocity decreases as $1/r^2$, the effect of cubic geometry on the mean radial velocity is negligible away from the boundary. Consequently, the boundary condition $\overline{u}_r = 0$ may be imposed at an *effective* radial distance $R_L = 2L(3/4\pi)^{1/3}$, which equals the radius of a spherical chamber with equal volume. The mean radial velocity in the reactants reads as

$$\overline{u}_r = -\frac{R_L}{3\gamma_u}\frac{1}{p}\frac{dp}{dt}\left[\frac{r}{R_L} - \left(\frac{r}{R_L}\right)^{-2}\right], \tag{2.23}$$

where γ_u is the ratio of specific heats of the reactants.

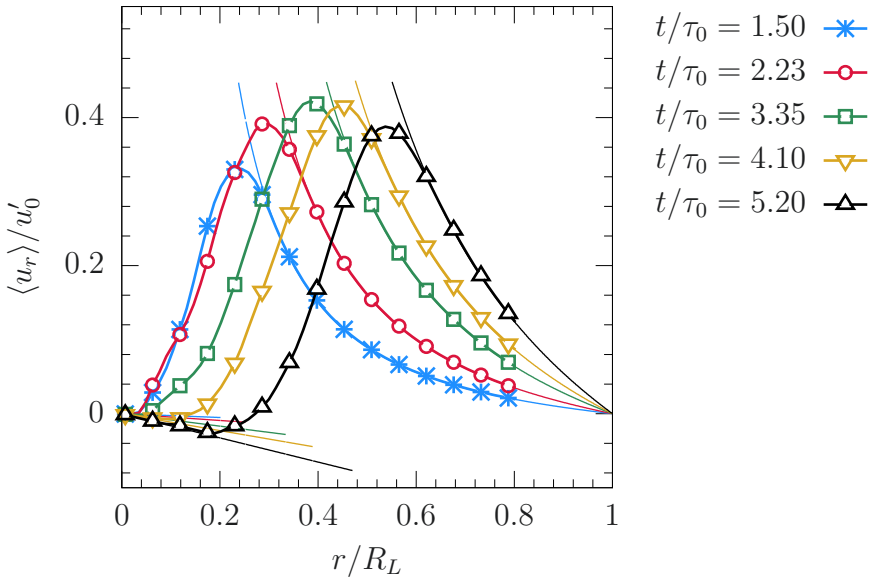

Figure 2.5: Reynolds-averaged radial velocity $\overline{u}_r$ normalized by the initial turbulence intensity for flame R2K1. Thin lines represent the expressions in Eq. (2.22) and Eq. (2.23) evaluated with the corresponding value of $d \ln p/dt$ from the DNS data. Data is compared for $r/R_L \leq 0.8$, which is the shortest distance from the center to the periodic boundary.

Figure 2.5 shows the Reynolds-averaged radial velocity $\overline{u}_r$ at five instants in time for flame R2K1. The mean is obtained by averaging over the polar and azimuthal angles and matches closely the expressions Eq. (2.22) and Eq. (2.23) in the products and reactants, respectively. In particular, the reactants' side comparison is identical up to $r/L = 1.0$ or $r/R_L = 0.8$, which corresponds to the minimum distance between the center and the faces of the cubic domain. In summary, the mean flow retains the spherical symmetry as if the computational domain were a spherical vessel of radius R_L.

It should be noted that the peak mean radial velocity within the brush

increases at first with time, but decreases later on. As the flame grows is size, the boundary condition causes the peak mean radial velocity to decrease due to confinement effects. Evidence for this statement comes from the following observations.

The evolution of peak mean radial velocity is qualitatively similar to that of the mean radial velocity at the leading edge of the brush, where Eq. (2.23) is applicable. While $(1/p)\,dp/dt$ increases continuously in time, the term inside the square brackets decreases as R/R_L increases, where R denotes the mean radial distance of the flame surface. The product of the two terms is non-monotonic in time and gives rise to the behavior seen in Fig. 2.5.

The conclusion is further supported by the observation that the non-monotonic trend of the peak mean radial velocity is seen for flame R3K1s but not for R3K1, where it increases continuously due to larger computational domain.

2.4 Framework for flame surface statistics

The evolution equation for reaction progress variable can be obtained from the species conservation equation and reads

$$\frac{\partial C}{\partial t} + \mathbf{u} \cdot \nabla C = \frac{1}{\rho} \nabla \cdot (\rho \mathbb{D} \nabla C) + \frac{\dot{\omega}_C}{\rho}, \tag{2.24}$$

where $\mathbb{D}$ and $\dot{\omega}_C$ denote the molecular diffusivity and the normalized reaction rate of molecular oxygen, respectively.

The reactive-diffusive equation for the progress variable is often cast into a kinematic equation of the form

$$\frac{\partial C}{\partial t} + (\mathbf{u} + S\mathbf{n}) \cdot \nabla C = 0, \tag{2.25}$$

where S is the displacement speed and $\mathbf{n}$ the normal vector. Adhering to the convention commonly found in the literature, the normal vector is defined as $\mathbf{n} = -\nabla C/|\nabla C|$ so that it points towards the reactants.

Comparing Eq. (2.24) with Eq. (2.25), the displacement speed S contains the contributions of reactions and molecular diffusion and is given by [92, 19]

$$S \equiv \frac{1}{|\nabla C|}\frac{DC}{Dt} = \frac{\dot{\omega}_C}{\rho|\nabla C|} + \frac{\mathbf{n} \cdot \nabla(\rho \mathbb{D} \mathbf{n} \cdot \nabla C)}{\rho|\nabla C|} - \mathbb{D}(\nabla \cdot \mathbf{n}). \tag{2.26}$$

In the equation above $D/Dt = \partial/\partial t + \mathbf{u} \cdot \nabla$ denotes the material derivative operator. Molecular diffusivity $\mathbb{D}$ was calculated as the binary diffusion coefficient of O_2 in N_2, the predominant species in the mixture.

The three contributions to the displacement speed S as written on the right hand side of eq. (2.26) are due to chemical reactions, molecular diffusion in the direction of the normal, and that in the tangential direction. In the present database the displacement speed is calculated as the material derivative since the reaction and molecular diffusion contributions are not available at the same time due to temporal operator splitting employed in the solver.

2.4.1 Turbulent burning velocity

While the laminar flame speed is a characteristic property of the reactant mixture and thermodynamic conditions, the turbulent burning velocity is strongly affected by the turbulence-flame interaction and differs significantly from the laminar flame speed [33].

The dimensionless turbulent burning velocity S_T/S_L is defined based on the mean volumetric fuel burning rate Ω_f and a suitable reference area A^*,

$$\frac{S_T}{S_L} = \frac{\Omega_f}{\rho_u Y_f S_L A^*}, \tag{2.27}$$

where ρ_u is the reactants' density, Y_f the mass fraction of fuel species in the reactants, and S_L the un-stretched laminar flame speed of the mixture.

The mean burning rate is $\Omega_f(t) = \left\langle \tilde{\Omega}_f(t) \right\rangle$, i.e. the statistical expectation of the instantaneous volumetric burning rate $\tilde{\Omega}_f(t)$ over repeated experiments. The angular brackets $\langle . \rangle$ denote the statistical expectation hereafter.

Similarly, the mean radial distance of the flame surface, $R(t) = \left\langle \tilde{R}(t) \right\rangle$ is termed as the flame radius henceforth. The reference area A^* is taken as $A^* = 4\pi R^2$, the area of a sphere with radius equal to the flame radius. Finally, the expectation of the turbulent flame surface area is $A(t) = \left\langle \tilde{A}(t) \right\rangle$, where $\tilde{A}(t)$ is the instantaneous flame surface area at time t.

Formal definitions of $R(t)$ and $A(t)$ are provided below in context of the flame surface density function. A comprehensive discussion on distinction

between statistical expectation and their instantaneous values in the context of spherical flames in included in Appendix A.

The burning rate enhancement as quantified by S_T/S_L may be attributed to two distinct effects in turbulent premixed flames. First, turbulent fluid motion wrinkles the flame surface, leading to a larger area over which chemical conversion from reactions to products takes place. Second, local burning rate per unit area may be modified on the account of enhanced transport of heat and radicals. The two effects are separated with the following decomposition:

$$\frac{S_T}{S_L} = \left(\frac{A}{A*}\right)\left(\frac{\Omega_f}{\rho_u Y_f S_L A}\right) = \chi \mathcal{I}. \tag{2.28}$$

Here, area ratio $\chi = A/A^*$ and correction factor $\mathcal{I} = \Omega_f/\rho_u Y_f S_L A$ quantify the enhancement of the surface area and local burning rate, respectively.

Figure 2.6 shows the normalized burning velocity S_T/S_L, the area ratio χ and the correction factor $\mathcal{I}$ for various flame configurations. The area ratio controls the dimensionless burning velocity S_T/S_L for the most part, while $\mathcal{I} \approx 1$ at all times for all flames. The area ratio is higher and grows faster in time for flames with higher Reynolds number. Also note that flame configurations with the same Reynolds number (pairs R2K1, R2a and R3K1, R3K1s) have largely similar growth of the surface area.

The analysis of growth of the flame surface area follows a novel approach that builds upon the concepts of flame surface density formalism. The proposed framework is discussed in the upcoming sections.

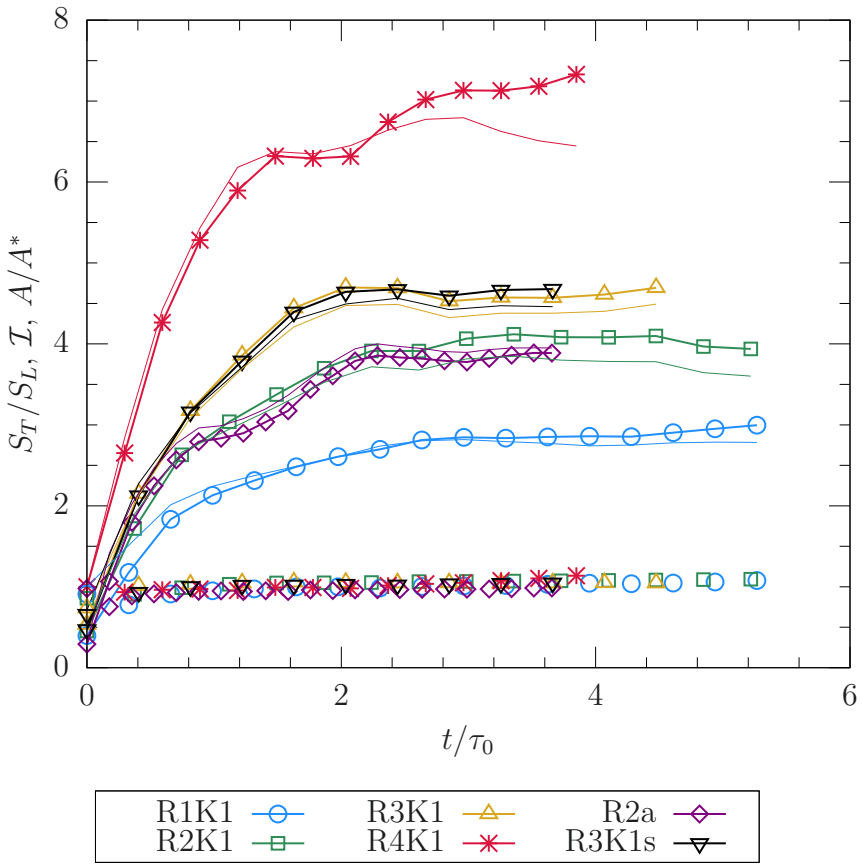

Figure 2.6: Temporal evolution of the normalized turbulent burning velocity S_T/S_L (thick lines with symbols), area ratio χ (thin lines) and the correction factor $\mathcal{I}$ (symbols only) for all flames. The area ratio explains most of the variation in S_T/S_L while $\mathcal{I} \approx 1$ at all times.

2.4.2 Surface density function

As defined in the preceding section, $\Omega_f(t)$, $R(t)$ and $A(t)$ are time-dependent statistical expectations of random processes $\tilde{\Omega}_f(t)$, $\tilde{R}(t)$ and $\tilde{A}(t)$, respectively. Suitable estimators for these expectations are defined in a manner consistent with the ergodicity of the flow within the mathematical framework of the flame surface density function.

The flame surface density function Σ is defined as the statistical expectation of the flame surface area per unit volume and implicitly defined as

$$A = \int_V \Sigma(\mathbf{x}, t)\, dV. \tag{2.29}$$

Since the flame surface area A is the expectation of that of the iso-level surface $C = c^*$, the surface density function is related to the progress variable C and its gradient. This can be seen as follows.

It can be shown that the gradient-weighted volume integral of any non-negative function $f(\mathbf{x}, t)$ equals the sum over all iso-surfaces $C = c$ of corresponding surface integrals [77, 58],

$$\int_V f(\mathbf{x}, t)|\nabla C|\, dV = \int_0^1 \oint_{A_c} f(\mathbf{x}, t)\, dA_c\, dc \tag{2.30}$$

Choosing the function $f(\mathbf{x}, t) = \delta(C(\mathbf{x}, t) - c^*)$ as the Dirac-delta function of the progress variable, the equation above reduces to

$$\int_V |\nabla C|\, \delta(C(\mathbf{x}, t) - c^*) = \int_0^1 \oint_{A_c} \delta(C - c^*) dA_c\, dc = \widetilde{A}, \tag{2.31}$$

where $\widetilde{A}$ is the surface area of iso-surface $C = c^*$ in a single realization.

The expectation of the surface area is then given by

$$A = \left\langle \widetilde{A} \right\rangle = \int_V \overline{|\nabla C| \delta(C - c^*)}\, dV \tag{2.32}$$

$$= \int_V \left\langle |\nabla C| \middle| C = c^* \right\rangle \mathcal{P}_C(C = c^*; \mathbf{x}, t)\, dV. \tag{2.33}$$

Here $\mathcal{P}_C$ denotes the probability density function (PDF) associated with the progress variable $C(\mathbf{x}, t)$, which is a random field.

Comparing Eq. (2.33) with Eq. (2.29), it can be seen that the surface density function is related to the gradient field with

$$\Sigma(C = c^*; \mathbf{x}, t) = \left\langle |\nabla C| \middle| C = c^* \right\rangle \mathcal{P}_C(C = c^*, \mathbf{x}, t). \tag{2.34}$$

For spherical flames, all statistics depend only on radial and time coordinates (r, t) only. The mean flame surface area A and flame radius R are given by

$$A(t) = \int_V \Sigma(\mathbf{x}, t)\, dV = 4\pi \int_0^\infty \Sigma(r, t) r^2\, dr \tag{2.35}$$

$$R(t) = \frac{1}{A(t)} \int_V ||\mathbf{x}|| \Sigma(\mathbf{x}, t)\, dV = \frac{4\pi}{A(t)} \int_0^\infty r^3 \Sigma\, dr, \tag{2.36}$$

since $||\mathbf{x}|| = r$. The area ratio χ can now be written in terms of Σ as

$$\chi = \frac{A}{4\pi R^2} = \int_0^\infty (r/R)^2 \Sigma(r, t)\, dr. \tag{2.37}$$

Finally, the mean volumetric fuel burning rate is simply

$$\Omega_f(t) = \int_V \langle \dot{\omega}_f(\mathbf{x}, t) \rangle\, dV, \tag{2.38}$$

where $\dot{\omega}_f(\mathbf{x}, t)$ is the instantaneous local rate of consumption of fuel per unit volume.

2.4.3 Probability density function of the radial distance of the flame surface

The analysis of the evolution of the area ratio χ and its scaling proceeds through a statistical description of the radial distribution of the flame surface. For spherical turbulent flames, the radial distance of the flame surface is a random variable, denoted henceforth as ϕ. The corresponding sample space variable is denoted as φ.

Cumulative density function (CDF) of ϕ is given by

$$\mathbb{P}(\phi < \varphi; t) = A_\varphi / A = A^{-1} \int_0^\varphi 4\pi r^2 \Sigma(r,t)\, dr, \tag{2.39}$$

where A_φ denotes the expectation of flame surface area contained within the sphere of radius φ.

Subsequently, the probability density function $\mathcal{P}$ of the radial distance is obtained by differentiating with respect to the sample space variable φ,

$$\mathcal{P}(\phi = \varphi; t) = d\mathbb{P}/d\varphi = \frac{4\pi\Sigma(\varphi,t)\varphi^2}{A(t)} \tag{2.40}$$

and has support $\varphi \in (0, \infty)$.

The mean μ and standard deviation σ of the PDF are related to the surface density function with

$$\mu = \int_0^\infty \varphi \mathcal{P}(\varphi,t)\, d\varphi = A^{-1} \int_0^\infty 4\pi r^3 \Sigma(r,t)\, dr = R(t) \tag{2.41}$$

and

$$\sigma^2 = \int_0^\infty (\varphi - R)^2 \mathcal{P}(\varphi,t)\, d\varphi = A^{-1} \int_0^\infty 4\pi r^2 (r-R)^2 \Sigma(r,t)\, dr. \tag{2.42}$$

If the PDF $\mathcal{P}$ is assumed to be a Gaussian, it can be shown that σ is re-scaled turbulent flame brush thickness,

$$\delta_T \equiv \left(\max\{|d\overline{C}/dr|\}\right)^{-1} \approx \sqrt{2\pi}\sigma, \tag{2.43}$$

where $\overline{C}$ is the mean progress variable and $d\overline{C}/dr$ its gradient.

The advantage of relating pertinent statistical measures to the PDF and the surface density function is that their temporal evolution is prescribed by ordinary differential equations. The evolution equation for $\mathcal{P}$ and its moments is derived starting from that for the flame surface density function next.

2.4.3.1 Transport equations

The flame surface density function Σ evolves according to [92, 113, 117]

$$\frac{\partial \Sigma}{\partial t} + \nabla \cdot \left(\langle \mathbf{u} + S\mathbf{n} \rangle_w \Sigma\right) = \langle K \rangle_w \Sigma, \tag{2.44}$$

where $\mathbf{u}$ and $\mathbf{n}$ denote the velocity and local flame normal vectors, respectively and K the flame stretch. The operator $\langle \cdot \rangle_w$ denotes a gradient-weighted or *surface average* [92], defined as

$$\langle Q \rangle_w \equiv \frac{\left\langle Q|\nabla C| \middle| C = c^* \right\rangle}{\left\langle |\nabla C| \middle| C = c^* \right\rangle}. \tag{2.45}$$

After making suitable simplifications due to spherical symmetry, the surface density transport equation reads

$$\frac{\partial \Sigma}{\partial t} + \frac{1}{r^2}\frac{\partial}{\partial r}(r^2 \langle u_r + Sn_r \rangle_w \Sigma) = \langle K \rangle_w \Sigma. \tag{2.46}$$

Here, S is the displacement speed as defined in (2.26) and $u_r = \mathbf{u} \cdot \hat{e}_r$ and $n_r = \mathbf{n} \cdot \hat{e}_r$ represent the radial components of the velocity and normal vectors, respectively.

The flame stretch $K = a - 2S\kappa$ contains two contributions: the *tangential strain rate* $a = -\mathbf{n}^T \nabla \mathbf{u} \mathbf{n} + \nabla \cdot \mathbf{u}$ and the *curvature-propagation term* $-2S\kappa = S\nabla \cdot \mathbf{n}$. The tangential strain rate depends only on the velocity field $\mathbf{u}$ and the orientation of the velocity gradient tensor $\nabla \mathbf{u}$ with respect to the flame normal $\mathbf{n}$.

On the other hand, the curvature-propagation term appears only for surfaces that propagate ($S \neq 0$) in the presence of non-zero surface curvature ($\kappa = -(\nabla \cdot \mathbf{n})/2 \neq 0$). In the case of a material surface, $K = a$ and surface stretch is due to tangential strain alone.

In light of Eq. (2.40), the time rate of change of $\mathcal{P}$ is given by

$$\frac{\partial \mathcal{P}}{\partial t} = \frac{4\pi\varphi^2}{A} \left[\frac{\partial \Sigma}{\partial t} - \frac{\Sigma}{A} \frac{dA}{dt} \right]. \tag{2.47}$$

The rate of change of the expected area A is obtained by integrating Eq. (2.46) throughout the entire volume,

$$\frac{dA}{dt} = -\int_0^\infty 4\pi \frac{\partial}{\partial r} \left(r^2 \left\langle u_r + S n_r \right\rangle_w \Sigma \right) \, dr + \int_0^\infty 4\pi r^2 \left\langle K \right\rangle_w \Sigma \, dr, \tag{2.48}$$

or,

$$\frac{1}{A} \frac{dA}{dt} = \int_0^\infty \left\langle K \right\rangle_w \mathcal{P} \, d\varphi \equiv K_G. \tag{2.49}$$

Since the volumetric integrals of the convective and propagation terms on the left hand side of Eq. (2.46) are zero the logarithmic time rate of change of the area is called the *global stretch* K_G.

Substituting $\partial\Sigma/\partial t$ from (2.46) and $1/A\, dA/dt$ from Eq. (2.49) into (2.47) and simplifying, the evolution equation for the PDF is obtained:

$$\frac{\partial \mathcal{P}}{\partial t} = -\frac{4\pi}{A}\frac{\partial}{\partial \varphi}\left(\varphi^2 \left\langle u_r + S n_r \right\rangle_w \Sigma\right) + \left\langle K \right\rangle_w \frac{4\pi\varphi}{A} - K_G \mathcal{P} \tag{2.50}$$

since $\mathcal{P} = 4\pi\varphi^2\Sigma/A$, the equation simplifies to

$$\partial\mathcal{P}/\partial t = -\partial/\partial\varphi\left\{\left\langle u_r + S n_r \right\rangle_w \mathcal{P}\right\} + (\left\langle K \right\rangle_w - K_G)\mathcal{P}. \tag{2.51}$$

Note that the *differential stretch* $\left\langle K' \right\rangle_w \equiv \left\langle K \right\rangle_w - K_G$ affects the time rate of change $d\mathcal{P}/dt$ and not the flame stretch $\left\langle K \right\rangle_w$ directly. In other words, a homogeneous flame stretch everywhere on the surface increases the flame surface area at the same rate everywhere and does not change how it is distributed in the radial direction.

In light of Eq. 2.41 and Eq. (2.51), the time rate of change of mean flame radius R is given by

$$\frac{dR}{dt} = \frac{d}{dt}\int_0^\infty \varphi\mathcal{P}\, d\varphi = \int_0^\infty \varphi\frac{\partial \mathcal{P}}{\partial t}\, d\varphi \tag{2.52}$$

$$= -\int_0^\infty \varphi\frac{\partial}{\partial\varphi}\left(\left\langle u_r + S n_r \right\rangle_w \mathcal{P}\right)\, d\varphi + \int_0^\infty \varphi \left\langle K' \right\rangle_w \mathcal{P}\, d\varphi. \tag{2.53}$$

Simplifying the equation using integration by parts, the equation reduces to

$$\frac{dR}{dt} = -\Big[\varphi \left\langle u_r + Sn_r \right\rangle_w \mathcal{P}\Big]_0^\infty + \int_0^\infty \left\langle u_r + Sn_r \right\rangle_w \mathcal{P}\, d\varphi + \int_0^\infty \varphi \left\langle K' \right\rangle_w \mathcal{P}\, d\varphi \tag{2.54}$$

$$= \int_0^\infty \left\langle u_r + Sn_r \right\rangle_w \mathcal{P}\, d\varphi + \int_0^\infty \varphi \left\langle K' \right\rangle_w \mathcal{P}\, d\varphi. \tag{2.55}$$

since $\mathcal{P} \to 0$ at both limits $\varphi = 0$ and $\varphi \to \infty$ of the integration.

Similarly, the following differential equation for the growth of turbulent flame brush thickness δ_T is obtained as

$$\frac{d\delta_T^2}{dt} = 2\pi \frac{d\sigma^2}{dt} = 2\pi \frac{d}{dt} \int_0^\infty (\varphi - R)^2 \mathcal{P}\, d\varphi \tag{2.56}$$

$$= 2\pi \int_0^\infty (\varphi - R)^2 \frac{\partial \mathcal{P}}{\partial t}\, d\varphi - 4\pi \frac{dR}{dt} \int_0^\infty (\varphi - R)\mathcal{P}\, d\varphi. \tag{2.57}$$

The second integral on the right hand side is zero by definition of R. Substituting for $d\mathcal{P}/dt$ from Eq. (2.51),

$$\begin{aligned} \frac{d\delta_T^2}{dt} = &- 2\pi \int_0^\infty (\varphi - R)^2 \frac{\partial}{\partial \varphi} \left(\left\langle u_r + Sn_r \right\rangle_w \mathcal{P} \right) d\varphi \\ &+ 2\pi \int_0^\infty (\varphi - R)^2 \left\langle K' \right\rangle_w \mathcal{P}\, d\varphi. \end{aligned} \tag{2.58}$$

Applying integration by parts on the first integral, the following form of the evolution equation for the thickness of the brush is obtained:

$$\begin{aligned} \frac{d\delta_T^2}{dt} = &- 2\pi \Big[(\varphi - R)^2 \left\langle u_r + Sn_r \right\rangle_w \mathcal{P} \Big]_0^\infty + 4\pi \int_0^\infty (\varphi - R) \left\langle u_r + Sn_r \right\rangle_w \mathcal{P}\, d\varphi \\ &+ 2\pi \int_0^\infty (\varphi - R)^2 \left\langle K' \right\rangle_w \mathcal{P}\, d\varphi \end{aligned} \tag{2.59}$$

As with Eq. (2.55), the first term on the right hand side drops to zero as $\mathcal{P} \to 0$ at both limits of the integration. The convective term is further broken

into three parts that separate the effects of turbulent dispersion, effects of mean radial velocity introduced in the domain by the propagating turbulent flame and associated density changes, and the effect of flame propagation on the thickness of the brush.

The ordinary differential equation for the flame brush thickness after this decomposition of the transport term reads

$$\begin{aligned}\frac{d\delta_T^2}{dt} &= 4\pi \int_0^\infty (\varphi - R) \left\langle u_r' \right\rangle_w \mathcal{P}\, d\varphi + 4\pi \int_0^\infty (\varphi - R) \overline{u}_r \mathcal{P}\, d\varphi \\ &+4\pi \int_0^\infty (\varphi - R) \left\langle S n_r \right\rangle_w \mathcal{P}\, d\varphi + 2\pi \int_0^\infty (\varphi - R)^2 \left\langle K' \right\rangle_w \mathcal{P}\, d\varphi,\end{aligned} \tag{2.60}$$

where $\overline{u}_r$ is the Reynolds-averaged mean radial velocity (not conditioned on the flame surface), and u_r' the corresponding fluctuation. Note that the surface average of the fluctuation $\left\langle u_r' \right\rangle_w$ is not zero since it is a gradient-weighted conditional mean of the Reynolds fluctuation.

2.4.3.2 Characterization of the PDF

The spatial distribution of the flame surface closely follows a Gaussian distribution, so the PDF of the radial distance $\mathcal{P}$ may be approximated as a normal distribution with mean R and standard deviation σ.

Figure 2.7 shows quadrants of representative planar slices of the instantaneous flame surface for flame configuration R2K1 at $t/\tau_0 = 4.2$. The instantaneous flame contours in the quadrants are shown in black color. The region $R - \sigma \leq \phi \leq R + \sigma$ is marked in red hue and provides an estimate of the turbulent flame brush.

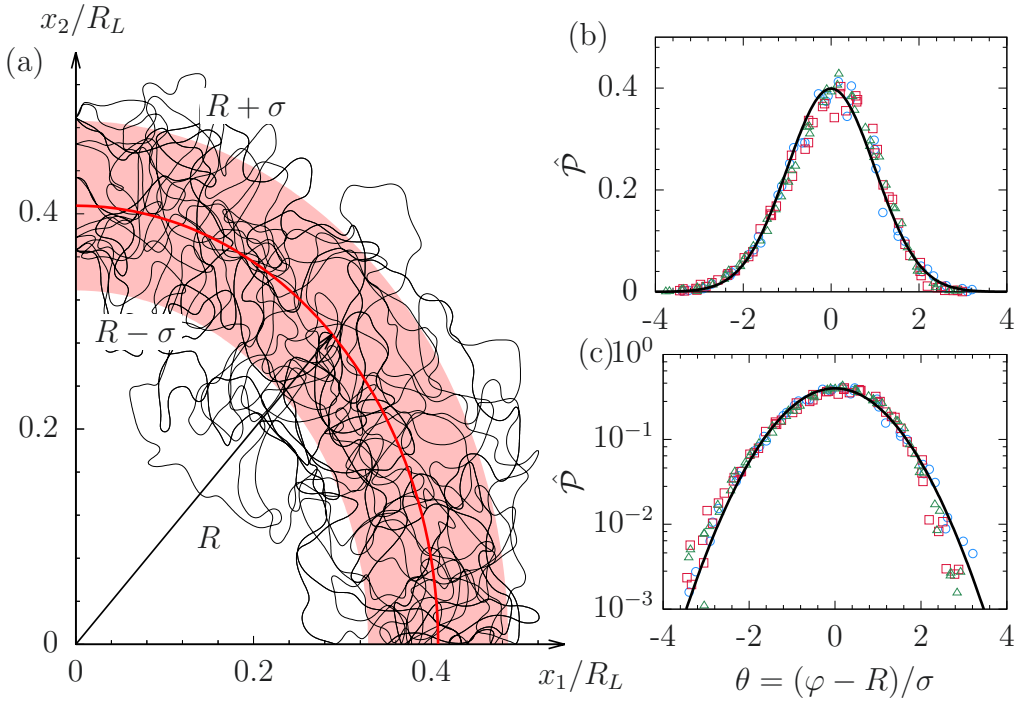

Figure 2.7: Characterization of the PDF of radial distance ϕ: (a) Quadrants of representative planar slices $x_1 - x_2$ of the Cartesian planes $x - y$, $y - z$ and $x - z$. (b) Normalized PDF $\hat{\mathcal{P}}$ against the brush coordinate θ in linear scale for flames R1K1 (◯), R2K1 (□) and R3K1 (△). The standard normal distribution is shown (thick black lines) for comparison also.

It is apparent the normalized PDF $\hat{\mathcal{P}} = \sigma\mathcal{P}$ is well described by the standard normal distribution $\mathcal{N}(0,1)$ in the normalized brush coordinate θ, consistently with data reported for various flame configurations in the literature (Lipatnikov & Chomiak [65] and references therein). Here, the normalized brush coordinate is defined as $\theta = (\varphi - R)/\sigma$.

Subplots (c) of the figure shows that the tails of the PDF are well approximated by the normal distribution also, although the comparison becomes worse for $|\theta| > 2$, possibly due to statistical convergence.

It must be noted that since the radial distance of the flame surface cannot be negative, the PDF can only be modeled as a truncated Gaussian with support $0 \leq \varphi < \infty$. However, since the mean flame distance R is much larger than the standard deviation σ, the difference between a truncated Gaussian and true normal distribution are negligible. Thus, for all practical purposes, $\mathcal{P}$ may be assumed to be a Gaussian in the region $R - 3\sigma \leq \varphi \leq R + 3\sigma$.

Since the PDF $\mathcal{P}$ and the surface density function Σ are related as $\mathcal{P}(\varphi, t) = 4\pi\varphi^2\Sigma(\varphi, t)/A$, a model for the surface density function may be obtained by assuming normal distribution for $\sigma\mathcal{P}$,

$$\Sigma(r,t) = \mathcal{P}(r,t)A/4\pi r^2 = (A/4\pi r^2\sigma)\,\mathcal{N}((r-R)/\sigma)), \tag{2.61}$$

where $\mathcal{N}$ denotes the standard normal distribution with zero mean and unit variance.

Figure 2.8 shows Σ at select times for simulations R1K1, R2K1, R3K1 and R4K1. The surface density function (SDF) is normalized by initial thermal

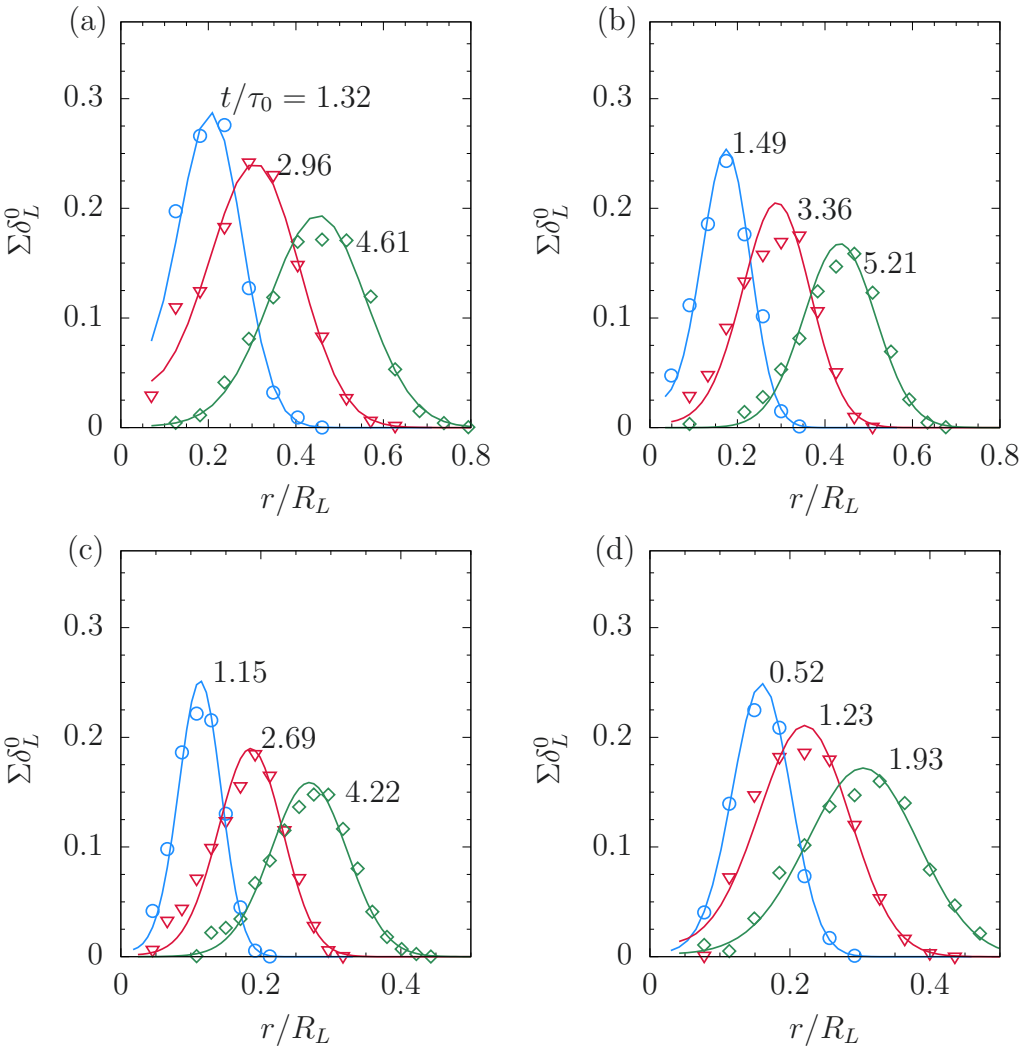

Figure 2.8: Surface density function evaluated with Eq. (2.34) at select times (symbols) for flames (a) R1K1, (b) R2K1, (c) R3K1 and (d) R4K1. The normalized time t/τ_0 is shown next to each profile. Model for Σ based on Eq. (2.61) is shown for comparison also (lines).

thickness δ_L^0 and plotted versus r/R_L, where R_L is the effective domain radius. With time, SDF is transported radially outward, its distribution broadens while the peak value $\Sigma_{\max}$ decreases. The broadening is due to the increase in the flame brush thickness and consistent with past observations of premixed spherical turbulent flames in decaying turbulence [96, 40].

The comparison between the surface density function evaluated from Eq. (2.34) and the model from Eq. (2.61) is satisfactory, indicating the the two methodologies are consistent. As discussed next in Sec. 2.5 and later in Chapter 4, the model for SDF will be leveraged to identify the location of the peak surface density $\Sigma_{\max}$.

2.5 Model for area ratio χ

Since the area ratio χ is related to the volumetric integral of Σ, broadening of the distribution of surface density function leads to increasing χ, while the decrease in the peak SDF $\Sigma_{\max}$ leads to the opposite effect. A more quantitative analysis of the area ratio is in order.

The location of the peak flame surface density, denoted henceforth by $\hat{r} = \hat{r}(t)$, is implicitly defined as

$$\frac{\partial \Sigma}{\partial r}\Big|_{r=\hat{r}} = -2\mathcal{P}(\hat{r},t)/\hat{r}^3 + \mathcal{P}'(\hat{r},t)/\hat{r}^2 = 0, \tag{2.62}$$

$$2\mathcal{P}(\hat{r},t) - \hat{r}\mathcal{P}'(\hat{r}) = 0, \tag{2.63}$$

since the surface density function only admits one maxima and no minima. In the equation above, $\mathcal{P}'$ denotes the partial derivative with respect to φ.

Based on Eq. (2.40), the maximum value of the surface density function $\Sigma_{\max}$ is

$$\Sigma_{\max} = \Sigma(\hat{r}, t) = (4\pi)^{-1} A \frac{\mathcal{P}'(\hat{r}, t)}{2\hat{r}} = (4\pi)^{-1} A \frac{\mathcal{P}(\hat{r})}{\hat{r}^2}. \tag{2.64}$$

Substituting Eq. (2.40) and Eq. (2.64) into the expression for area ratio χ, Eq. (2.37), the following expression is obtained:

$$\chi = \Sigma_{\max} \delta_T \beta, \tag{2.65}$$

where β is a geometric shape factor defined as

$$\beta = \frac{1}{\mathcal{P}(\hat{r}, t)\, \delta_T} \left(\frac{\hat{r}}{R} \right)^2. \tag{2.66}$$

The shape factor β is related solely to the functional form of $\mathcal{P}(\varphi, t)$.

For all practical purposes, the truncated normal distribution and the underlying normal distribution are identical on the account of negligible probability of $\varphi < 0$ if even if a true normal distribution is assumed. For simplicity, ignoring these small differences results in the following solution for $\hat{r}$ from Eq. (2.63),

$$\hat{r}(t) = 2\mathcal{P}(\hat{r}, t)/\mathcal{P}'(\hat{r}) = R \left(1 + \sqrt{1 - 8\alpha^2} \right) /2, \tag{2.67}$$

where $\alpha = \sigma/R$ is the relative standard deviation of the radial distance.

Substituting Eq. (2.67) into Eq. (2.66) and simplifying, the shape factor reads as

$$\beta = \beta(\alpha) = 0.25 \left(1 + \sqrt{1 - 8\alpha^2} \right)^2 \exp \left\{ (\sqrt{1 - 8\alpha^2} - 1)^2 / 8\alpha^2 \right\}. \tag{2.68}$$

The shape factor is a monotonic function of α. For $\alpha \to 0$, $\beta \to 1$ and decreases as α increases. For all flame configurations, $\alpha = 0$ at $t = 0$ since a laminar kernel is initiated. Initially, the standard deviation σ increases more rapidly as compared to R, α increases and β decreases. Eventually, the flame radius R increases more rapidly than σ and α decreases again. For all flame configurations, it was found that $\alpha \leq 0.33$ at all times and $0.875 \leq \beta \leq 1$.

Since $\beta \approx 1$, Eq. (2.65) illustrates that the area ratio is controlled by the product of peak flame surface density and the thickness of turbulent flame brush, both of which are independently controlled quantities associated with the surface wrinkling by turbulence. The temporal evolution of both these quantities is carefully examined with appropriate partial differential equations later in Chap. 3 and Chap. 4.

Chapter 3

Turbulent flame brush thickness

The turbulent flame brush thickness $\delta_T(t)$ is a statistical measure of the distance of flame surface from its mean location. Since the turbulent spherical flames in the database grow from an initially laminar kernel of fully burnt gases, the brush thickness grows from zero as time progresses and turbulence wrinkles the flame surface.

Equation (2.60) indicates that the growth of flame brush thickness is influenced turbulent diffusion, mean velocity field, flame propagation, and the differential flame stretch. Apart from turbulent diffusion, all other effects arise due to flame propagation and associated density changes.

Karlovitz [52] argued that for a slowly moving front ($u'/S_L \gg 1$), the evolution of turbulent flame brush must be equivalent to dispersion of material points due to turbulent motion. In such situations, the evolution of the flame brush is consistent with Taylor's theory of turbulent diffusion [109]. Indeed, as discussed below in section 3.2, the relative contributions of mean velocity, flame

---

The content presented in this chapter has been originally published in the following article:

Kulkarni, T., Bisetti, F. (2021). Analysis of the development of the flame brush in turbulent premixed spherical flames. Combustion and Flame, Available online at `https://doi.org/10.1016/j.combustflame.2021.111640`.

propagation and differential flame stretch to the flame brush become small compared to that of turbulent diffusion for large u'/S_L. Success for the theory has been reported in the literature for a variety of flame configurations [65, 64]. The spatial growth of the brush thickness with distance from the flame-holder or outlet may be regarded as temporal growth under Taylor's hypothesis [110].

The temporal evolution of the standard deviation $\widetilde{\sigma}$ of the position of material points in homogeneous isotropic turbulence is given by [109]

$$\frac{d\widetilde{\sigma}^2}{dt} = 2u'(t)\int_0^t u'(p) f_L(p,t)\, dp, \tag{3.1}$$

where f_L denotes the Lagrangian velocity auto-correlation function and $u'(t)$ the turbulence intensity at time t.

For stationary turbulence, Eq. (3.1) can be simplified by assuming an exponential form for the Lagrangian autocorrelation function (such as in [46]) to give

$$\frac{\widetilde{\sigma}^2}{l^2} = \frac{2t}{\tau^\dagger}\left(1 - \frac{\tau^\dagger}{t}\left[1 - e^{-t/\tau^\dagger}\right]\right), \tag{3.2}$$

where $l = u'^3/\epsilon$ is the integral length scale and $\tau^\dagger = l/u'$ is a reference time scale (here a constant). The short and long term limits of Eq. (3.2) are $\widetilde{\sigma}^2 \sim t^2$ for $t \ll \tau^\dagger$ and $\widetilde{\sigma}^2 \sim t$ for $t \gg \tau^\dagger$, respectively. The short time limit has been shown to explain reasonably well the early and near-field evolution of the brush in various experimental and numerical flame configurations, including spherically expanding flames and turbulent Bunsen flames [65]. The model suggests that the flame brush thickness scales with large, energy-containing

scales of turbulence (i.e. the integral scale l), since the ratio $\widetilde{\sigma}/l$ is a function of the normalized time $t/\tau^{\dagger}$ alone.

3.1 Correction to Taylor's theory

The turbulent diffusion term of Eq. (2.60) is equivalent to the Taylor's theory and in the limit $u'/s_L \to \infty$ the two approaches recover the same evolution of the brush thickness. Since the flame surface elements disperse in the radial direction, a geometric correction to Eq. (3.1) is necessary to account for the fact that the radial direction itself changes along the trajectories of surface elements.

Following closely the approach by Taylor [109], consider an ensemble of particles released on the surface of a sphere of radius R_0 at $t = 0$ and follow the evolution of variance of radial distance of the ensemble in time. The radial distance of a particle in the ensemble is governed by

$$\frac{dr(a,t)}{dt} = \mathbf{u}(\mathbf{x}(a,t),t) \cdot \mathbf{i}_r(a,t), \tag{3.3}$$

where $\mathbf{u}$ denotes the local fluid velocity at particle location $\mathbf{x}(a,t)$, a being the particle index in the ensemble, and $\mathbf{i}_r(a,t) = \mathbf{x}(a,t)/|\mathbf{x}(a,t)|$ is the unit vector in the radial direction. Integrating the ordinary differential equation with the initial condition $r(a,0) = R_0$, the particle distance at $t > 0$ is given by

$$r(a,t) = R_0 + \int_0^t \mathbf{u}(\mathbf{x}(a,p),p) \cdot \mathbf{i}_r(a,p)\, dp. \tag{3.4}$$

Here p represents a dummy variable of integration.

The variance σ^2 of the radial distance in absence of mean velocity is

$$\frac{1}{2}\frac{d\sigma^2}{dt} = \left\langle (r(a,t) - R_0)\frac{dr(a,t)}{dt} \right\rangle = \left\langle \mathbf{u}(a,t)\cdot\mathbf{i}_r(a,t)\int_0^t \mathbf{u}(a,p)\cdot\mathbf{i}_r(a,p)\,dp \right\rangle, \tag{3.5}$$

since the mean radial distance is constant and equal to R_0. In the expression above, angular brackets denote average of the ensemble of particles and the dependence of $\mathbf{u}$ on $\mathbf{x}(a,p)$ is written as $\mathbf{u}(a,p)$ for simplicity.

Equation (3.5) can be expanded as following in the Cartesian coordinates:

$$\begin{aligned}\frac{1}{2}\frac{d\sigma^2}{dt} = &\int_0^t \left\langle u_x(a,t)u_x(a,p)\frac{x(a,t)x(a,p)}{r(a,t)r(a,p)} \right\rangle dp \\ &\int_0^t \left\langle u_y(a,t)u_y(a,p)\frac{y(a,t)y(a,p)}{r(a,t)r(a,p)} \right\rangle dp \\ &\int_0^t \left\langle u_z(a,t)u_z(a,p)\frac{z(a,t)z(a,p)}{r(a,t)r(a,p)} \right\rangle dp,\end{aligned} \tag{3.6}$$

where u_x, u_y, u_z and x, y, z denote the Cartesian components of the velocity vector $\mathbf{u}$ and the position vector $\mathbf{x}$, respectively.

In homogeneous isotropic turbulence the velocity vector $\mathbf{u}$ is uncorrelated with the position vector $\mathbf{x}$. Moreover, due to isotropy, the three integrals in Eq. (3.6) are equal to each other and can be written in terms of Lagrangian velocity auto-correlation function. In light of these simplifications, Eq. (3.6) can be simplified as

$$\frac{1}{2}\frac{d\sigma^2}{dt} = \int_0^t \langle u_x(a,t)u_x(a,p)\rangle \left\langle \frac{\mathbf{x}(a,t)\cdot\mathbf{x}(a,p)}{|\mathbf{x}(a,t)|\,|\mathbf{x}(a,p)|} \right\rangle dp, \tag{3.7}$$

with an additional factor that accounts for the dependence on the mean cosine

of the angle between the radial unit vectors on Lagrangian trajectories. Let the angle between radial unit vectors at time p and t be denoted as $\alpha_{p,t}$.

The final expression for the modified dispersion relation in radial coordinate is given by

$$\frac{1}{2}\frac{d\sigma^2}{dt} = u'(t)\int_0^t u'(p) f_L(p,t)\ \langle \cos\alpha_{\alpha,t}\rangle\ dp, \tag{3.8}$$

where f_L is the Lagrangian velocity auto-correlation function in decaying isotropic turbulence

$$f_L(t_1,t_2) \equiv \frac{\langle u_x(a,t_1)u_x(a,t_2)\rangle}{u'(t_1)u'(t_2)}. \tag{3.9}$$

In summary, since the radial direction itself varies along a Lagrangian trajectory, an additional orientation factor $\langle \cos\alpha_{p,t}\rangle$ must be included in the dispersion relation (Eq. (3.1)). This implies that Taylor's theory overestimates the variance in the radial direction since $\cos\alpha_{p,t} \leq 1$. The orientation factor $\langle \cos\alpha_{p,t}\rangle$ depends on the lateral movement of particles in the polar and azimuthal directions compared to that in the radial direction and is close to unity for small values of the ratio between the two.

3.2 Dimensionless evolution equation

To compare the development of turbulent flame brush thickness and its growth rate across different flames in the database, the evolution equation is considered in a transformed, dimensionless form. Consistent with the turbulent diffusion theory, the integral length scale l and the eddy turnover

time τ are chosen as reference scales. Note that in decaying turbulence these scales themselves change in time. In particular, using the instantaneous eddy turnover time $\tau(t)$ is akin to the transformation from t to s, since the two are related as $ds \equiv dt/n\tau$.

The evolution equation for the dimensionless brush thickness $\hat{\delta}_T = \delta_T/l$ reads

$$\frac{d\hat{\delta}_T}{ds} = n\tau \frac{d(\delta_T/l)}{dt} = \frac{3n}{2u'}\frac{d\delta_T}{dt} - \frac{\delta_T}{l}\frac{dl}{ds} \tag{3.10}$$

$$= \frac{3n}{2u'}\frac{d\delta_T}{dt} - (1-n/2)\hat{\delta}_T. \tag{3.11}$$

The factor $3/2$ appears in front of $d\delta_T/dt$ since $\tau/l = (k/\epsilon)\,(u'^3/\epsilon)^{-1} = 3/(2u')$. In addition, the second term on the right hand side of Eq. (3.11) appears due to evolution of integral length scale itself, which evolves in decaying turbulence as $l/l_0 = \exp((1-n/2)s)$.

Substituting for $d\delta_T/dt$ from Eq. (2.60) in Eq. (3.11) leads to

$$\begin{aligned}\frac{d\hat{\delta}_T}{ds} = &\underbrace{\frac{nC_\delta}{u'}\int_{-R/\sigma}^{\infty} \langle u_r' \rangle_w\, \theta\hat{\mathcal{P}} - (1-n/2)\hat{\delta}_T}_{T_1} + \underbrace{\frac{nC_\delta}{u'}\int_{-R/\sigma}^{\infty} \overline{u}_r \theta\hat{\mathcal{P}}\, d\theta}_{T_2} \\ &+ \underbrace{\frac{nC_\delta}{u'}\int_{-R/\sigma}^{\infty} \langle Sn_r \rangle_w\, \theta\hat{\mathcal{P}}\, d\theta}_{T_3} + \underbrace{\frac{n\hat{\delta}_T}{2}\int_{-R/\sigma}^{\infty} \langle K' \rangle_w\, \theta^2\hat{\mathcal{P}}\, d\theta}_{T_4}.\end{aligned} \tag{3.12}$$

In the equation above, $C_\delta = 3\sqrt{\pi/2}$ is a constant. The transformation from radial coordinate r to the normalized brush coordinate θ attaches the frame of reference to the mean radial location of the flame surface. The four terms on the right hand side of Eq. (3.12) identify the effects of turbulent

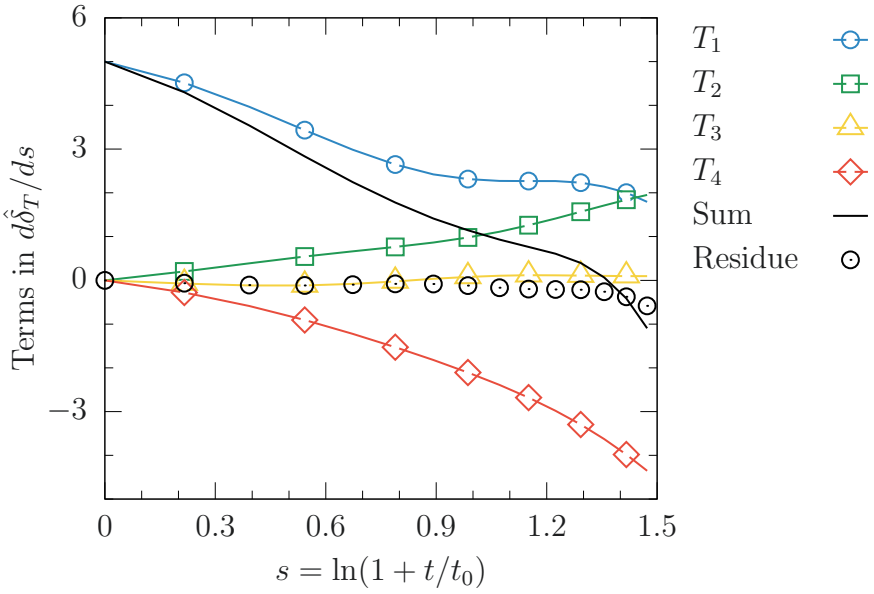

Figure 3.1: Contribution of various mechanisms to the growth of turbulent flame brush thickness. Data shown for flame R2K1.

dispersion (term T_1), mean radial velocity (term T_2), flame propagation (term T_3) and flame stretch (term T_4) on the temporal evolution of the thickness of the flame brush.

Figure 3.1 shows contributions of the four terms T_1, T_2, T_3, and T_4 on the evolution of normalized flame brush thickness for flame R2K1. Turbulent dispersion dominates early in the evolution of the brush, leading to a rapid increase in its thickness. Effects of mean radial velocity and flame stretch increase in magnitude with time and become comparable to turbulent dispersion only at later time. The flame stretch (term T_4) is negative at all time and slows down the growth of the brush thickness. The contribution of flame propagation (term T_3) is negligible at all times. As a result, the growth

of turbulent flame brush slows down with time and its thickness appears to reach an asymptotic or a maximum value. The following sections discuss each of these mechanisms in detail.

3.2.1 Turbulent diffusion

As discussed at the start of this chapter, the brush thickness of slow, thin flames with no gas expansion mimics the dispersion of an ensemble of material elements. Then, the turbulent diffusion term T_1, when considered in isolation, should match the predictions of Taylor's theory, appropriately modified as discussed earlier. To facilitate the comparison, the evolution of normalized dispersion thickness $\widehat{\sigma} = \sigma/l$ in the logarithmic time coordinate according to the turbulent diffusion theory is obtained as following.

Starting from Eq. (3.7), assume that the cosine factor $\langle \cos(\alpha_{p,t}) \rangle \approx 1$ at all times. Then, the dispersion thickness σ grows as

$$\sigma^2 = 2 \int_0^t u'(t') \left(\int_0^{t'} u'(t'') f_L(t', t'') \, dt'' \right) dt'. \tag{3.13}$$

The Lagrangian auto-correlation function $f_L(t', t'')$ evolves differently for different flames since the eddy turnover time scale τ is different. Furthermore, eddy turnover time τ itself changes due to decaying turbulence which makes the comparison of σ across different flames difficult.

Huang and Leonard [48] demonstrated that f_L exhibits a self-similar form in s coordinate, i.e. $f_L(s', s'')$ is a function of the lag in the s coordinate, $\Delta s = s' - s''$ alone. Since transformation from t to s compensates for different

initial conditions across the flames, such a transformation allows for comparison of the effects of turbulent dispersion on the growth of the flame brush across different flames and also with that of material elements in decaying turbulence.

The transformation from t to s in Eq. (3.13) with $ds = dt/n\tau$ leads to

$$\sigma^2(s) = 2n^2 \int_0^s u'(s')\tau(s') \left(\int_0^{s'} u'(s'')\tau(s'') f_L(s', s'')\, ds'' \right) ds' \tag{3.14}$$

$$= (9n^2/2) \int_0^s l(s') \left(\int_0^{s'} l(s'') f_L(s' - s'')\, ds'' \right) ds' \tag{3.15}$$

since $u'\tau = u'k/\epsilon = 3l/2$. Multiplying both sides with $2\pi/l^2$, the equation above can be written as

$$\widehat{\sigma}^2 \equiv \frac{2\pi\sigma^2}{l^2} = 9\pi n^2 \int_0^s ds' \int_0^{s'} ds''\, f_L(s' - s'') \exp\left\{(1 - n/2)(s' + s'' - 2s)\right\}, \tag{3.16}$$

since $l(s')/l(s) = \exp((1 - n/2)(s' - s))$ in decaying turbulence.

Figure 3.2 compares the turbulent dispersion term T_1 with the predicted rate of change $d\widehat{\sigma}/ds$ according to Eq. (3.16). An exponential model for $f_L(s' - s'')$ as proposed by Huang and Leonard [48] was used to numerically evaluation σ from Eq. (3.16) and subsequently its rate of change using finite difference derivatives. Shaded gray region marks predictions of the turbulent diffusion theory for various values of decay exponent $1.55 \leq n \leq 1.78$, the range observed for different flames. The turbulent dispersion term T_1 is similar to $d\widehat{\sigma}/ds$ from Eq. (3.16), albeit lower in magnitude. This difference

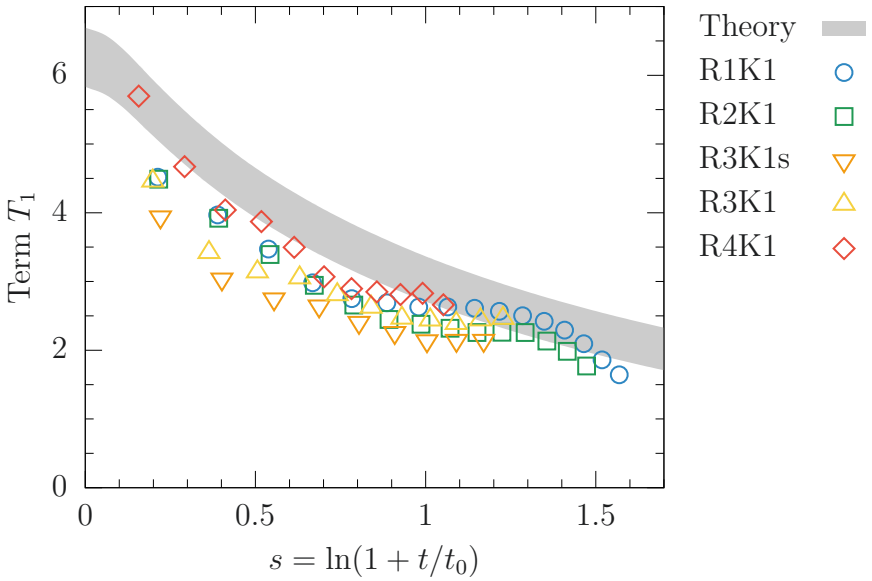

Figure 3.2: Comparison of the turbulent dispersion term T_1 with the predictions of Taylor's theory.

likely originates from the orientation factor $\langle \cos \alpha_{p,t} \rangle$ which was ignored in the present analysis.

This hypothesis is supported by the following observations. Early on, when the thickness of turbulent flame brush is small, any movement of flame surface elements in a direction perpendicular to the radial direction is small compared to their radial distance, thus the orientation factor is approximately unity. Accordingly, an agreement between T_1 and $d\widehat{\sigma}/ds$ is seen.

Subsequently, the thickness of turbulent flame brush grows rapidly compared to the rate of change of the mean radial distance and the orientation factor is expected to decrease, resulting in a larger deviation. In the long time limit, the mean radial distance of the flame surface grows large while

the thickness of the brush reaches an asymptotic value and the orientation factor increases towards unity again. The deviation between $d\widehat{\sigma}/ds$ and term T_1 mimics this trend.

It is important to note here that the decrease in the magnitude of T_1 in time is not due to decaying turbulence, since it is already accounted for by the reference velocity scale u', which changes in time. Instead, the decrease results from the decorrelation of radial velocity fluctuations in time, consistently with the Lagrangian approach of Taylor's theory.

In the current formulation the said de-correlation manifests itself as a decrease in the magnitude of the normalized radial velocity fluctuation ($\langle u'_r \rangle_w / u'$), while the distribution of the flame surface in the normalized brush coordinate (i.e. $\hat{\mathcal{P}}$) remains virtually identical, as can be seen in Fig. 3.3.

Such a change in the radial velocity fluctuation experienced by the surface elements is expected for an ensemble of material points too, as discussed next. Surface elements start at the radial distance $r = R_0$ at $t = 0$ and face positive and negative radial velocity fluctuation alike. However, the surface elements that experience negative (respectively positive) fluctuations are transported to lower (respectively higher) radial distances as compared to the mean radial distance. Since the velocity fluctuation is correlated with itself over time, flame surface elements at the trailing edge experience negative fluctuation and at the leading edge experience positive fluctuation, resulting in a gradient of $\langle u'_r \rangle_w / u'$ across the brush. Since the auto-correlation weakens in time, the slope of $\langle u'_r \rangle_w / u'$ across the brush decreases in time.

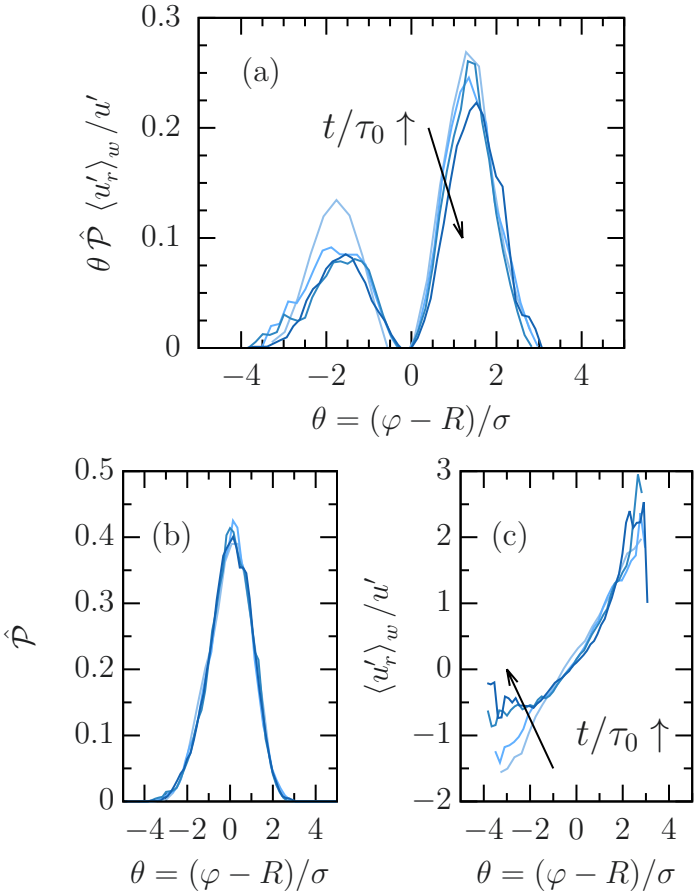

Figure 3.3: Turbulent dispersion term T_1 for flame configuration R3K1s: (a) Integrand $\theta\hat{\mathcal{P}}\,\langle u_r'\rangle_w/u'$ at four instants, (b) PDF of the normalized brush coordinate $\hat{\mathcal{P}}$, and (c) Normalized gradient-weighted radial velocity fluctuation $\langle u_r'\rangle_w/u'$. Simulation time increases in the direction of the arrow, i.e. from light to dark hues, corresponding to $t/\tau_0 = 0.81$, 1.63, 2.44 and 3.25.

In summary, the development of the turbulent flame brush due to turbulent dispersion considered in isolation is similar to the prediction of Taylor's theory. The contribution of this mechanism to the growth of the flame brush thickness decreases in time due to decorrelation of the radial velocity fluctua-

tion in time.

3.2.2 Mean velocity term

The development of the flame brush is affected also by the mean velocity field, which is induced by the propagating turbulent flame itself. The density change across the front (i.e. between reactants and products) due to thermal expansion leads to a spatially varying mean radial velocity field in the domain. Since the mean radial velocity in the reactants is higher than that in the products (see discussion in Sec. 2.3.2), the flame surface closer to the reactants (the leading edge) propagates faster than that closer to the products (the trailing edge), resulting in a broadening of the brush [3]. In the proposed framework this effect is quantified by term T_2, which is re-written below for reference:

$$T_2 = nC_\delta \int_{-R/\sigma}^{\infty} \frac{\overline{u}_r}{u'} \theta \hat{\mathcal{P}} \, d\theta. \tag{3.17}$$

While numerical modeling of term T_2 requires a solution to the mean radial velocity field and is configuration specific, universal scaling arguments may be made based on the source terms that affect $\overline{u}_r$. For this purpose, consider the Reynolds averaged continuity equation, written below in a simplified form considering spherical symmetry:

$$\frac{1}{r^2}\frac{\partial(r^2\overline{u}_r)}{\partial r} = -\frac{1}{\overline{\rho}}\frac{\partial \overline{\rho}}{\partial t} - \frac{\overline{u}_r}{\overline{\rho}}\frac{\partial \overline{\rho}}{\partial r} - \frac{1}{\overline{\rho}\, r^2}\frac{\partial r^2 \overline{\rho' u_r'}}{\partial r}. \tag{3.18}$$

In the equation above, over-bar (such as $\overline{\rho}$) denotes Reynolds averages and primes (such as ρ') the corresponding fluctuation.

Further simplifications are made by adopting the following assumptions. First, the Bray-Moss-Libby [15] model for mean density $\overline{\rho}$ is assumed to hold, so that

$$\begin{aligned}\overline{\rho}(r,t) &\approx \rho_u(1-\overline{C}) + \rho_b\overline{C} \\ &= \rho_{u,0}(p/p_0)^{1/\gamma}\left[1-(1-1/\zeta)\overline{C}\right]. \end{aligned} \tag{3.19}$$

In the equation above $\rho_u(t)$ and $\rho_b(t)$ are temporally varying densities of reactants and products, respectively and $\zeta = \rho_u/\rho_b$ their ratio, assumed a constant. Isentropic compression of gases in the closed vessel is assumed with $\rho_u/\rho_{u,0} = \rho_b/\rho_{b,0} = (p/p_0)^{1/\gamma}$. The ratio of specific heats $\gamma \approx 1.3$ is taken equal in reactants and products and a constant.

The temporal and spatial derivatives of density are related to those of the mean progress variable $\overline{C}$ and pressure p,

$$\frac{1}{\overline{\rho}}\frac{d\overline{\rho}}{dt} = \frac{1}{\gamma}\frac{d\log(p/p_0)}{dt} - \frac{1-1/\xi}{1-(1-1/\xi)\overline{C}}\frac{d\overline{C}}{dt} \tag{3.20}$$

$$\frac{1}{\overline{\rho}}\frac{d\overline{\rho}}{dr} = -\frac{1-1/\xi}{1-(1-1/\xi)\overline{C}}\frac{\partial\overline{C}}{\partial r}. \tag{3.21}$$

Substituting Eq. (3.21) and (3.20) in Eq. (3.18), the simplified continuity equation reads

$$\begin{aligned}\frac{1}{r^2}\frac{\partial r^2\overline{u}_r}{\partial r} = &-\frac{1}{\gamma}\frac{d\log(p/p_0)}{dt} - \frac{1}{\overline{\rho}r^2}\frac{\partial r^2\overline{\rho' u_r'}}{\partial r} \\ &+ \frac{1-1/\zeta}{1-(1-1/\xi)\overline{C}}\left(\frac{\partial\overline{C}}{\partial t} + \overline{u}_r\frac{\partial\overline{C}}{\partial r}\right).\end{aligned} \tag{3.22}$$

The effects of rise in chamber pressure, turbulent mass flux and flame propagation on the mean radial velocity are thus identified and separated.

Since the variation of mean radial velocity through the brush is of particular interest, a dimensionless form of Eq. (3.22) is obtained by transforming the radial coordinate r to the brush coordinate θ with $(\partial/\partial\theta)_s = \sigma(\partial/\partial r)_t$, and from time t to the logarithmic coordinate s with $(\partial/\partial s)_\theta = n\tau(\partial/\partial t)_r$, to get

$$\begin{aligned}\left(1+\theta\frac{\sigma}{R}\right)^{-2}\frac{\partial(1+\theta\sigma/R)^2(\overline{u}_r/u')}{\partial\theta} &= -\frac{\sigma}{nu'\tau}\,\frac{1}{\gamma}\frac{d\log(p/p_0)}{ds} \\ &\quad -(1+\theta\sigma/R)^{-2}\,\frac{1}{\overline{\rho}u'}\frac{\partial(1+\theta\sigma/R)^2\overline{\rho' u_r'}}{\partial\theta} \\ &\quad +\frac{\sigma}{u'}\frac{1-1/\xi}{1-(1-1/\xi)\overline{C}}\left[\frac{\partial\overline{C}}{\partial t}+\overline{u}_r\frac{\partial\overline{C}}{\partial r}\right].\end{aligned} \tag{3.23}$$

Apart from pressure rise and the turbulent mass flux, the propagation of turbulent flame influences mean velocity through spatial and temporal changes to the average reaction progress variable. This can be easily seen by performing Reynolds averaging operation on the reaction progress variable equation (2.24) to get,

$$\frac{\partial\overline{C}}{\partial t}+\overline{u}_r\cdot\frac{\partial\overline{C}}{\partial r}=\overline{S|\nabla C|}-\overline{\mathbf{u}'\cdot\nabla C'}. \tag{3.24}$$

Substituting Eq. (3.24) into Eq. (3.23), the following form of the equation is

obtained:

$$\left(1+\theta\frac{\sigma}{R}\right)^{-2}\frac{\partial(1+\theta\sigma/R)^2(\overline{u}_r/u')}{\partial\theta}=\underbrace{-\frac{\hat{\delta}_T}{nC_\delta\gamma}\frac{d\log(p/p_0)}{ds}}_{\text{pressure}}$$
$$\underbrace{-\left(1+\theta\frac{\sigma}{R}\right)^{-2}\frac{1}{\overline{\rho}u'}\frac{\partial(1+\theta\sigma/R)^2\overline{\rho'u'_r}}{\partial\theta}-\frac{1-1/\xi}{1-(1-1/\xi)\overline{C}}\frac{\sigma\overline{u'\cdot\nabla C'}}{u'}}_{\text{turbulent flux}} \tag{3.25}$$
$$\underbrace{+\frac{1-1/\xi}{1-(1-1/\xi)\overline{C}}\frac{\overline{(S/S_L)(|\nabla C|\sigma)}}{u'/S_L}}_{\text{flame propagation}}.$$

In the above equation, $\mathsf{F}(\xi;\overline{C}=(1-1/\xi)/(1-(1-1/\xi)\overline{C})$ is the coefficient that scales the gradient weighted displacement speed. The mean radial velocity is normalized by the instantaneous turbulence intensity u'. The three source terms on are labeled 'pressure', 'turbulent flux' and 'flame propagation'.

Figure 3.4 shows the source terms at $t/\tau_0 = 2.44$ for flames R3K1 and R3K1s. Recall that apart from the domain radius R_L the other flow parameters are identical across the two flames. It can be seen that the contribution of flame propagation to the mean velocity is largest and independent of the domain size. Pressure rise contribution differs between R3K1 and R3K1s on the account of different domain size, yet its overall contribution to mean velocity is negligible. As a result the mean velocity field is similar between R3K1 and R3K1s. For this reason the following scaling analysis may also be expected to hold for spherical turbulent flames in an open domain.

Since the flame propagation source term dominates over the other two, scaling of velocity field and term T_2 may follow that of the propagation source

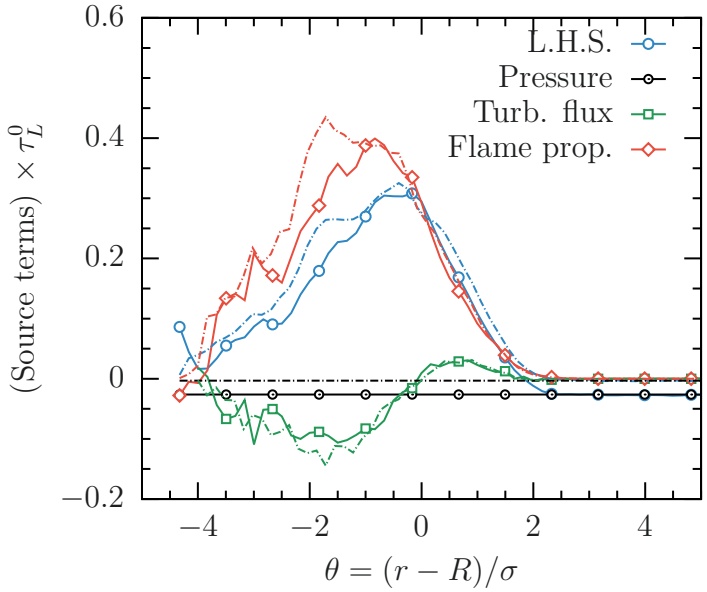

Figure 3.4: Source terms for mean radial velocity for flame configurations R3K1 and R3K1s at $t/\tau_0 = 2.44$.

term. The flame propagation term in Eq. (3.25) is directly proportional to the mean, gradient-weighted displacement speed $\overline{S|\nabla C|}$ and is parameterized by the density ratio ξ though the coefficient $\mathsf{F}(\xi; \overline{C})$. The following discussion demonstrates that the flame propagation term scales with the ratio S_T/u', the ratio of turbulent flame speed to the instantaneous turbulence intensity.

The normalized gradient-weighted displacement speed may be written as an integral of conditional mean over all iso-surfaces as follows:

$$\begin{aligned} \overline{(S/S_L)|\nabla C|\sigma} &= (\sigma/S_L) \int_0^1 \langle S|\nabla C| \big| C = c \rangle \mathcal{P}_C(C = c)\, dc \\ &= \sigma \int_{0^+}^{1^-} \frac{\langle S(C = c) \rangle_w}{S_L} \Sigma(C = c)\, dc, \end{aligned} \tag{3.26}$$

where $\langle . \rangle_w$ denotes surface weighted average according to Eq. (2.45) at the iso-

level $C = c$, not c^*. The product of the surface-weighted displacement speed and the surface density function is integrated over all iso-levels $0 < c < 1$. The iso-levels $c = 0$ and $c = 1$ are ill-defined (reactants and products) and are excluded from the integration. This does not affect the overall integral since $|\nabla C| \approx 0$ in these regions. All quantities in Eq. (3.26) depend on r and t, although not explicitly mentioned.

Multiplying and dividing by $\Sigma_{\max}$, the peak flame surface density of the iso-surface $C = c^*$, results in the following expression

$$\overline{(S/S_L)|\nabla C|\sigma} = \Sigma_{\max}\sigma \int_{0^-}^{1^+} \frac{\langle S(C = c; r, t)\rangle_w}{S_L} \frac{\Sigma(C = c; r, t)}{\Sigma_{\max}}\, dc \tag{3.27}$$

$$\sim \Sigma_{\max}\delta_T \sim S_T/S_L \tag{3.28}$$

The mean gradient-weighted displacement speed is directly proportional to the product of peak flame surface density and the turbulent flame brush thickness, since the integrands $\langle S\rangle / S_L$ and $\Sigma/\Sigma_{\max}$ are self-similar (not shown). As a result, the mean gradient-weighted displacement speed scales as the turbulent flame speed S_T.

Since the density ratio ξ is the same for all flames in the present database, the flame propagation source term in Eq. (3.25) and, by extension, term T_2 of Eq. (3.12) scale as S_T/u'. Indeed, large variations in T_2 with time disappear when multiplied by the ratio u'/S_T as shown in Fig. 3.5. Term T_2 increases in time with turbulent burning rates and also across flames R1 to R4 due to increasing initial Reynolds number.

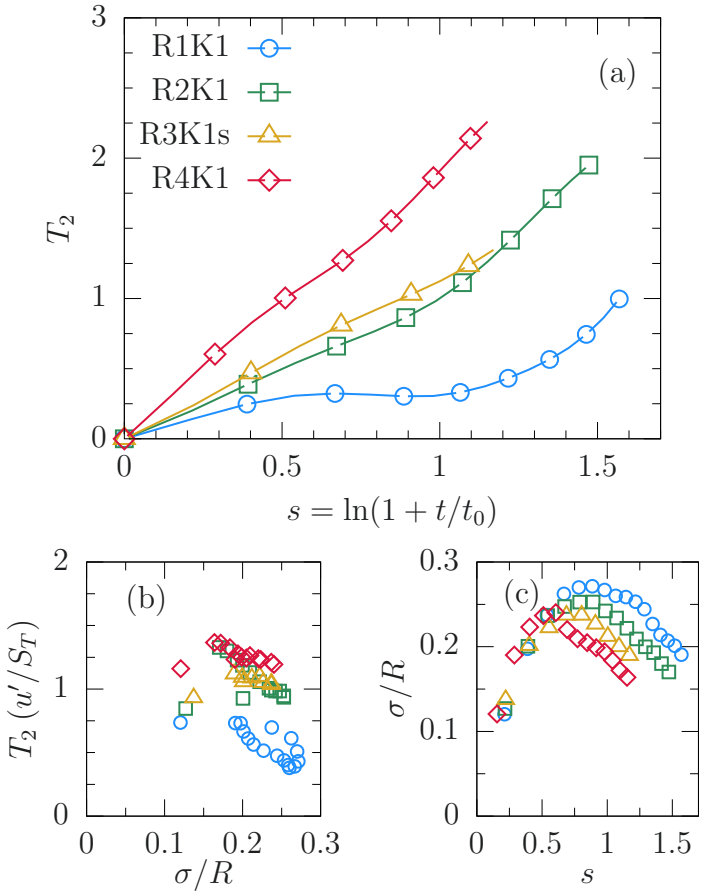

Figure 3.5: The mean velocity term T_2 (a) as written in Eq. (3.12), (b) compensated by ratio u'/S_T against dimensionless standard deviation σ/R, and (c) evolution of σ/R in logarithmic time coordinate s.

Eq. (3.25) highlights the role of density ratio ξ on the growth of turbulent flame brush through the coefficient $\mathsf{F}(\xi;\overline{C})$. While the present database is not suitable for examination of such dependence, support for the postulate comes from experiments on turbulent Bunsen and V-shaped flames by Nie et. al. [81], Tamadonfar and Gülder [108], and Kheirkhah and Gülder [54]. The researchers reported and investigated the spatial growth rate of turbulent

flame brush for various mixtures and observed deviations from Taylor's theory. The observed trends are consistent with the effects of mean velocity on the development of the brush, as discussed below.

Tamadonfar and Gülder [108] and Nie et. al. [81] reported that the spatial growth rate of flame brush thickness increased when the equivalence ratio changed from 0.7 to 1 for premixed turbulent Bunsen flames of various hydrocarbon fuels. Kheirkhah and Gülder [54] observed a similar increase for turbulent premixed methane/air V-shaped flames. Since the equivalence ratio was changed at fixed turbulence intensity and bulk flow velocity in all these studies, it is reasonable to assume that the contribution of the turbulent dispersion mechanism to the development of the brush remained the same.

On the other hand, increases in the equivalence ratio for lean hydrocarbon fuels towards unity bring about an increase in both the laminar flame speed and the density ratio ξ, which lead to a larger mean velocity gradient across the flame brush.

Data from Tamadonfar and Gülder [108] for fuel-rich mixtures is consistent with the effects of mean velocity also. The researchers observed that the growth rate decreased when the equivalence ratio increased from unity towards rich mixtures. This trend mimics the dependence of laminar flame speed on the equivalence ratio, which peaks near stoichiometry. Moreover, when experiments were repeated at higher turbulence intensity, a lower sensitivity to the equivalence ratio was observed [108, 54]. Since a higher turbulence intensity lowers the relative contribution of term T_2 as compared to T_1 (see

Eq. (3.12)), the lower sensitivity of the turbulent flame brush to equivalence ratio is consistent with the proposed framework.

In closing, it must be noted that the mean velocity field and term T_2 of Eq. (3.12) are geometry dependent. For example for the spherical flames they are influenced by the geometric parameter σ/R also. In the limit of $\sigma/R \to 0$, the evolution of the flame brush thickness of a spherical turbulent flame is similar to that of a planar flame. This corresponds to both the small time (when $\sigma \approx 0$) and the long time (when $R \gg \sigma$) behavior. Similar geometry-specific effects are expected in other flow configurations.

3.2.3 Differential flame stretch

Flame stretch is responsible for production and destruction of flame surface. If the stretch rate is uniform, for example in the growth of material surface in isotropic turbulence, then the surface area increases at the same rate everywhere and $\mathcal{P}$ and its moments are not affected. Flame stretch varies across the brush, changing from negative at the trailing edge (net destruction of flame surface) to positive at the leading edge (net production of flame surface). This asymmetry acts to reduce the thickness of flame brush by modifying the spatial distribution of the flame surface. The following discussion in this section demonstrates that the change in flame stretch across the brush is primarily associated with that in the flame curvature κ and displacement speed S.

To facilitate the analysis, a gradient-weighted displacement speed is

defined as $S_g \equiv S|\nabla C|/\langle|\nabla C|\rangle$, where $\langle|\nabla C|\rangle$ is the mean gradient magnitude at the surface and depends on r and t. The curvature-propagation component of flame stretch reads

$$\langle S\nabla\cdot n\rangle_w = \frac{\langle S(\nabla\cdot\mathbf{n})|\nabla C|\rangle}{\langle|\nabla C|\rangle} = -2\langle S_g\kappa\rangle, \tag{3.29}$$

where the surface-weighted average has been re-written as a conditional mean of $S_g\kappa$ at the surface.

The conditional mean of the product is further simplified as the product of the conditional means and the conditional covariance as

$$-2\langle S_g\kappa\rangle = -2\langle S\rangle_w\langle\kappa\rangle - 2\mathrm{covar}\{S_g,\kappa\} = K^b + K^c. \tag{3.30}$$

Note that $\langle S\rangle_w = \langle S_g\rangle$ by definition. The two components of curvature-propagation stretch term are denoted as K^b and K^c.

With this decomposition, the following three contributions to flame stretch are recognized: tangential strain rate $\langle a\rangle_w$, product of mean curvature and displacement speed K^b, and the conditional covariance term K^c. Their contribution to the differential stretch term T_4 are split accordingly as

$$\begin{aligned} T_4 &= T_4^a + T_4^b + T_4^c \\ &= \frac{n\hat{\delta}_T}{2}\int_{-R/\sigma}^{\infty}\left(\langle a\rangle_w - K_G^a\right)\theta^2\hat{\mathcal{P}}\,d\theta \\ &+ \frac{n\hat{\delta}_T}{2}\int_{-R/\sigma}^{\infty}\left(-2\langle S\rangle_w\langle\kappa\rangle - K_G^b\right)\theta^2\hat{\mathcal{P}}\,d\theta \\ &+ \frac{n\hat{\delta}_T}{2}\int_{-R/\sigma}^{\infty}\left(-2\mathrm{covar}\{S_g,\kappa\} - K_G^c\right)\theta^2\hat{\mathcal{P}}\,d\theta. \end{aligned} \tag{3.31}$$

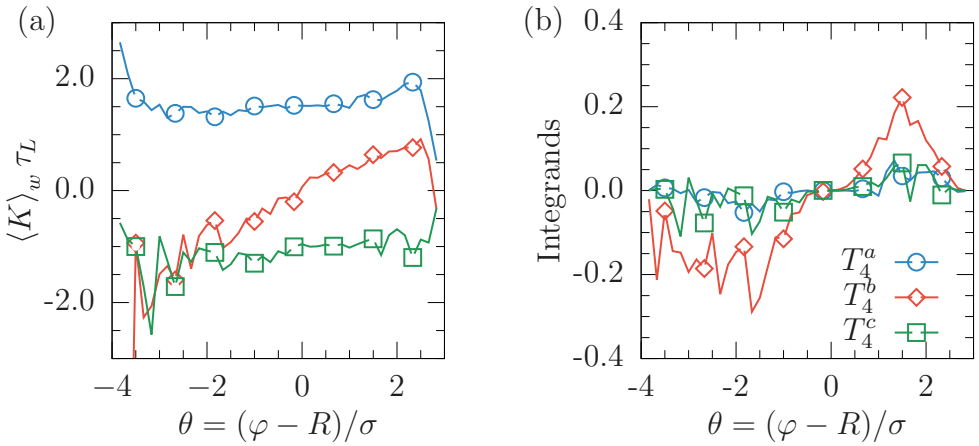

Figure 3.6: Spatial variation of stretch components and integrands of terms T_4^a, T_4^b and T_4^c. Data presented for flame R3K1s at $t/\tau_0 = 2.44$.

The three contributions to T_4 are denoted as T_4^a, T_4^b and T_4^c, respectively and K_G^a, K_G^b and K_G^c are their respective global means:

$$K_G^a = \int_{-R/\sigma}^{\infty} \langle a \rangle_w \hat{\mathcal{P}}\, d\theta, \qquad K_G^b = -2 \int_{-R/\sigma}^{\infty} \langle S \rangle_w \langle \kappa \rangle \hat{\mathcal{P}}\, d\theta$$
$$K_G^c = -2 \int_{-R/\sigma}^{\infty} \mathrm{covar}\{S_g, \kappa\} \hat{\mathcal{P}}\, d\theta. \tag{3.32}$$

Figure 3.6 shows the spatial variation of the three stretch components and integrands of terms T_4^a, T_4^b and T_4^c. The tangential strain rate and covariance components of the flame stretch rate are uniform across the brush. Since both these terms affect the flame surface uniformly, their contribution to the growth of the brush is negligible, as shown in Fig. 3.6(b).

On the other hand, both the product of the mean displacement speed $\langle S \rangle_w$ and the mean flame curvature $\langle \kappa \rangle$ varies significantly across the brush. In fact, both the speed and curvature decrease from the trailing edge to the

leading edge. The total flame stretch $\langle K \rangle_w$ is negative at the trailing edge and increases to a positive value at the leading edge. This behavior is well documented for spherical [100, 101] and planar flames [113, 19] and understood to be a universal feature of turbulent premixed flames.

The fact that the mean curvature $\langle \kappa \rangle$ decreases from positive to negative across the brush is a fundamental topological feature of a closed surface. The part of any closed surface behind its mean location in the direction of its average normal direction must necessarily have positive curvature on average. Similarly, the trailing edge of the flame brush is expected to have negative curvature on average.

Figure 3.7 presents the joint probability density function (PDF) of flame curvature and the gradient-weighted displacement speed at various locations in the brush. Flame surface is divided into five parts based on its location in the brush. Recall that the terminology *flame surface* refers to the iso-level surface $C = c^*$.

The gradient-weighted displacement speed S_g is multiplied by the ratio of mean density at the iso-surface ρ_* to the reactants' density ρ_u to compensate of a higher density at the flame surface. The presence of the weight $|\nabla C| / \langle |\nabla C| \rangle$ de-emphasizes large displacement speeds in highly curved areas at the trailing and leading edge whose contribution to the surface averaged statistics is low on the account of $|\nabla C| / \langle |\nabla C| \rangle \ll 1$. As a result, the joint-PDF of S_g and κ is S-shaped instead of a nearly linear shape reported in the literature [50].

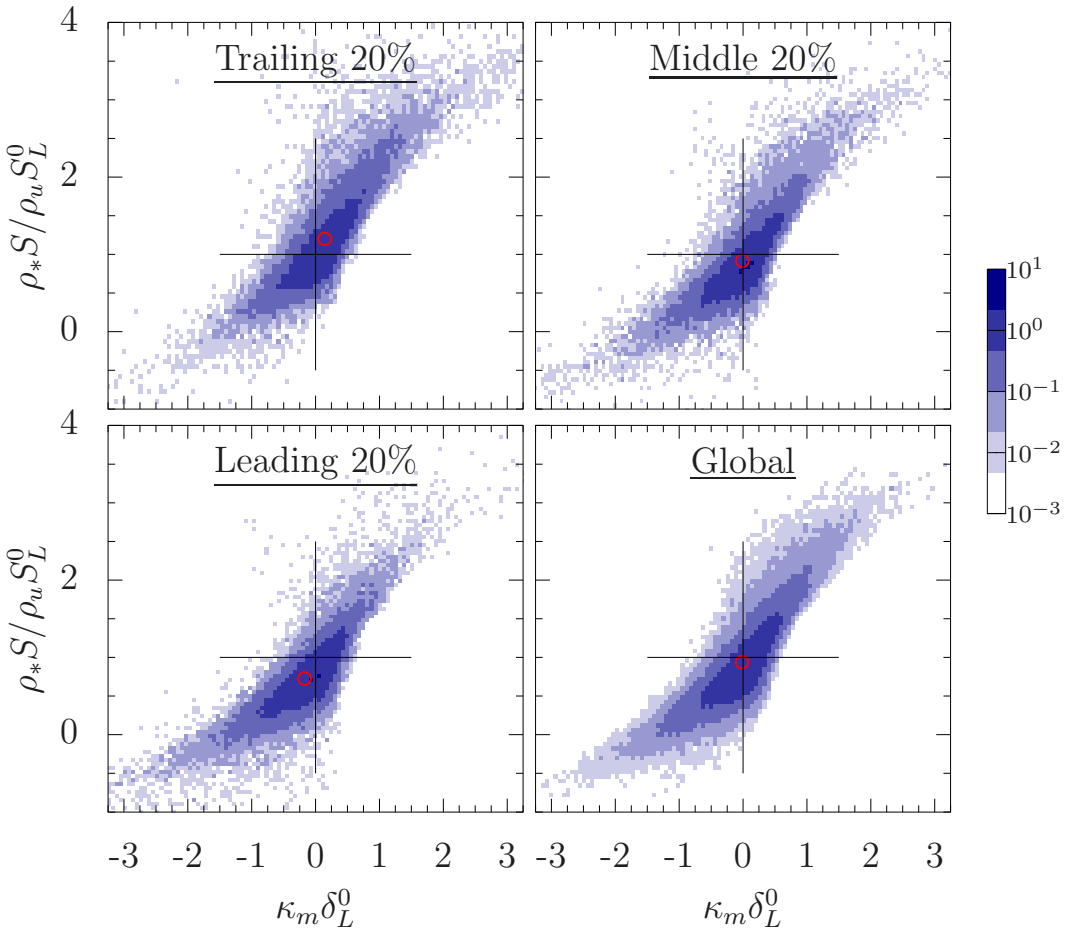

Figure 3.7: Joint probability density function of flame curvature and the gradient-weighted displacement speed across the brush. Trailing 25 percentile of the flame surface possess high positive curvature and displacement speed while the leading 25 percentile low speed and negative curvature.

The normalized, gradient-weighted mean displacement speed averaged over the entire surface is close to unity as expected. The surface-averaged mean flame curvature is negative, consistent with the topology of spherical flames. However the most probable value of curvature is positive, indicating that concave topology (i.e. ridges) is more commonly found than the convex

ones.

At the trailing edge, regions of high positive curvature and displacement speed have a higher probability density while at the leading edge regions of high negative curvature and low displacement speed are more commonly found. In general, the displacement speed and the curvature are negatively correlated with a high correlation coefficient. The mean of two quantities across the brush is plotted as a red curve on top of the joint-PDF. As the curvature distribution shifts from largely-positive at the trailing edge to largely-negative at the trailing edge, the conditional mean of the normalized, gradient-weighted displacement speed decreases as well.

This response of the displacement speed to changes in curvature is consistent with the Markstein effect [88, 84, 75], which is a linear theory that relates flame speed of to its stretch rate. The surface-weighed displacement speed can be modeled as

$$\langle S \rangle_w = \frac{\rho_u S_L}{\rho_*} \left(1 - \mathrm{Ma} \langle K \rangle_w \tau_L\right) \tag{3.33}$$

$$= \frac{\rho_u S_L}{\rho_*} \left(1 - \mathrm{Ma} \langle a \rangle_w \tau_L + 2\mathrm{Ma} \frac{\langle S \rangle_w}{S_L} \langle \kappa \rangle \delta_L + 2\mathrm{Ma} \tau_L \, \mathrm{covar}\{S_g, \kappa\}\right) \tag{3.34}$$

where $\mathrm{Ma} = \mathcal{L}/\delta_L$ is the Markstein number and $\mathcal{L}$ the Markstein length. The density ratio ρ_*/ρ_u compensates for the differences between displacement speed of iso-level $C = c^*$ and the laminar flame speed S_L. For the methane/air mixture under consideration, $\mathrm{Ma} \approx 0.33$ and was estimated from three-dimensional laminar spherical flame simulations at the same thermo-chemical conditions.

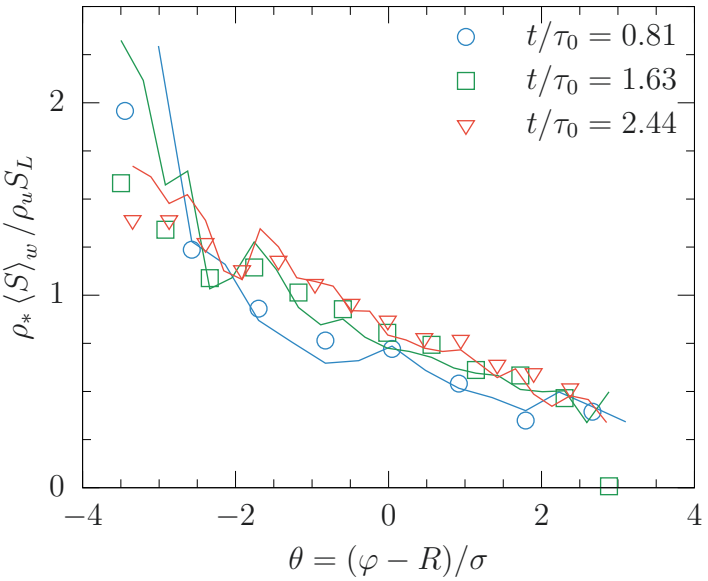

Figure 3.8: The normalized, gradient-weighted displacement speed across the flame brush, along with the prediction of Markstein model (Eq. (3.35)). Data shown for flame R3s at three different times.

Substituting the expression for stretch rate $\langle K \rangle_w$ in Eq. (3.34) the following expression for $\langle S \rangle_w$ is obtained:

$$\frac{\rho_* \langle S \rangle_w}{\rho_u S_L} = \frac{1 - \mathrm{MaKa}\left(\langle a \rangle_w - 2\mathrm{covar}\{S_g, \kappa\}\right)\tau_\eta}{1 - 2\mathrm{Ma}(\rho_u/\rho_*)\langle \kappa \rangle \delta_L}. \tag{3.35}$$

The tangential strain rate $\langle a \rangle_w$ is normalized with the instantaneous Kolmogorov time scale τ_η in accordance with its scaling for the deformation of material elements in isotropic turbulence [43]. A similar scaling is also shown to hold in premixed turbulent flames [71] also. Consistently, the Kolmogorov time scale τ_η is chosen to normalize the covariance term also and the Karlobvitz number $\mathrm{Ka} = \tau_L/\tau_\eta$ appears as a result.

Figure 3.8 shows that the Markstein model from Eq. (3.35) accurately

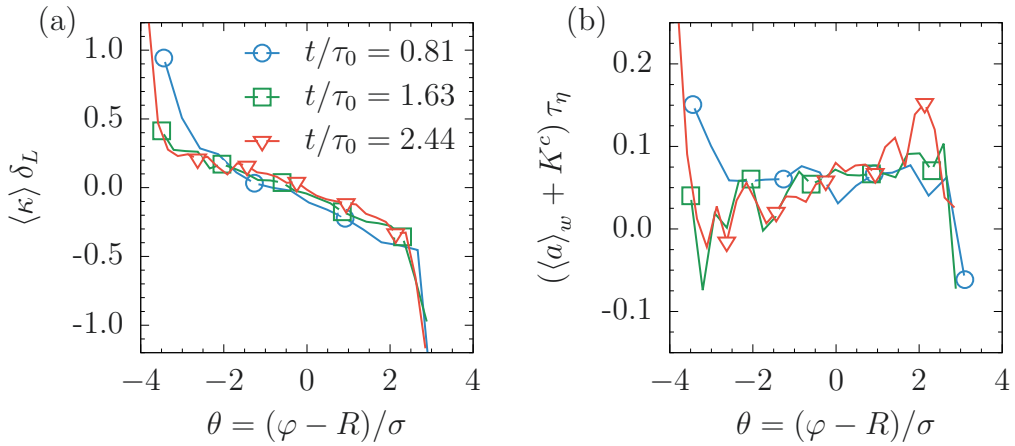

Figure 3.9: Spatial variation of mean curvature, strain rate $\langle a\rangle_w$ and covariance stretch component K^c. Stretch rates are normalized by the instantaneous Kolmogorov time scale τ_η. Representative data from three times for flame R3K1s is presented.

predicts the variation of the displacement speed across the brush. Data are presented at three different times for flame R3s (symbols) and compared with the predictions of the Markstein model with Ma = 0.33. At the leading and trailing edge of the brush, large curvature leads to large values of flame stretch rate and deviations from the linear Markstein model are observed. However, such differences may not affect the integral in the term T_4^b appreciably since $\hat{\mathcal{P}}\theta^2 \to 0$ at the edges of the brush.

The two stretch components and mean curvature across the brush are shown in Fig. 3.9. The tangential strain rate and the covariance stretch terms normalized by instantaneous Kolmogorov time scale are spatially homogeneous across the brush, while mean flame curvature changes significantly. According to Eq. (3.35), the variation in displacement speed thus originates in response to

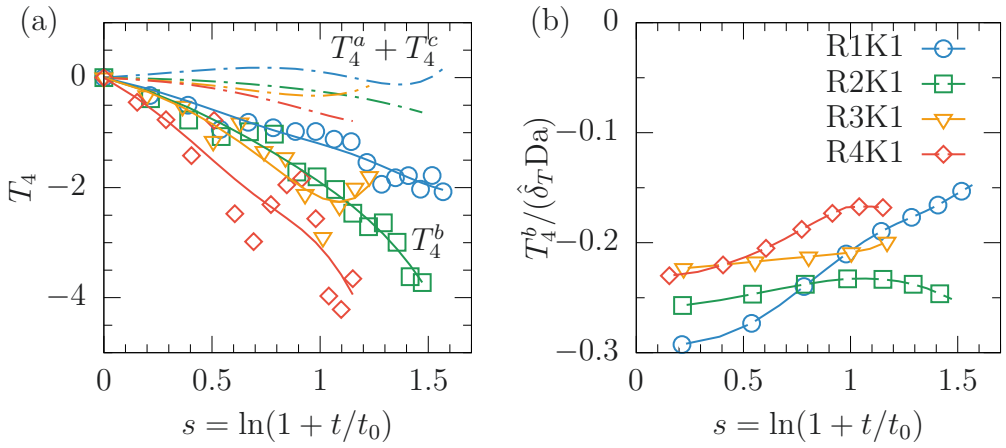

Figure 3.10: (a) Differential flame stretch terms $\Pi_4^a + \Pi_4^c$ and Π_4^b in Eq. (3.12) for all flames in the database. DNS data for Π_4^b are shown in symbols, along with a smooth trend-line (lines with same color). (b) Π_4^b compensated by $\hat{\delta}_T$ Da as suggested by Eq. (3.36).

that in flame curvature. As discussed earlier, the variation of flame curvature across the brush is a fundamental property of closed flame surface, the variation of displacement speed across the brush is expected in different turbulent flame configurations also. As a result, the differential flame stretch mechanism is expected to adversely affect the growth of flame brush in general.

Substituting $\langle S \rangle_w$ from Eq. (3.35) in Eq. (3.31), a model for term T_4^b is obtained:

$$T_4^b = -n\hat{\delta}_T \mathrm{Da} \int_{-R/\sigma}^{\infty} d\theta \hat{\mathcal{P}}\, \theta^2 \left(\frac{\rho_u}{\rho_*} \frac{1 - \mathrm{MaKa}\tau_\eta \left(\langle a \rangle_w - 2\mathrm{covar}\{S_g, \kappa\} \right)}{1 - 2\mathrm{Ma}(\rho_u/\rho_*) \langle \kappa \rangle \delta_L} \right), \tag{3.36}$$

where the Damköhler number $\mathrm{Da} = \tau/\tau_L$ originates from the choice of normalizing scales.

Since reference scales and dimensionless groups inside the integrand of

Eq. (3.36) are constant or evolve similarly across flames R1K1, R2K1, R3K1 and R4K1, term T_4^b should increase with the flame brush thickness $\hat{\delta}_T$ and proportionally with the Damköhler number.

Figure 3.10 plots the three differential stretch terms T_4^a, T_4^b and T_4^c. Terms T_4^a and T_4^c contribute very little to the evolution of the brush, since the corresponding stretch components are approximately constant through the brush. Magnitude of T_4^b is higher for flames with higher Reynolds (and Damköhler) number.

For most part, the absolute value of T_4^b increases in time proportional to the normalized brush thickness $\hat{\delta}_T$. As with the mean velocity term T_2, flame stretch effects are negligible early on when turbulent diffusion is the dominant mechanism. With growing brush thickness the differential flame stretch effects become prominent and hinder the growth of the brush. However, the magnitude of T_4 continues to increase even after $\hat{\delta}_T$ reaches an asymptotic value. This residual temporal variation may be due to deviations of the surface-averaged displacement speed from the Markstein theory, variation in the normalized curvature $\langle\kappa\rangle\,\delta_L$ or other transient effects.

Overall, the models presented for $\langle S\rangle_w$ and T_4^b here highlight the role of the Markstein number in the growth of the flame brush thickness. Since a lower Markstein number leads to a smaller variation of $\langle S\rangle_w$ for similar changes in $\langle\kappa\rangle$, the model predicts a lower magnitude of T_4 for smaller Markstein number. While the present database does not explore such dependence, Fairweather et. al. [36] do indeed report that methane-hydrogen mixtures with lower Markstein

number burn faster than explained by changes in the laminar flame speed alone. Based on the above discussion, it may be postulated that this might be due to a smaller contribution of T_4 towards hindering the growth of the brush. A thicker turbulent flame brush would lead to higher turbulent flame speed due to larger area increase.

Several researchers have investigated the effect of hydrodynamic instabilities in the growth of turbulent flame surface area [39, 27, 124]. It has been demonstrated that in the presence of Darrieus-Landau (DL) hydrodynamic instabilites, the PDF of curvature departs from a Gaussian distribution and exhibits a negative skewness [27]. When hydrodynamic instabilities play a significant role in development of a turbulent flame, the changes to curvature statistics across the brush will affect differential stretch rate terms and influence the evolution of the brush. Such effects are minimal at present due to large values of u'/S_L but may be important in general.

3.2.4 Evolution of turbulent flame brush thickness

As discussed in this chapter, the temporal growth of the brush of turbulent spherical flames is controlled by several mechanisms. Figure 3.11 compares the evolution of the normalized brush thickness $\hat{\delta}_T$ across different flames and against the modified dispersion relation. The dimensional flame brush thickness δ_T changes by a factor of four from flame R1K1 to R4K1, yet the normalized thickness $\hat{\delta}_T$ evolves similarly. This demonstrates that the integral length scale l is the most appropriate normalizing scale for the thickness of

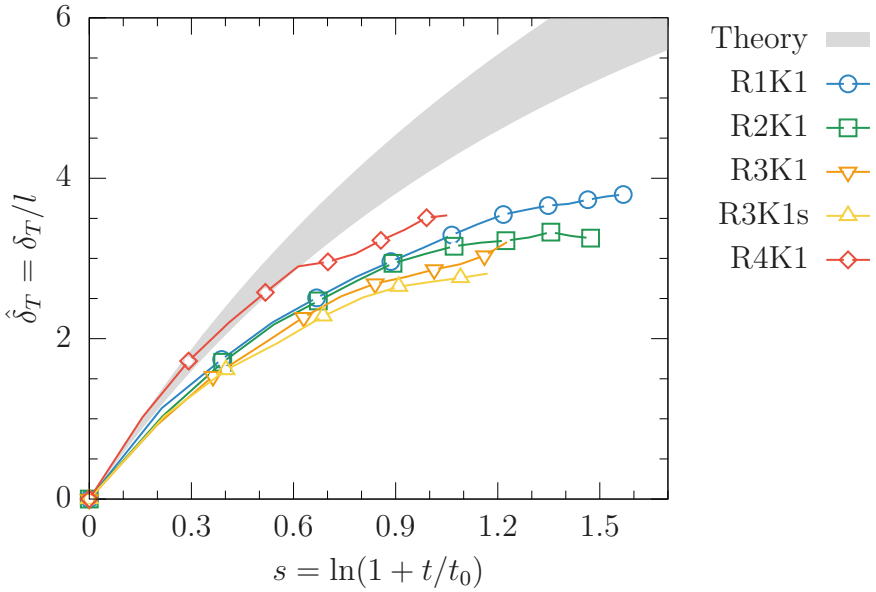

Figure 3.11: Comparison of normalized flame brush thickness $\hat{\delta}_T = \delta_T/l$ (lines with symbols) against predictions of Taylor's theory.

turbulent flame brush, even though reactants' turbulence decays freely and in the presence of mechanisms in addition to turbulent dispersion.

The shaded region in Fig. 3.11 shows the predictions of the modified dispersion relation for the range of values of the decay exponent n as observed in the database. A better agreement between the two is seen early on as the initial growth of the turbulent brush is governed by turbulent dispersion. More significant differences appear later as the mean velocity gradient and differential flame stretch terms increase in magnitude. The normalized turbulent flame brush thickness appears to reach an asymptotic value, contrary to the thickness of region occupied by material points, which continues to grow indefinitely even in decaying isotropic turbulence [48].

A characterization of the various terms points to universal mechanisms that are likely to apply in other flame configurations. It was observed that the role of turbulent dispersion weakens in time compared to other effects. This decline is due to the de-correlation of the velocity fluctuation experienced by the flame surface elements, consistent with Taylor's theory. Thus, a similar behavior is also expected in statistically stationary homogeneous isotropic turbulence.

On the other hand, differential flame stretch and mean velocity terms become more important as the thickness of turbulent flame brush increases due to differences in the mean velocity and flame stretch across the brush are amplified. This can be seen in Eq. (3.12) since T_2 and T_4 are directly proportional to the thickness $\hat{\delta}_T$ itself. Based on the preliminary characterization of expanding spherical turbulent flames from the present database, the latter (term T_4) seems to dominate the former (term T_2). The analysis presented in this chapter seems to indicate that the thickness of turbulent flame brush may not increase indefinitely and may attain an asymptotic or a maximum value.

Chapter 4

The peak flame surface density

4.1 Peak SDF in thin reaction zone regime

As discussed in Sec. 2.3 and shown in Fig. 2.8, the flame surface density function peaks in the central region of the turbulent flame brush and decreases rapidly towards the edges of the brush. The expression for the surface density function for isosurface $C = c^*$ is re-written below for reference:

$$\Sigma(C = c^*; r, t) = \left\langle |\nabla C| \middle| C = c^* \right\rangle \mathcal{P}_C(c^*; r, t). \tag{4.1}$$

In general, the spatial variation of the surface density function may be due to that in the conditional gradient magnitude or the PDF of the progress variable $\mathcal{P}_C(c^*)$, or both.

Figure 4.1(a) shows the conditional mean of the magnitude of progress variable gradient as a function of the conditioning value c at two times for flame configuration R2K1. The two representative checkpoints $t/\tau_0 = 0.75$

The content presented in this chapter has been published in the following two articles:

Kulkarni, T., Buttay, R., Kasbaoui, M., Attili, A., & Bisetti, F. (2021). Reynolds number scaling of burning rates in spherical turbulent premixed flames. *J. Fluid Mech.*, 906, A2. https://doi.org/10.1017/jfm.2020.784

Kulkarni, T., Bisetti, F. (2021). Evolution and scaling of the peak flame surface density in spherical turbulent premixed flames subjected to decaying isotropic turbulence. *Proc. Combust. Inst.*, 38(2), 2817-2824. https://doi.org/10.1016/j.proci.2020.06.042

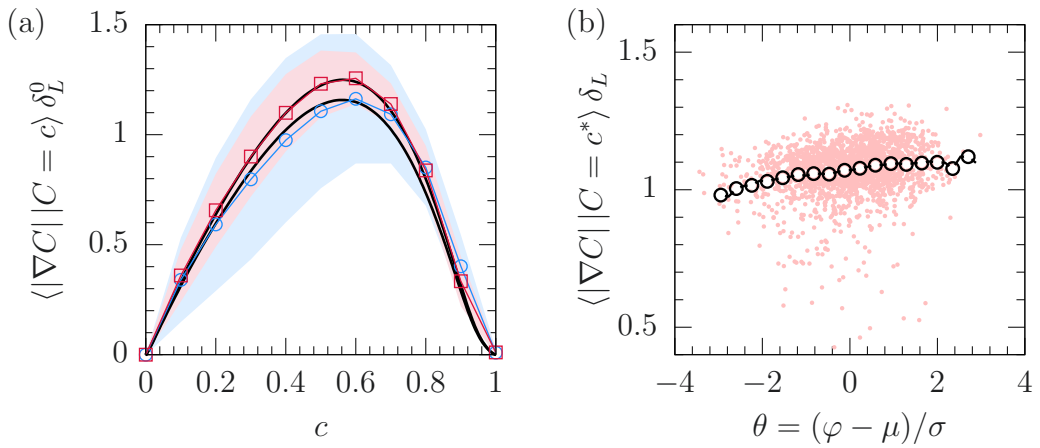

Figure 4.1: (a) DNS data for the conditional mean of gradient magnitude at two different times. The shaded regions mark one standard deviation around the mean. (b) Conditional mean of the gradient magnitude across the flame brush at $t/\tau_0 = 5.25$. Scatter of samples is represented with red dots. Data presented for flame configuration R2K1.

(blue color) and 5.25 (red color) are chosen to represent data from early and late stages of the evolution. Also shown for comparison are the curves from a laminar flame front at the corresponding temperature and pressure (black lines), which increase in time due to isentropic compression. The red and blue color hues mark one standard deviation from the mean.

The conditional mean of the gradient at all values of c is same as its value in a laminar flame, confirming that the flame configuration belongs to thin flamelet regime [87] where the structure of propagating front is retained in the mean. Furthermore, since the data are normalized with the initial thermal thickness δ_L^0, the effect of increasing pressure on the front can be observed also. Since the peak value of the gradient changes by 10% only, it is demonstrated that the effect of increasing pressure on the flame structure is negligible.

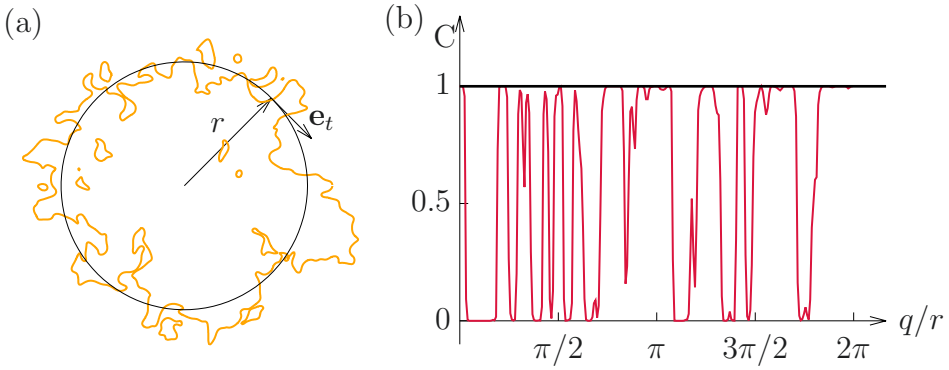

Figure 4.2: Flame surface crossings in a plane for flame R2K1 at $t/\tau_0 = 4.5$. (a) A planar cut of the flame surface $C = c^*$. (b) Progress variable field along the circle of radius r versus the normalized arc length q/r.

More importantly, figure 4.1(b) shows the radial variation of the gradient magnitude at isosurface $C = c^*$ is minimal, indicating that the conditional gradient magnitude component of Eq. (4.1) may be considered constant for all practical purposes. The spatial and temporal variation of the surface density function is then primarily due to the PDF $\mathcal{P}_C$. The peak flame surface density function is thus intricately tied to that of the PDF and further investigation of the spatial and temporal dependence of $\mathcal{P}_C$ is warranted.

The investigation follows an approach inspired by the Bray-Moss-Libby model [16]. Consider an ensemble of two-dimensional planar cuts, whereby each plan contains the origin and its normal is oriented randomly. On each such planar cut, consider a circle of radius r, centered at the origin and let $\mathbf{e}_t$ be the unit vector along the tangential direction. Let q be the arc length distance from an arbitrary point along the circle ($0 \leq q \leq 2\pi r$).

Figure 4.2 shows a schematic representation of one such planar cut.

The progress variable profile at one particular radial distance is shown as a function of the coordinate q in subplot (b).

Given the spherical symmetry of the statistics, the progress variable C and its gradient ∇C are ergodic along $\mathbf{e}_t$. The probability $\mathbb{P}_C$ that C takes a value between $c - dc/2$ and $c + dc/2$ on the circle equals

$$\mathbb{P}_C[c - dc/2 \leq C \leq c + dc/2] = \mathcal{P}_C(c; r, t)\, dc = \frac{1}{2\pi r p} \sum_{j=1}^{p} \sum_{i=1}^{m_j} dq_{ij}, \qquad (4.2)$$

where dq_{ij} is an infinitesimal arc length centered at location q_{ij} such that $C(q_{ij}) = c$ and $c - dc/2 \leq C(q) \leq c + dc/2$ for $q_{ij} - dq_{ij}/2 \leq q \leq q_{ij} + dq/2$.

Since many such segments may exists on a single plane, the segment length is summed over m_j segments along plane j ($j = 1, \ldots, p$) and p denotes an arbitrarily large number of planes considered for such average. Similar to the nomenclature used in the Bray-Moss-Libby (BML) model [15, 63], each of the q_{ij} locations is referred to as a 'flame crossing'.

The infinitesimal arc length dq_{ij} is related to the projection of the gradient ∇C onto the tangential unit vector $\mathbf{e}_t$ at the flame crossing i with circle of radius r on plane j:

$$dq_{ij} = dc/|\nabla C \cdot \mathbf{e}_t|_{ij}. \qquad (4.3)$$

Let m be the total number of flame crossings summed over all planes. Rearranging Eq. (4.2) and dividing by dc, the following expression for the PDF

$\mathcal{P}_C$ is obtained:

$$\mathcal{P}_C(c;r,t) = \frac{m}{2\pi rp}\frac{1}{m}\sum_{j=1}^{p}\sum_{i=1}^{m_j}|\nabla C\cdot\mathbf{e}_t|_{ij}^{-1} \tag{4.4}$$

$$= \varpi(r,t)\left\langle|\nabla C\cdot\mathbf{e}_t|^{-1}\middle|C=c\right\rangle, \tag{4.5}$$

where $\varpi(r,t) = m(r,t)/2\pi rp$ is the flame crossing frequency, defined as number of flame crossings per unit length. The statistical mean of $|\nabla C\cdot\mathbf{e}_t|^{-1}$ over all crossings at a fixed radial distance is simply its conditional mean at the iso-surface $C=c$.

Since the expression for Σ involves the product of the PDF $\mathcal{P}_C$ and the conditional mean of the gradient magnitude $|\nabla C|$, it is beneficial to relate the conditional mean of $|\nabla C\cdot\mathbf{e}_t|^{-1}$ to the inverse of the conditional mean:

$$\left\langle|\nabla C\cdot\mathbf{e}_t|^{-1}\middle|C=c\right\rangle = \Upsilon\left\langle|\nabla C\cdot\mathbf{e}_t|\middle|C=c\right\rangle^{-1}, \tag{4.6}$$

where the correction factor Υ is implicitly defined in the equation above.

A binomial series expansion relates Υ to the statistics of gradient projection as

$$\Upsilon = 1 + \mathrm{Var}\left\{|\nabla C\cdot\mathbf{e}_t|\middle|C=c\right\}\left\langle|\nabla C\cdot\mathbf{e}_t|\middle|C=c\right\rangle^{-2} + \ldots \tag{4.7}$$

For turbulent flames in the thin reaction zone regime, the structure of the reactive layer is unaffected by reactant side turbulence and the variance of the gradient projection is small compared to the square of its mean ($\Upsilon \to 1$). As will be shown below, the Bray-Moss-Libby model for the flame surface density based on the flame crossing frequency is recovered for $\Upsilon = 1$. The factor Υ is

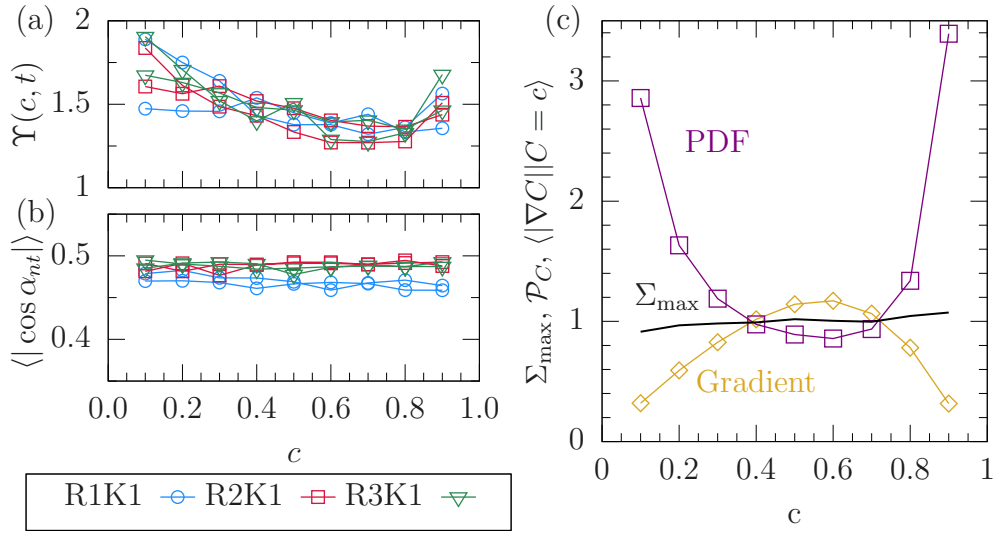

Figure 4.3: (a) The correction factor Υ, (b) The alignment cosine for three flame configurations and (c) The peak surface density function $\Sigma_{\max}(c)$ for various values of c along with the two componets for flame R2K1 at $t/\tau_0 = 5.2$.

thus serves as a correction factor for the BML model for turbulent flames in the thin reaction zone regime. For various flame configurations in the database, $\Upsilon \approx 1.35$ for $0.5 \leq c \leq 0.9$, as shown in Fig. 4.3 (a).

The surface of turbulent spherical flame is randomly oriented with respect to the radial and tangential unit vectors $\mathbf{e}_r$ and $\mathbf{e}_t$. Moreover, the statistics of the magnitude of the gradient of C are isotropic and uncorrelated with the flame orientation and the following simplification is possible:

$$\begin{aligned}\left\langle |\nabla C \cdot \mathbf{e}_t| \middle| C = c \right\rangle &= \left\langle |\nabla C||\mathbf{n} \cdot \mathbf{e}_t| \middle| C = c \right\rangle \\ &\approx \left\langle |\nabla C| \middle| C = c \right\rangle \left\langle |\mathbf{n} \cdot \mathbf{e}_t| \middle| C = c \right\rangle .\end{aligned} \tag{4.8}$$

With this simplification, the expression for $\mathcal{P}_C$ reads

$$\mathcal{P}_C(c;r,t) = \frac{\varpi(r,t)\Upsilon}{\left\langle |\nabla C| \middle| C = c \right\rangle \left\langle |\cos\alpha_{nt}| \middle| C = c \right\rangle}, \tag{4.9}$$

where α_{nt} is the angle between the normal $\mathbf{n}$ and the ergodic unit vector $\mathbf{e}_t$ and represents the orientation of flame surface with respect to the ergodic direction. The orientation angle α_{nt} stays nearly constant in time, independent of the conditioning value c and same across different simulations (see Fig. 4.3 (b)).

Figure 4.3(c) shows the peak flame surface density $\Sigma_{\max}(c)$ for a general isosurface $C = c$, normalized by $\Sigma_{\max}(c^*)$ at a given time. Within the range of values $0.1 \leq c \leq 0.9$, the peak flame surface density function is fairly insensitive to the choice of the iso-level, since $\mathcal{P}_C \sim \left\langle |\nabla C| \middle| C = c \right\rangle^{-1}$, while Υ and the alignment cosine are roughly constant.

Based on the above simplifications, an approximate expression for the surface density function is given by

$$\Sigma(c; r, t) = \varpi(r, t)\Upsilon / \left\langle |\cos \alpha_{nt}| \middle| C = c \right\rangle . \tag{4.10}$$

Figure 4.4 compares the left and right-hand sides of Eq. (4.10) for $c = c^* = 0.73$, where the surface density evaluation on the left hand side is evaluated with the definition from Eq. (2.34). The two are found to be in good agreement. Since the factor $\Upsilon / \langle |\cos \alpha_{nt}| \rangle$ is approximately constant in space, time and across flame configurations, the spatial and temporal dependence of Σ emerges primarily due to that of the flame crossing frequency $\varpi = \varpi(r, t)$.

This conclusion is consistent with the BML theory, whereby the surface density function is modeled in terms of the spatial crossing frequency and a mean cosine factor $\Sigma_{\mathrm{BML}} = \varpi / \langle |\cos \alpha_{nt}| \rangle$ [14, 13]. Equation (4.10) has the

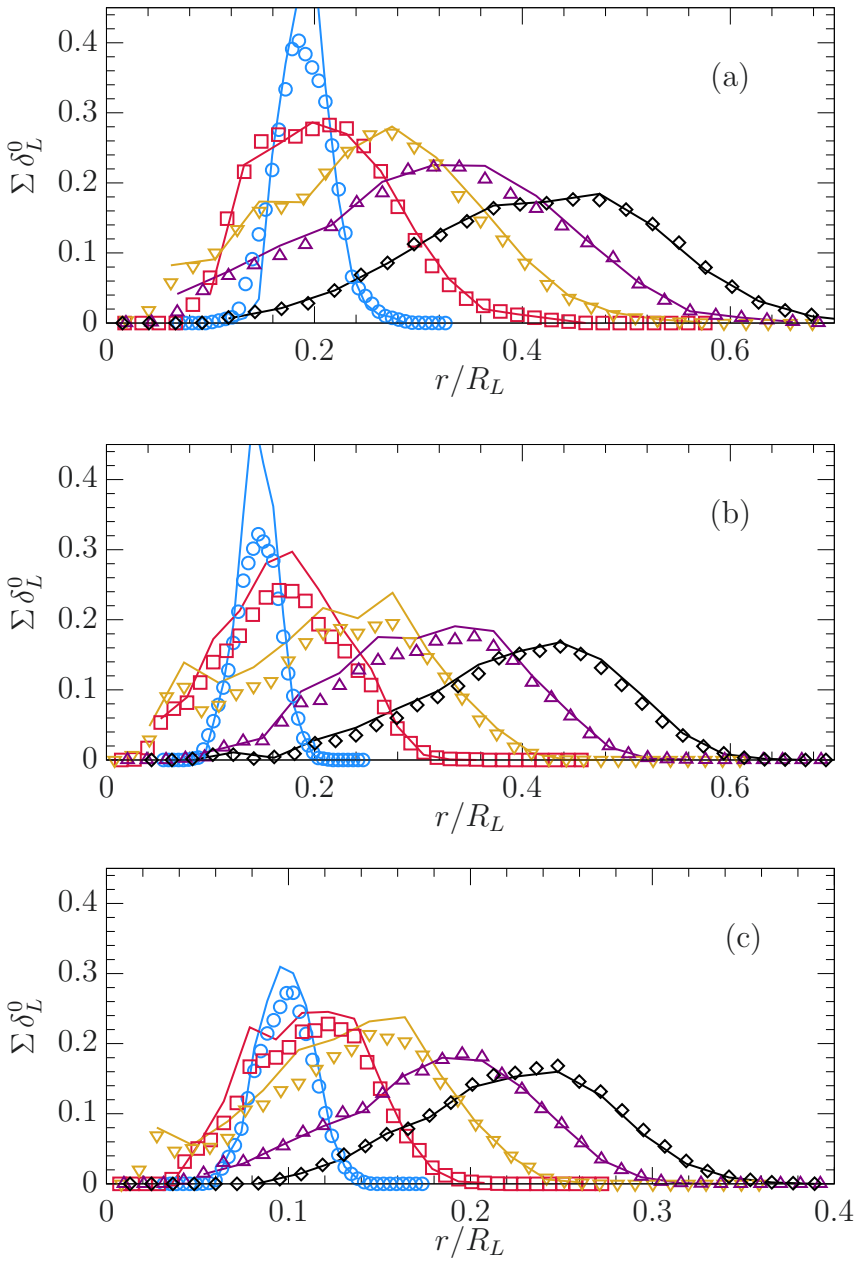

Figure 4.4: Comparison between the two expressions for Σ in Eq. (2.34) and the BML model Eq. (4.10) for three flames at five different times: (a) R1K1, (b) R2K1 and (c) R3K1. Time increases from left to right.

same form but includes the correction factor Υ additionally, which provides a correction for the fact that the premixed flames are not infinitesimally thin.

For a statistically stationary and planar turbulent premixed flame, the BML model relates the crossing frequency ϖ to the two-point, one-time auto-correlation function of the reaction progress variable,

$$\mathcal{F}(q; x_1) = \langle C'(\mathbf{x}, t)\, C'(\mathbf{x} + q\mathbf{e}_t, t\rangle \,/\sigma_C^2, \tag{4.11}$$

$$\varpi = \varpi(x_1) = -2\frac{\partial \mathcal{F}}{\partial q}\Big|_{q=0}. \tag{4.12}$$

Here, x_1 is an inhomogeneous coordinate, normal to the ergodic plane of the planar turbulent flame. All statistical quantities depend on the flame-normal direction x_1 only and are averaged in the ergodic directions. In Eq. (4.11) $C' = C - \overline{C}$ is the Reynolds fluctuation, $\sigma_C^2 = \overline{C'^2}$ the variance and $\mathbf{e}_t$ the unit vector in plane of the flame that identifies an ergodic direction. In other words, the two-point auto-correlation function is evaluated with samples taken in ergodic direction where statistics are spatially invariant.

Under specific assumptions on the functional form of the two-point scalar auto-correlation function $\mathcal{F}$, the crossing frequency and surface density function are modeled as

$$\varpi = A_\varpi\, \overline{C}(1 - \overline{C})/L^*, \tag{4.13}$$

$$\Sigma = A_\Sigma\, \overline{C}(1 - \overline{C})/L^*, \tag{4.14}$$

where $\overline{C} = \overline{C}(x_1)$ only, A_ϖ and A_Σ are modeling constants of order unity and L^* is the so-called *wrinkling scale*.

Since the crossing frequency is closely related to the auto-correlation function of the progress variable, L^* likely reflects the entire spectrum of the progress variable field $C(\mathbf{x}, t)$, although it is not clear how L^* should scale with the Reynolds number and how a suitable autocorrelation length could be defined from $\mathcal{F}$.

There exists significant controversy on the origin and scaling of the wrinkling length-scale in the literature. Cant & Bray [18] proposed the following closure for the wrinkling scale,

$$L^* \propto k^{3/2}\epsilon^{-1}, \tag{4.15}$$

thereby advancing the hypothesis that the wrinkling scale is proportional to the integral length scale defined as $l = u'^3/\epsilon$ and controlled by energy containing fluid structures of the turbulent motion, rather than scales associated with flame structure and its propagation.

Deschamps *et. al.* [31] observed $L^* \approx l$ for conical turbulent premixed flames, while others [118, 101] found the wrinkling scale to be about five times smaller than the integral scale for V-shaped and planar turbulent premixed flames. Contrary to these observations, Shy *et. al.* [101] also reported that the wrinkling scale remained constant for two different turbulence intensities, while the integral scale changed by about 50%. In must be noted that such experimental investigations of flame surface wrinkling scale may be affected by inadequate resolution of the turbulent flame surface, since the wrinkling scale was found to be about the same size as the width of the averaging box

used for the measurement of the flame surface density function. Dependence of L^* on turbulence intensity u'/S_L has also been postulated, yet no conclusive evidence exits.

Given that L^* and $1/\Sigma$ are related to within constants of order unity, let $L^* = (4\Sigma_{\max})^{-1}$, where $\Sigma_{\max}$ denotes the peak flame surface density within the brush. The factor of four is included here so as to be consistent with Eq. (4.14), according to which the surface density function peaks at $\overline{C} = 0.5$. Since $L^* \propto \Sigma_{\max}$, both quantities obey the same scaling relations.

The analysis of this section points to a hydrodynamic scaling of wrinkling length scale, such that its separation with the integral scale l increases with increasing Reynolds number as $l/L^* \sim \mathrm{Re}_\lambda^{1.13}$. Such power law scaling is typical of hydrodynamic length scales of turbulent motion, such as Taylor scale λ and Kolmogorov scale η. Since the peak flame surface density is controlled by the transport and flame stretch mechanisms, the said scaling is investigated in detail in the following sections.

4.2 Evolution equation for $\Sigma_{\max}$

A more detailed investigation of the peak flame surface density, wrinkling scale and its scaling with Reynolds number is investigated by considering the evolution equation for $\Sigma_{\max}$. Recall that the surface density transport equation, simplified for spherical flames reads

$$\frac{\partial \Sigma}{\partial t} + \frac{1}{r^2}\frac{\partial}{\partial r}\left(r^2 \left\langle u_r + S n_r \right\rangle_w \Sigma\right) = \left\langle K \right\rangle_w \Sigma, \tag{4.16}$$

where u_r and n_r denote the radial components of the velocity and surface normal vectors, respectively.

The evolution equation for the peak surface density $\Sigma_{\max}$ is obtained by evaluating the equation above at the radial location of the peak, $\hat{r}(t)$, where $\partial\Sigma/\partial r = 0$. However, the statistical noise inherent to the evaluation of the surface density function from Eq. (2.34) affects both the determination of both the location $\hat{r}(t)$ and the peak value.

To avoid the statistical noise from affecting the balance terms for peak flame surface density, the peak location is evaluated based on the Gaussian model as in Eq. (2.67) and is re-written below for reference:

$$\hat{r} = R\left(1 + \sqrt{1 - 8\alpha^2}\right)/2. \tag{4.17}$$

Since the ratio $\alpha = \sigma/R$ is small at all times, it follows that the surface density peaks close to the mean radial location, $\hat{r} \approx R$.

The evolution equation for the peak $\Sigma_{\max} = \Sigma(\hat{r}(t), t)$ is obtained by evaluating Eq. (4.16) at $\hat{r}(t)$ and reads

$$\frac{1}{\Sigma_{\max}}\frac{d\Sigma_{\max}}{dt} = \left\{-\frac{1}{r^2}\frac{\partial}{\partial r}\left(r^2\left\langle u_r + Sn_r\right\rangle_w\right) + \left\langle K\right\rangle_w\right\}_{\hat{r}(t)} \tag{4.18}$$

Note that $\Sigma_{\max} = \Sigma_{\max}(t)$ only and the source terms on the right hand side are evaluated at $\hat{r}(t)$.

As with the evolution equation for the turbulent flame brush thickness, a dimensionless form of Eq. (4.18) is obtained by transforming time t to logarithmic time coordinate $s = \log(1 + t/t_0)$ and radial distance r to brush

coordinate $\theta = (r - R)/\sigma$ to facilitate comparison across different flame configurations. The dimensionless form of Eq. (4.18) reads

$$\begin{aligned}\frac{d\log\Sigma_{\max}}{ds} = &-\frac{n\tau}{\sigma\hat{r}^2}\left\{\frac{\partial}{\partial\theta}(\theta\sigma+R)^2\left\langle u_r'\right\rangle_w\right\}_{\hat{\theta}} - \frac{n\tau}{\sigma\hat{r}^2}\left\{\frac{\partial}{\partial\theta}(\theta\sigma+R)^2\overline{u}_r\right\}_{\hat{\theta}} \\ &-\frac{n\tau}{\sigma\hat{r}^2}\left\{\frac{\partial}{\partial\theta}(\theta\sigma+R)^2\left\langle Sn_r\right\rangle_w\right\}_{\hat{\theta}} + n\tau\left\langle K\right\rangle_w(\hat{\theta},s)\end{aligned} \tag{4.19}$$

where the derivative with respect to θ is taken while holding time s constant, although θ is a function of both r and t. The source terms are evaluated at $\hat{\theta} = (\hat{r} - R)/\sigma$, the time-varying location of the peak flame surface density in the normalized brush coordinate.

As with the evolution equation for the flame brush thickness, the contributions of the mean velocity field and turbulent fluctuations are separated using the Reynolds decomposition $u_r = \overline{u}_r + u_r'$. Recall that the surface weighted average $\left\langle u_r'\right\rangle_w \neq 0$ since $\overline{u}_r$ is the *unconditional* mean radial velocity.

The four terms on the right hand side of Eq. (4.19) represent four mechanisms that affect the evolution of the peak flame surface density: turbulent transport (term Π_1), mean radial transport (term Π_2), propagation (term Π_3) and flame stretch (term Π_4).

The four terms are shown in Fig. 4.5 for flame R2K1. All transport terms (Π_1, Π_2 and Π_3) contribute to the reduction of the peak by transporting the surface density away from the location of the peak. The turbulent transport term (Π_1) dominates early on, but the mean transport term (Π_2) surpasses it later on as turbulence decays with time. The propagation term (Π_3) has only a minor influence on the evolution of peak surface density and

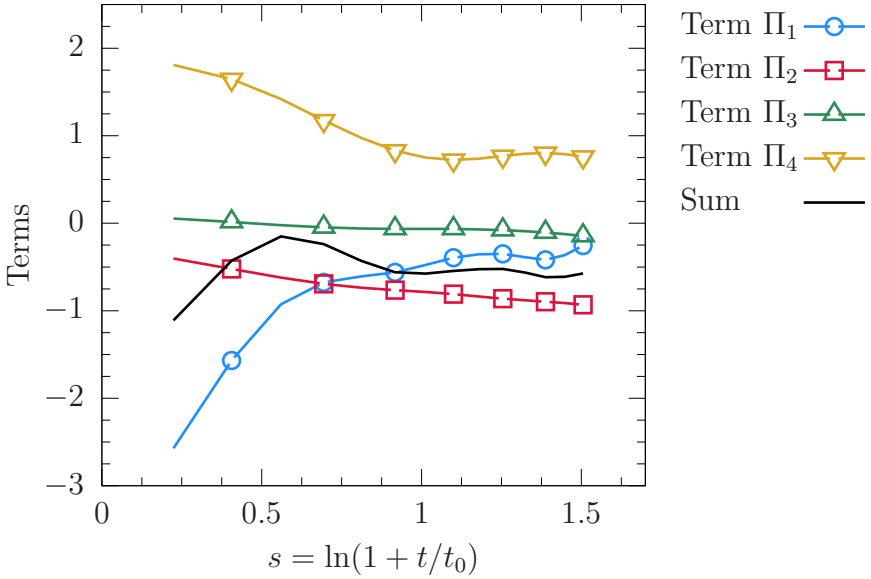

Figure 4.5: Terms in the evolution equation Eq. (4.19) of the peak flame surface density for flame configuration R2K1.

its role is primarily to changes in the radial location of the peak, $\hat{r}(t)$. On the other hand, flame stretch term is always positive, increasing the peak surface density by small-scale wrinkling. The balance of the transport and stretch terms leads to an approximately constant rate of logarithmic decay of peak flame surface density (black line in Fig. 4.5).

Terms Π_1, Π_2 and Π_4 are analyzed in detail in the following subsections and their scaling with appropriate turbulence scales is discussed.

4.2.1 Turbulent transport

Figure 4.6(a) shows the evolution of the absolute value of term Π_1 across various flame configurations. The evolution of this term in logarithmic time

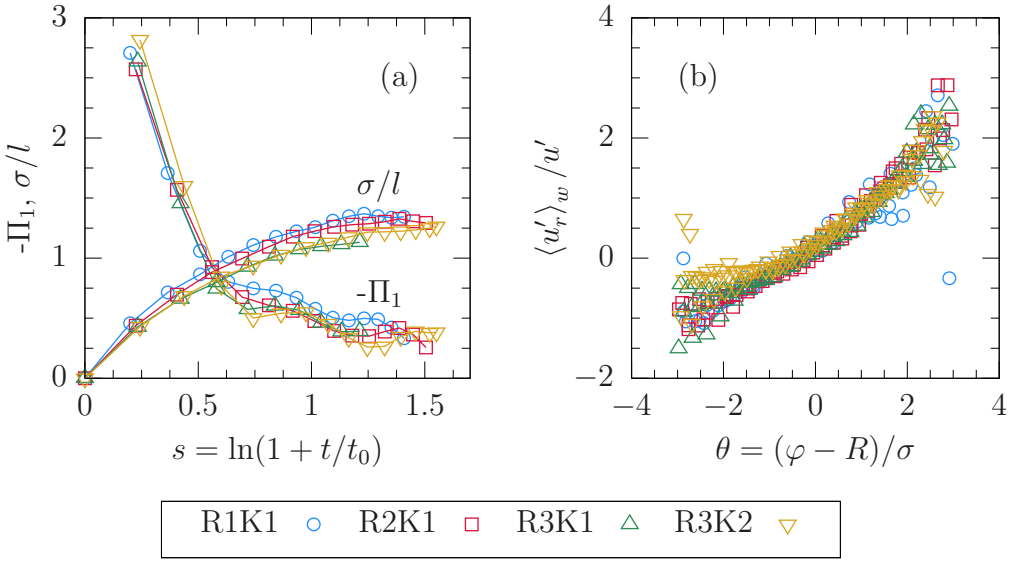

Figure 4.6: (a) The turbulent transport term Π_1 of Eq. (4.19) and the normalized standard deviation σ/l and (b) the surface-weighted radial velocity component $\langle u_r' \rangle_w / u'$.

coordinate s is similar across different flames, even though the rms turbulence fluctuation u' is different.

To explain this observation, consider the following decomposition of Π_1:

$$\Pi_1 = -\frac{n\tau}{\sigma} \left\{ \frac{2 \langle u_r' \rangle_w \sigma}{\theta\sigma + R} + \frac{\partial \langle u_r' \rangle_w}{\partial\theta} \right\}_{\hat{\theta}}. \tag{4.20}$$

Figure 4.6(b) shows the surface averaged radial fluctuation $\langle u_r' \rangle_w$, normalized by the rms turbulence fluctuation $u'(t)$ at three instants for various flames.

Although, as discussed in earlier Sec. 3.2.1, the normalized fluctuation $\langle u_r' \rangle_w / u'$ changes with time at the leading and trailing edges of the brush due to de-correlation of velocity, the slope of $\partial \langle u_r' \rangle_w / \partial\theta$ in the central region ($\theta = 0$) is the same. Since the flame surface density peaks close to the mean

radial location $\hat{\theta} \approx 0$ where $\langle u_r' \rangle_w \approx 0$, term Π_1 is approximately

$$\Pi_1 \approx -\frac{3}{2}\frac{l}{\sigma}\left\{\frac{\partial \langle u_r' \rangle_w / u'}{\partial \theta}\right\}_{\hat{\theta}}, \tag{4.21}$$

since $\tau u' = 3u'^3/2\epsilon = 3l/2u'$. As demonstrated in Fig. 4.6(b), the term inside braces is unchanged across flames and in time and the temporal variation in Π_1 is inversely proportional to the normalized standard deviation σ/l. Since the evolution of normalized standard deviation σ/l in s is nearly identical across different flame configurations, term Π_1 is similar also.

4.2.2 Mean radial transport

The propagation of the reactive front induces a mean radial velocity due to thermal expansion across the flame. The gradient of the mean radial velocity thus induced in turn affects the peak surface density through term Π_2.

The expression for term Π_2 reads

$$\Pi_2 = -\frac{n\tau}{\sigma \hat{r}^2}\left\{\frac{\partial}{\partial \theta}(\theta\sigma + R)^2 \overline{u}_r\right\}_{\hat{\theta}} \tag{4.22}$$

and involves the evaluation of the gradient of mean radial velocity at the peak location.

The mean velocity profile and its gradient may be obtained by appropriately modeling the Reynolds average continuity equation as in Sec. 3.2.2. The mean velocity gradient and term Π_2 scale with the difference of radial velocity between the leading and trailing edge of the brush.

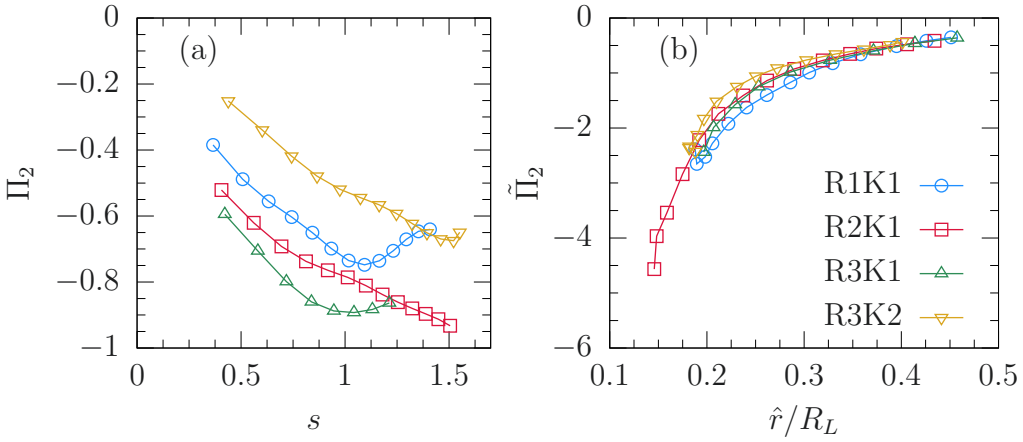

Figure 4.7: Mean radial transport of surface density at the peak location: (a) Term Π_2 of Eq. (4.19) and (b) Scaled term $\tilde{\Pi}_2$ with proposed scaling relation.

For the purposes of identifying relevant scaling relation for Π_2, consider the Reynolds-averaged continuity equation in reactants and products, where density is spatially uniform and an exact solution is available. The solution for mean radial velocity in reactants and products is given by (see Sec. 2.3.2)

$$\overline{u}_r(r,t) = \begin{cases} -\dfrac{R_L}{3\gamma_b p}\dfrac{dp}{dt}\left(\dfrac{r}{R_L}\right) & \text{Products} \\ -\dfrac{R_L}{3\gamma_u p}\dfrac{dp}{dt}\left[\left(\dfrac{r}{R_L}\right) - \left(\dfrac{r}{R_L}\right)^{-2}\right] & \text{Reactants} \end{cases} \tag{4.23}$$

Here, γ_u and γ_b are the specific heat ratios of reactants and products respectively.

The factor R_L/τ_p, where $\tau_p \equiv p(dp/dt)^{-1}$ appears in front of the expression for mean radial velocity in both reactants and products and scales the magnitude of term Π_2. The time scale τ_p is the reference time scale for pressure rise due to chemical reactions in the closed domain.

Figure 4.7 shows the term Π_2 and $\tilde{\Pi}_2 \equiv \Pi_2(\tau_p/\tau)(\sigma/R_L)$ as suggested by the analysis above. Similarity of $\tilde{\Pi}_2$ across different flames indicates that the mean transport term depends on the ratio of the flame brush thickness to the domain radius σ/R_L and the ratio of pressure rise time scale to the eddy turnover time τ_p/τ.

4.2.3 Flame stretch

Flame stretch acts as a source of surface density and contributes to increasing its peak. Recall that flame stretch consists of two terms so that $\Pi_4 = n\tau \langle K \rangle_w = n\tau \langle a \rangle_w + n\tau \langle S\nabla \cdot \mathbf{n} \rangle_w$. It must be noted that term Π_4 is proportional to the flame stretch $\langle K \rangle_w$ and not the *differential* flame stretch $\langle K' \rangle_w$ as with the turbulent flame brush thickness.

Figure 4.8(a) shows the time variation of the two stretch terms for various flames, normalized by flame time scale τ_L. The tangential strain rate term is positive while the curvature-propagation term is negative. Overall, the flame stretch at the peak location is positive and contributes to increasing the peak flame surface density. The absolute value of both components decreases in time.

It has been demonstrated that the tangential strain rate for infinitesimal material surface elements in homogeneous isotropic turbulence is governed by Kolmogorov time scale. Girimaji & Pope [43] found that the normalized tangential strain rate $a\tau_\eta \approx 0.165$, independent of Reynolds number in the range $\mathrm{Re}_\lambda = 38-90$, roughly the same range of Reynolds number in the present

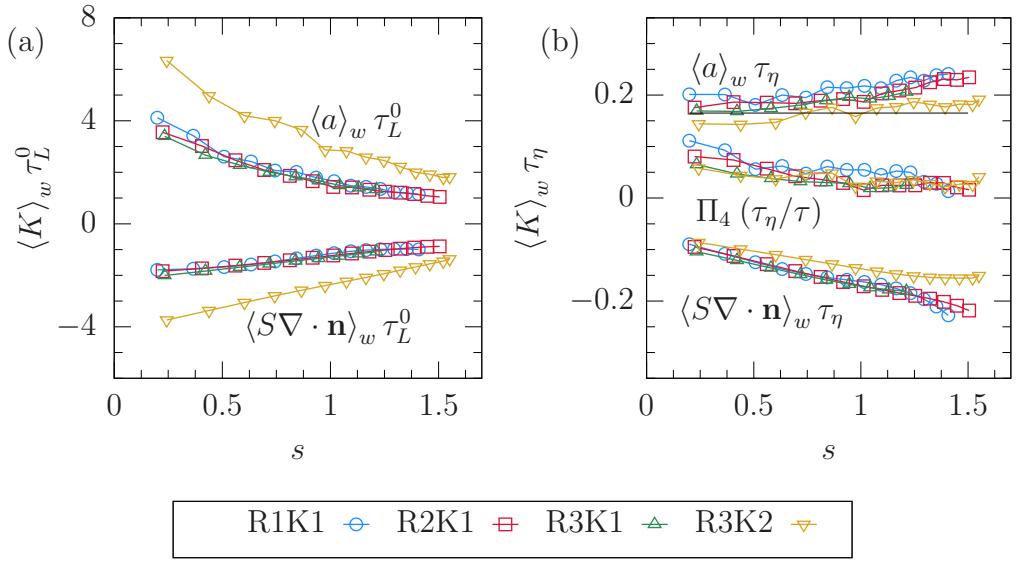

Figure 4.8: Flame stretch rate and components: (a) normalized by flame time τ_L and (b) by the instantaneous Kolmogorov time scale τ_η. Solid line in (b) marks $\langle a \rangle_w \tau_\eta = 0.165$, the constant value found for infinitesimal surface elements in isothermal turbulence [43].

database. The observation was attributed to the alignment of surface normal along the direction of the eigenvector corresponding to the most compressive (negative) eigenvalue if the velocity gradient tensor [43, 114], which leads to persistent straining of the surface.

Figure 4.8(b) shows the two terms compensated by the time varying Kolmogorov time scale τ_η, evaluated in the reactants. The turbulence statistics at the flame surface $C = c^*$ evolve similarly in time to that in the reactants to within a constant, thus the scaling arguments may be made based on turbulence reference scales in the reactants. Similar to the infinitesimal material surfaces, $\langle a \rangle_w \tau_\eta \approx 0.2$, independent of Reynolds number.

Once normalized by the instantaneous Kolmogorov time scale τ_η, the tangential strain rate term is approximately constant in time also to within 20%, as compared to a twofold change in $\langle a \rangle_w \tau_L^0$. The origin of the residual temporal dependence of $\langle a \rangle_w \tau_\eta$ is unclear at present and may be related to some large scale effects specific to the spherical flame configuration. It appears that this slow temporal evolution is slightly different across simulations and smaller for larger Reynolds numbers.

The normalized curvature-propagation term shows a larger temporal variation when normalized by τ_η and is analyzed using the same decomposition as in the context of turbulent flame brush thickness presented earlier (Eq. (3.29) in Sec. 3.2.3). The curvature-propagation stretch term is written as following:

$$\begin{aligned} n\tau \langle S\nabla \cdot \mathbf{n} \rangle_w &= -2n\tau \langle S\kappa \rangle_w \\ &= -2n\tau \langle S_g \rangle \langle \kappa \rangle - 2n\tau \,\mathrm{covar}\{S_g, \kappa \big| C = c^*\}, \end{aligned} \tag{4.24}$$

where covar denotes the conditional covariance of S_g and κ at the flame surface.

Since the curvature-propagation term is evaluated at the peak location, $\hat{\theta} \approx 0$. Since the mean flame curvature $\langle \kappa \rangle \approx 0$ at the center of the brush (see Fig. 3.9(a)), the curvature-propagation term is mainly controlled by the conditional covariance term.

Note that here the covariance term is evaluated only at the location of the peak surface density. Next, the covariance is re-written as a product of conditional covariances and a correlation coefficient,

$$-2n\tau \,\mathrm{covar}\{S_g, \kappa\} = -2n\tau \Phi_{s,\kappa} \sigma_s \sigma_\kappa, \tag{4.25}$$

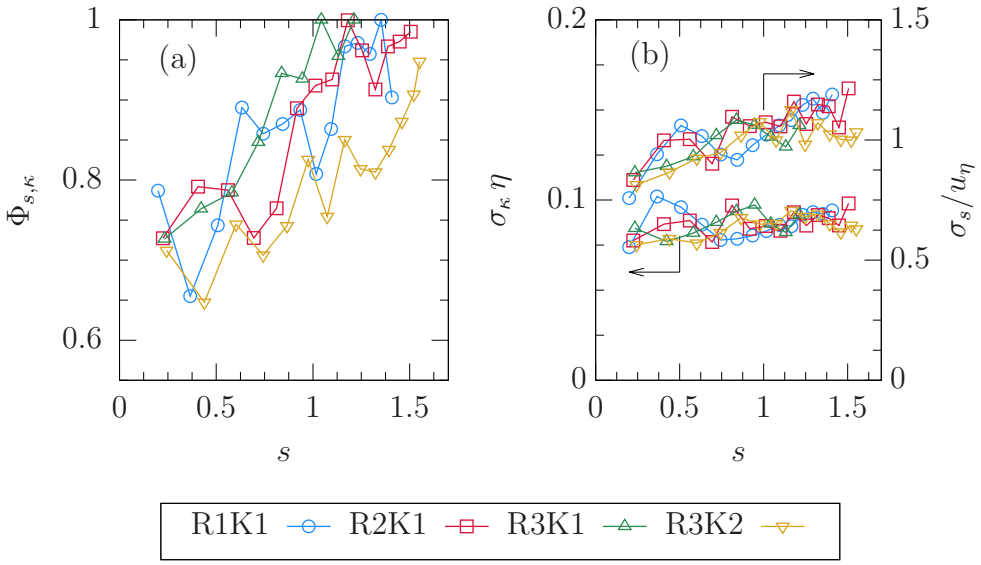

Figure 4.9: (a) Correlation coefficient $\Phi_{s,\kappa}$ and (b) conditional standard deviations σ_s and σ_κ of S_g and κ.

where $\Phi_{s,\kappa}$ is the conditional correlation coefficient and σ_s and σ_κ the conditional standard deviations of S_g and κ, respectively. All statistics are evaluated at the peak location and conditioned on the flame surface, $C = c^*$.

Figure 4.9 presents the time variation of the correlation coefficient and the conditional standard deviations of S_g and κ, normalized by appropriate Kolmogorov scales. It is evident that the normalized standard deviations are roughly constant in time and across different flames. Specifically, the collapse of these quantities across flames R3K1 and R3K2 is convincing where η and u_η differ by a factor of 1.5. On the other hand, $\Phi_{s,\kappa}$ changes by about 30% and explains most of the temporal variation in the curvature-propagation term, although it is nearly unity at all time.

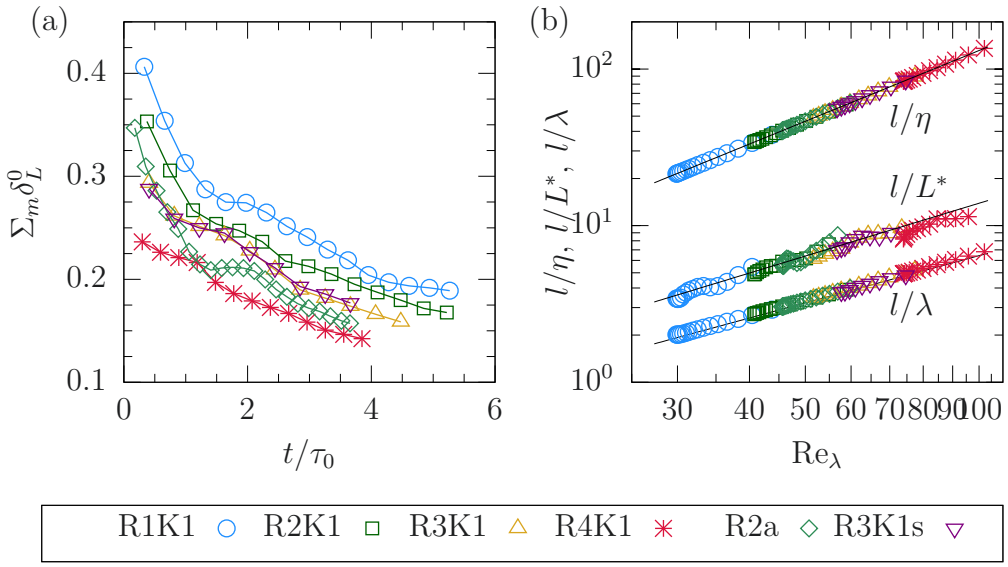

Figure 4.10: (a) Peak flame surface density $\Sigma_{\max}$ normalized by the thermal flame thickness δ_L^0. (b) The ratio of length scales l/η, l/λ and l/L^* along with power law fits of form $a\mathrm{Re}_\lambda^b$ (solid lines).

It is clear from the above analysis that the flame stretch at the peak location is governed by τ_η for the most part and that the product $\langle K \rangle_w \tau_\eta$ changes in time due to changes in the correlation coefficient $\Phi_{s,\kappa}$. The reasons behind this behavior are not clear at present and warrant further investigation over a broader range of dimensionless parameters.

As a consequence of the above analysis, the flame stretch may be modeled as $\Pi_4 \sim \Pi_4(s)(\tau/\tau_\eta) \sim \mathrm{Re}_\lambda$. In other words Π_4 is directly proportional to the instantaneous Reynolds number, but also possesses a residual temporal dependence not explained by changes in Reynolds number.

4.3 The wrinkling scale

Figure 4.10 (a) shows the temporal evolution of $\Sigma_{\max}$ normalized by the thermal thickness of the laminar premixed flame. It is apparent that $\Sigma_{\max}$ decreases it time several-fold for each spherical turbulent flame configuration. Since δ_L^0 is same for all flames and the variation in the flame thickness is minimal during the propagation of turbulent flames, the figure indicates conclusively that $\Sigma_{\max}$ does not scale with the thermal thickness of the laminar flame, a property of the premixed mixture. This behavior is consistent with experiments on turbulent spherical flames in decaying turbulence behind grids also [96, 40].

On the other hand, Fig. 4.10 (b) points to a hydrodynamic scaling of the wrinkling scale L^*. The subplot shows the wrinkling scale normalized by the integral length scale l and plotted against the Taylor Reynolds number. Data from all flame configurations and at several times are shown. It is apparent that over the range $30 \leq \mathrm{Re}_\lambda \leq 102$, the wrinkling scale L^* is about 3 to 12 times smaller than the integral length scale, consistent with previous experiments as discussed earlier. However, its variation across time and different flame configurations indicates its dependence on the Reynolds number.

The wrinkling scale falls between Taylor scale λ and Kolmogorov scale η, albeit closer to the former that to the latter. When scaled with l, the data suggests the following power law fit for the wrinkling scale:

$$l/L^* = 4\Sigma_{\max} l = 0.0756\,\mathrm{Re}_\lambda^{1.13}. \tag{4.26}$$

Note that only the data for $t/\tau_0 > 0.5$ have been used in this fit since it is necessary for turbulent motions to wrinkles the flame past an initial transient, during which a power law scaling for l/L^* is not warranted.

The power-law scaling for l/L^* from Eq. (4.26) shown in Fig. 4.10 (b) is rather convincing, especially since it holds across simulations with varying initial conditions and instantaneously as Re_λ and l vary in time during the decay of turbulence. Nevertheless, the postulated scaling relation must be validated over a broader range of Reynolds number.

The observation that $\eta < L^* < \lambda$ suggests that the peak surface density is governed by the small scale turbulent motion. The importance of small scales in controlling Σ_{max} has been postulated by Huh, Kwon & Lee [49], who analyzed the surface density transport equation for statistically planar flames and proposed that Σ_{max} scales with the inverse of the mean flame surface curvature. Since Zheng, You & Yang [126] recently demonstrated that the PDF of the flame surface curvature is independent of Reynolds number when normalized with the Kolmogov length, a case could be made that $\Sigma_{\mathrm{max}} \propto \eta^{-1}$ or $L^* \sim \eta$, independently of Reynolds number.

The present data do not support this hypothesis, although they do highlight the fact that L^* is smaller than λ and its evolution is most likely related to processes at the dissipative end of the inertial range of turbulence spectrum.

The Darrieus-Landau (DL) instability [29, 61] may provide an addi-

tional mechanism for flame surface wrinkling [39, 27], thereby influencing the surface density distribution, wrinkling scale and its proposed hydrodynamic scaling. The instability may be particularly important towards the end of simulations, as pressure and flame radius increase, while turbulence decays leading to small u'/S_L. The role of DL instability towards the observed scaling relation in Eq. (4.26) in the present dataset must be assessed.

The said assessment is made within the framework proposed by Yang *et. al.* [124], whereby the growth rates of DL instability (ω_{DL}) are compared against the rates of flame surface wrinkling due to turbulence (ω_T) in a range of wavenumbers where both effects are active. It is assumed that the range of scales over which the DL instability is important is $k_s \in [1/R, 1/\delta_L]$, while that of turbulent wrinkling is $k_s \in [1/l, 1/\eta]$. Since $R > l$ and $\eta < \delta_L$ at all times, the overlap region is $k_s \in [1/l, 1/\delta_L]$.

The ratio of growth rates $\omega_D L/\omega_T$ is proportional to characteristic velocities at the relevant scales, given by

$$\omega_T(k_s)/\omega_{DL}(k_s) \approx u'_{k_s}/S_L, \tag{4.27}$$

where $u'_{k_s} = (\epsilon/k_s)^{1/3}$ is the eddy velocity associated with the wavenumber k_s in the turbulence kinetic energy spectrum. Since $u'_{k_s}/S_L > u'_\eta/S_L > 1$ for all k_s in the overlap region, it is concluded that all turbulent flames considered here belong to the 'turbulent dominated regime', where the effects of DL instability can be safely neglected.

Chapter 5

Scaling of the area ratio

5.1 Evidence for Reynolds scaling

The mathematical framework presented in the earlier section demonstrated that the area ratio χ depends on two quantities that scale independently: the thickness of turbulent flame brush δ_T and the peak flame surface density therein, $\Sigma_{\max}$. The implications of their individual scaling laws on that of the area ratio χ are discussed next.

The expression for χ from Eq. (2.65) is rearranged as follows,

$$\chi = \Sigma_{\max}\delta_T\beta = (l/4L^*)(\delta_T/l)\beta. \tag{5.1}$$

Recall that β is a shape factor nearly constant and approximately equal to unity. Substituting the scaling laws $\delta_T \sim l$ and $l/L^* \sim \mathrm{Re}_\lambda^{1.13}$, the following expression is obtained

$$\chi(s,\alpha) = C_\chi \mathrm{Re}_\lambda^{1.13} f(s,\alpha), \tag{5.2}$$

where C_χ is a constant and the dependence of $\hat{\delta}_T$ on s and β on α is absorbed in the function $f(s)$. The area ratio χ and S_T/S_L increase in time directly due to increasing brush thickness δ_T/l and indirectly through $\mathrm{Re}_\lambda(t)$ in decaying turbulence.

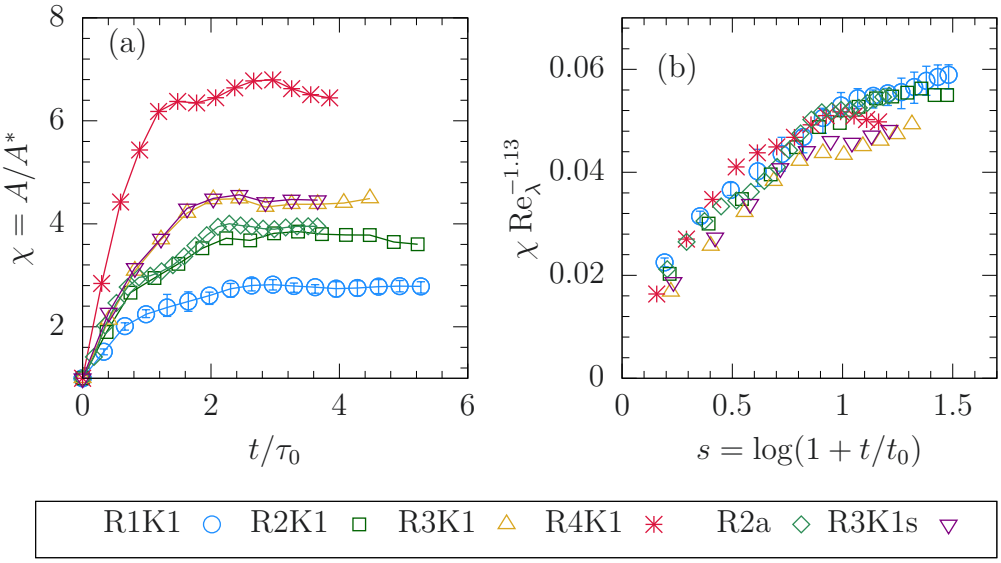

Figure 5.1: Temporal evolution of the area ratio: (a) χ vs t/τ_0 and (b) area ratio compensated with proposed Reynolds scaling, i.e. $\chi \mathrm{Re}_\lambda^{-1.13}$ against logarithmic time coordinate s. Error bars on the data for R1K1 show the range of values across four independent realizations.

The most important implication of Eq. (5.1) is that

$$\chi(t)\,\mathrm{Re}_\lambda^{1.13} \sim f(s,\alpha) \sim f(s), \tag{5.3}$$

so that if two turbulent spherical flames are compared at the same logarithmic time s, the area ratio increases as $\chi \sim \mathrm{Re}_\lambda^{1.13}$ or $\mathrm{Re}^{0.56}$, since $\mathrm{Re} = u'l/\nu \sim \mathrm{Re}_\lambda^2$. This observation is broadly consistent with previously reported Reynolds number dependence of burning rates in spherical turbulent flames [21, 51, 3].

Figure 5.1(a) shows the temporal variation of χ for various flame configurations. For $t/\tau_0 > 2$, the area ratio χ reaches a limit value which differs by a factor of 2-3 between R1K1 and R4K1. The same data are shown in a compensated form as $\chi \mathrm{Re}_\lambda^{1.13}$ versus s in subplot (b). Note that only data

for $t/\tau_0 > 0.5$, which corresponds to $s > 1.3$ are shown since the scaling of peak flame surface density requires that all scales of turbulent motion have had sufficient time to wrinkle the flame surface past an initial transient. This time is of the order of τ_0, the initial eddy turnover time scale, which is the time scale of the largest turbulent structure. During $t/\tau_0 < 0.5$ the proposed scaling of the wrinkling length scale is not valid.

The collapse in Fig. 5.1(b) is encouraging, albeit not perfect. Despite minor inconsistencies related to collapse of δ_T/l at later time, the data indicates that scale separation between the integral length scale l that governs the thickness of turbulent flame brush, and the wrinkling scale L^* which controls the peak flame surface density; plays an important role in controlling the area ratio and the dimensionless burning rate S_T/S_L.

In order to investigate this important implication, a set of three flames is considered. These include flames R2K1 and R2a, which share the same Reynolds number at all times $\mathrm{Re}_\lambda(t)$, but not the same u'/S_L. Along with these two flames, consider flame R1K1 also which shares the same temporal evolution of turbulence intensity u'/S_L but different Reynolds number.

From the evolution of χ for flames R1K1, R2K1 and R2a in Fig. 5.1(a), it is clear that when the Reynolds number is held constant and u'/S_L changes along with l/δ_L, the area ratio does not change (compare R2K1 and R2a). On the other hand, when u'/S_L is held constant and the Reynolds number changes along with l/δ_L, the area ratio is greater for the flame with higher Reynolds number (compare R1K1 and R2a).

These observations support the conclusion that, for a given premixed mixture, S_T/S_L is not a function of u'/S_L at constant Reynolds number for the flame configuration and regime of premixed turbulent combustion considered here. Rather, the data indicates that the area ratio and burning rates are controlled by the Reynolds number characterizing the state of reactants' turbulence.

A similar Reynolds number dependence was proposed by Chaudhuri *et. al.* [20] based on spectral analysis of the level-set equations. Since increasing Re_λ at fixed u'/S_L increases l/δ_L also, the observed trends and scaling of χ may not be conclusively attributed solely to Re_λ independently of l/δ_L and a broader set of experiments are required.

Chapter 6

Reactive surfaces in shear driven turbulence

The analysis presented in the previous chapters on the evolution of flame surface area, thickness of the turbulent flame brush and the wrinkling scale considered a canonical configuration of turbulent spherical flames in homogeneous isotropic turbulence. Turbulent flows in devices for practical engineering applications are more complex and generate turbulence through mean shear.

The discussion in this chapter seeks to advance the framework and analysis presented previously to a practically relevant flow configuration. In particular, the applicability of Reynolds scaling of growth rate of the surface area of a reactive front is examined.

To this end, the development of reactive surfaces in a swirling von Kármán flow device is considered. A schematic diagram of the device is shown in Figure 6.1. More details on the geometry are provided in Appendix C. The configuration consists of a set of two counter-rotating impellers (shown in red and blue colors), enclosed in an outer cylindrical chamber. Fluid flow inside the device is driven by the impellers, which rotate at a fixed angular speed Ω. The central region features shear-generated turbulence of high intensity. The

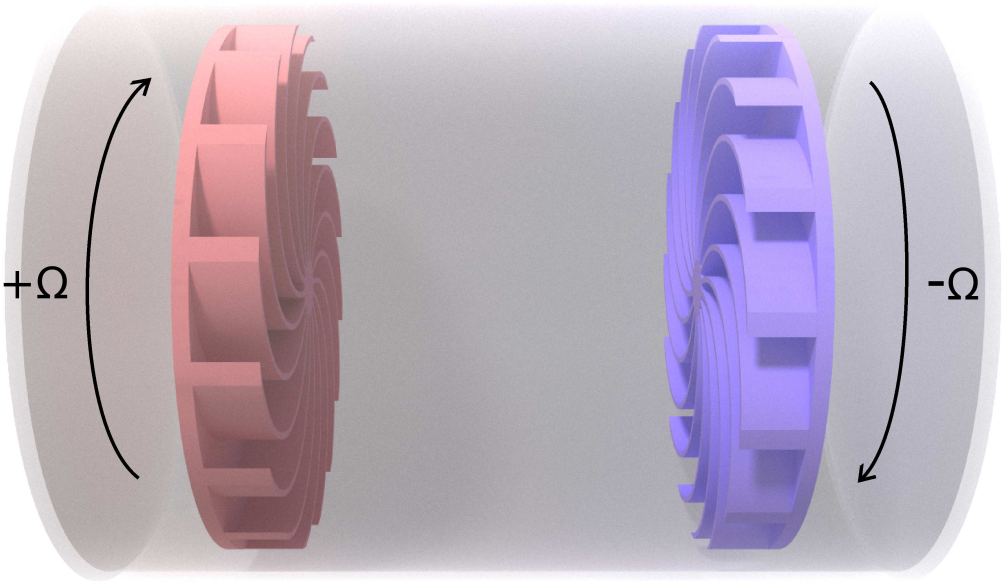

Figure 6.1: A schematic representation of the von Kármán device. The impellers, shown in red and blue colors, rotate in opposite directions as indicated by the arrows. Fluid flow is confined within the cylindrical enclosure shown in grey color.

configuration is reproduced from the experimental apparatus 'TM 60' analyzed by Ravelet *et. al.* [95].

The interaction of moving impellers with surrounding fluid flow is modeled with the immersed boundary method of Uhlmann [116]. In this approach the no-slip velocity boundary condition at the solid-fluid interface is enforced indirectly through a body force field $\mathbf{F}_{\mathrm{IB}}(\mathbf{x}, t)$, which is evaluated at each time t so that the relative fluid velocity at the interface equals zero. With this approach, a homogeneous Cartesian mesh with uniform grid spacing may be used instead of a body-fitted mesh to the moving interface which requires frequent

re-meshing. More details on the implementation of the immersed boundary method can be found in the work by Kasbaoui, Kulkarni & Bisetti [53].

6.1 Mathematical models for reactive front

Development of a reactive-diffusive interface in a fully developed von Kármán swirling flow is analyzed by solving the reactive scalar equation

$$\rho\frac{\partial C}{\partial t} + \rho\mathbf{u}\cdot\nabla\mathbf{C} = \rho\mathcal{D}_C\nabla^2 C + \dot{\omega}_c, \tag{6.1}$$

where C is the reaction progress variable, $\mathcal{D}_C$ the diffusion coefficient and $\dot{\omega}_C = \dot{\omega}_C(C)$ the reaction rate, which is modeled as a function of progress variable C only. The use of detailed chemistry with multiple species and elementary reactions as with spherical turbulent flames is computationally expensive as discussed later in this section.

The density ρ and the molecular diffusion coefficient $\mathcal{D}_C$ are assumed to be constant across the reactive front in order to simplify the analysis. As a result, thermodynamic pressure p remains constant in time also. Since the density ratio across the reactive front is taken to be unity, the fronts are referred to as *reactive-diffusive fronts* and not *flames*, as premixed flames have a non-unity density ratio due to heat release from chemical reactions. Nevertheless, the role of the density ratio in turbulent burning rates and surface wrinkling is minor [66] and the examination of the evolution of reactive-diffusive surfaces is still useful.

All governing equations are considered in a dimensionless form with

reference scales R_{cyl}, the radius of the cylindrical enclosure; Ω, the rotation rate of impellers and the density ρ. The set of governing equations for conservation of mass, momentum and the progress variable read as follows in the dimensionless form:

$$\nabla \cdot \mathbf{u} = 0, \tag{6.2}$$

$$\frac{\partial \mathbf{u}}{\partial t} + \mathbf{u} \cdot \nabla \mathbf{u} = -\nabla \pi + \mathrm{Re}_{\Omega}^{-1} \nabla^2 \mathbf{u} + \mathbf{F}_{\text{IB}}, \tag{6.3}$$

$$\frac{\partial C}{\partial t} + \mathbf{u} \cdot \nabla C = \mathrm{Re}_{\Omega}^{-1} \mathrm{Sc}^{-1} \nabla^2 C + \mathrm{Da}^{-1} \widetilde{\dot{\omega}}_C, \tag{6.4}$$

where all quantities and differentiation operators in the equations above are in the dimensionless form.

In the equations above, $\mathrm{Re}_{\Omega} \equiv \rho R_{\text{cyl}}^2 \Omega / \mu$ denotes the Reynolds number based on the reference device scales, $\mathrm{Sc} \equiv \mu / \mathcal{D}_C$ the Schmidt number and $\mathrm{Da} = 6\mathcal{I}_C / \Omega$ the Damköhler number. Here, $\mathcal{I}_C$ denotes the integral of the reaction rate $\dot{\omega}_C$ in the progress variable space,

$$\mathcal{I}_C \equiv \int_0^1 \dot{\omega}_C(c)\, dc, \tag{6.5}$$

so that the integral of $\widetilde{\dot{\omega}}_C \equiv \dot{\omega}_C / 6\,\mathcal{I}_C = 1/6$ and matches that of the classic Fisher-KPP expression $\widetilde{\dot{\omega}}_C = C(1-C)$. Thus, in Eq. (6.4), the magnitude of the reaction term is controlled by the Damköhler number.

The normalized reaction rate function $\widetilde{\dot{\omega}}_C$ is modeled with the Zeldovich reaction rate closure [125]

$$\widetilde{\dot{\omega}}_C = \begin{cases} 0 & C \le c^* \\ \dfrac{1}{8(1-c_m)} \left[1 - \dfrac{(C-c_m)^2}{(1-c_m)^2} \right] & C > c^*. \end{cases} \tag{6.6}$$

In the equation above, $c_m = 2c^* - 1$ is the location of the peak reaction rate and c^* is the cutoff in the progress variable space. The reaction rate is zero for all values below the threshold c^* which mimics the effects of activation energy on chemical reaction rates. With this model for the reaction rate, the progress variable equation follows the form of Fisher-KPP equation [38, 59] for a reactive-diffusive propagating front.

The single-equation, progress variable model is preferred to finite rate chemistry calculations since the von Kármán flow device does not offer the same statistical symmetries as the spherical turbulent flames. As a result, averaging over multiple realizations is required and the use of single equation progress variable model makes large scale simulations computationally affordable.

The suitability of the single-equation progress variable model for the thin reaction zone regime was assessed by conducting tests of spherical turbulent flame R1K1 and compared with the corresponding DNS data obtained previously using the detailed finite rate chemistry. Negligible differences in all statistics pertaining to the evolution of the flame surface were observed while resulting in a 30x speed up in computational speed. In other words, the use of the single variable progress variable model allows for 30 realizations of the flow with the same computational cost as that with a single finite rate chemistry calculation.

Code	Re_Ω	N_r	Π_V	Π_L	Runs
S1	4 000	640	11.50	42.58	30
S2	8 000	896	16.25	60.41	30
S3	16 000	1280	23.00	84.00	10

Table 6.1: Design parameters for increasing Reynolds number at fixed values of $\mathrm{Sc} = 0.25$ and $\mathrm{Da} = 10$.

6.2 Description of database

The investigation of the role of the Reynolds number on the development of reactive surfaces consists of a set of three direct numerical simulations at increasing Reynolds number Re_Ω from $4,000$ to $16,000$, doubling between consecutive simulations. Relevant parameters are listed in Tab. 6.1. The Damköhler number $\mathrm{Da} = 10$ and the Schmidt number $\mathrm{Sc} = 0.25$ are kept fixed and their values are chosen so as to match the resolution requirements for the reactive front and turbulence.

Numerical simulations are initialized from a quiescent initial condition and the flow in the device is allowed to develop as a result of the action of the moving impellers alone. A statistically stationary turbulent flow is observed to develop after about two full revolutions, after which a laminar kernel of radius $0.15R$ is initialized at the center of the domain. Statistics related to the development of the reactive-diffusive surface are gathered by conducting multiple realizations initialized at times separated by at least $1/16^{\mathrm{th}}$ revolution, the time period after which the flow is statistically periodic. For configurations S1 and S2, the ensemble contains 30 independent runs, while for S3 only 10

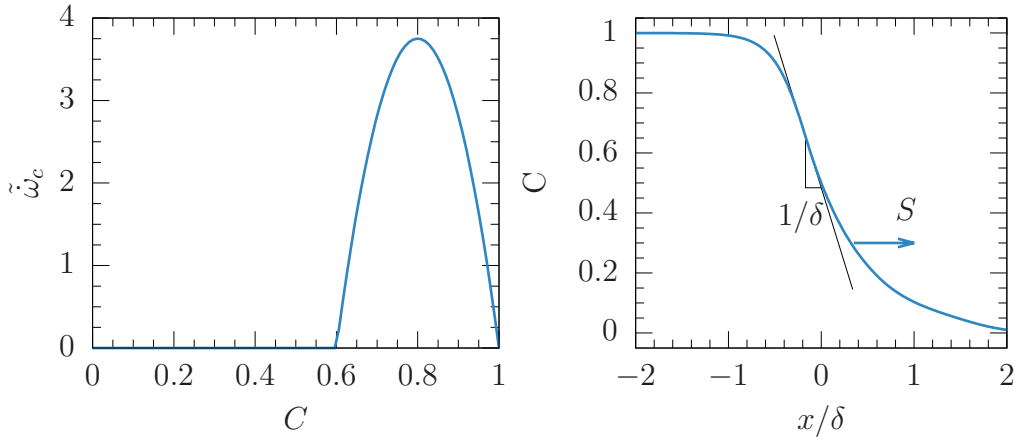

Figure 6.2: Reactive-diffusive front with the single-equation progress variable model with constant density and diffusivity. (a) The normalized Zeldovich reaction rate term $\dot{\omega}_C$ against progress variable C and (b) resulting flame front, travelling from left to right. Progress variable cutoff of $c^* = 0.6$ for $\dot{\omega}_C$ is used for calculation.

runs were afforded at present due to relatively higher computational cost.

A one-dimensional laminar solution to the reactive-diffusive front governed by Eq. (6.4) is shown in Fig. 6.2. The front propagates from left to right and introduces intrinsic velocity and length scales, denoted by S and δ, respectively. Here, the laminar thickness $\delta = \max\{|dC/dx|\}$ is defined using the maximum gradient method.

The ratio of velocity scales $\Pi_V = R\Omega/S$ and length scales $\Pi_L = R/\delta$ serve as additional dimensionless parameters. In order to keep Da and Sc fixed while varying Re_Ω, Π_V and Π_L must vary as well, since

$$\Pi_L^2 = \mathrm{Re}_\Omega \mathrm{ScDa}/(c_1 c_2) \tag{6.7}$$

$$\Pi_V^2 = \mathrm{Re}_\Omega \mathrm{ScDa}^{-1}\,(c_2/c_1), \tag{6.8}$$

where $c_1 = S\delta/\mathcal{D}_C$ and $c_2 = \delta\mathcal{I}_C/S$ depend on the c_m, density ratio across the front and the model for changes in viscosity across the front. Note that since Π_L and Π_V change across simulations S1 through S3 they may influence the evolution of the surface area of the reactive fronts also.

A homogeneous Cartesian grid is considered with a uniform grid spacing. The number of grid points in the directions perpendicular to the axis of rotation are denoted by N_r in Tab. 6.1. The spatial resolution is determined by estimating the Kolmogorov scale η at the center of the device using isothermal runs as discussed below in Sec. 6.3.3. The reactive front is resolved with $\delta_L/\Delta > 7$, a higher resolution than that of reactive fronts considered earlier in spherical turbulent flames.

6.3 Characterization of the velocity field

The fluid flow between two impellers is driven by the rotation of the blades and turbulence in the central region is generated through mean shear. Ravelet *et. al.* [95] investigated the flow in the device over a wide range of Reynolds numbers ranging from $\mathrm{Re}_\Omega = 90$ to $1,200,000$. They observed that at low Reynolds number, the flow consists of two toroidal regions resulting in a symmetrical flow about the mid-height plane. The symmetry is broken due

A part of the content presented in Sec. 6.3 was originally published in the following article:

Kasbaoui, M. H., Kulkarni, T., Bisetti, F. (2021). Direct Numerical Simulations of swirling von Kármán flow using a semi-implicit moving immersed boundary condition. *Comput. Fluids*. Available online at `https://doi.org/10.1016/j.compfluid.2021.105132`.

to an onset of Kelvin-Helmhotz instability at $\mathrm{Re}_\Omega = 360$. As the Reynolds number is increased, several successive instabilities appear, resulting in a transitional flow at $\mathrm{Re}_\Omega = 2000$, eventually leading to a fully developed turbulent flow at $\mathrm{Re}_\Omega = 4000$. These flow features were replicated as a validation of the immersed boundary method implementation in a previous work [53].

Of particular interest to this work is the evolution of large surfaces in the shear-driven flow in the turbulent regime. For this reason, the range of Reynolds numbers from $\mathrm{Re}_\Omega = 4,000$ to $16,000$ is considered, which feature fully developed turbulent flow.

Figure 6.3 compares the velocity component in the direction normal to the planar cut for three cases S1 through S3 at the end of three revolutions, i.e. $\Omega t/2\pi = 3.0$. Consistent with the decrease in viscosity as the Reynolds number increases, finer structures appear in the velocity field.

Since the density is constant, the velocity field evolves independently of the progress variable C, although the evolution of the reactive front is affected by the velocity field through the convection term in Eq. (6.4). Thus, a preliminary characterization of the velocity field is in order. In particular, the spatial variation of velocity components and isotropy of the Reynolds shear stress tensor are investigated next before analyzing the evolution of surfaces in the device at increasing Reynolds number.

Figure 6.3: Snapshots of configurations S1 through S3 at normalized time $ft = \Omega t/2\pi = 3.00$ during the isothermal precursor run. As Reynolds number Re_Ω increases from 4,000 (S1) to 16,000 (S3), finer structures appear whereas the mean velocity field remains largely similar.

6.3.1 Mean flow field and homogeneity

In the database of the three von Kármán flow configurations, Reynolds number is changed by changing the kinematic viscosity ν, while the device radius R_{cyl} and rotation rate Ω is kept fixed. As shown in Fig. 6.3, flow-fields for a higher Reynolds number features smaller scales of coherent turbulent motion as compared to that for a lower Reynolds number. However, the Reynolds-averaged mean flow field, which retains only the large scale flow features of the size comparable to the device length scale, is expected to be independent of the Reynolds number. This postulate is validated by averaging the velocity components according to the averaging procedure described below.

Since the configuration involves 16 blades on each impeller, the flow internal to the cylindrical domain confined by the immersed boundaries is statistically periodic with a period $\tau_b = 2\pi/16$. As a result, each grid point in the internal flow has 15 corresponding points where statistics of velocity field are identical, which are at equal angle ahead of the 16 blades. Upon reaching statistical stationarity (about 2 revolutions), temporal averaging is conducted from the perspective of an observer moving with the rotating blades, i.e. in 'blade-view'. Samples at different time are rotated by the angle of rotation of the blade before grouping together.

Statistics gathered using the averaging procedure outlined above depend on radial coordinate r, axial coordinate z and angular position ahead of the blades $\Theta \in (0, 2\pi/16)$. It is observed, although not shown here, that the the statistics depend strongly on the sample angle with respect to the blades

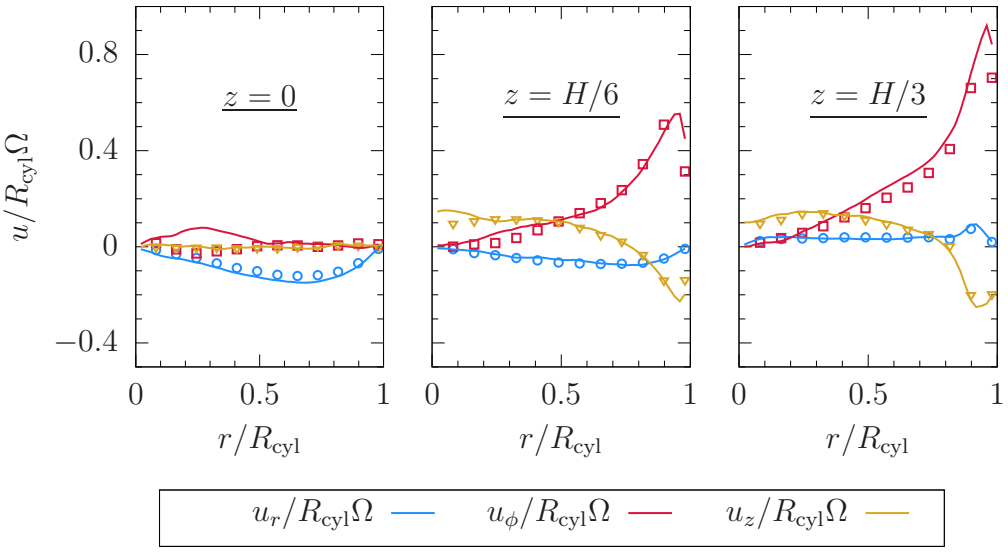

Figure 6.4: Components of Reynolds averaged velocity vector at three locations between the central plane ($z = 0$) and the base of the impellers ($z = H/2$). Data is compared across configurations S1 (symbols) and S2 (lines).

in the region near the impellers only. Moving towards the central region, the dependence on the angular direction weakens and the flow in the central region possesses cylindrical symmetry.

The three components of the mean velocity field extracted along radial lines for the azimuthal angle $\Theta = 0$ and at different height z/H are shown in Fig. 6.4. Here $H = 1.8R_{\rm cyl}$ refers to the distance between two impellers. The magnitude of all components of the mean velocity field are small at the mid-height plane $z = 0$. In the planes closer to the impellers, the radial and axial components u_r and u_z remain small but the angular component u_ϕ reaches a value close to the tip velocity of the blades. Comparison between data for configurations S1 and S2 suggests that the mean velocity field is fairly

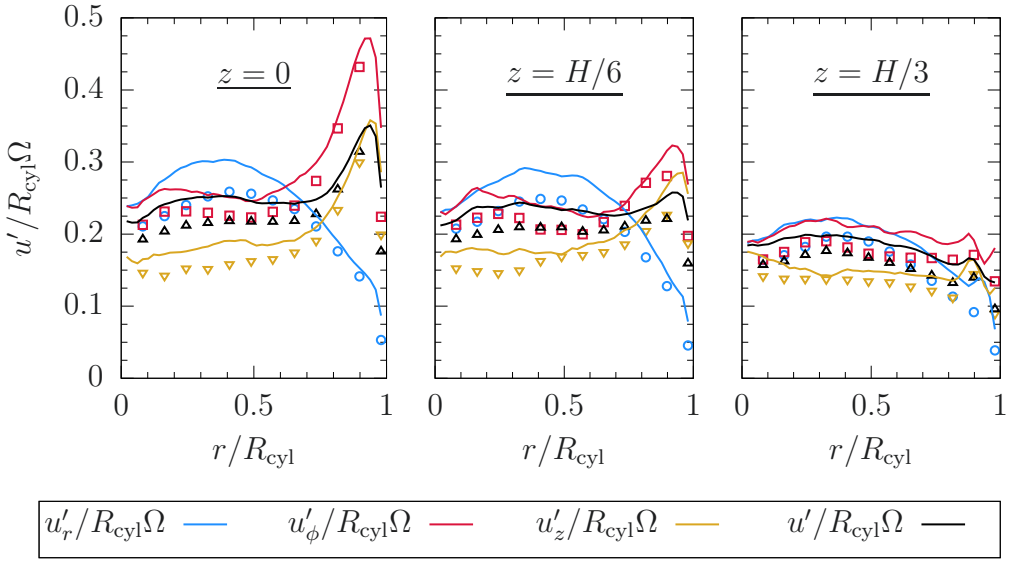

Figure 6.5: RMS fluctuations of the cylindrical components of velocity vector at three locations between the central plane ($z = 0$) and the base of the impellers ($z = H/2$). Data is compared across configurations S1 (symbols) and S2 (lines).

insensitive to the Reynolds number.

Figure 6.5 presents the RMS fluctuations of the three components at the three planes. The RMS fluctuations of all velocity components is larger than the mean near the central region and decrease with decreasing distance to the impellers. Unlike the mean velocity field, the RMS velocity fluctuations depend on the Reynolds number, although the dependence is minor. Fluctuations in the radial and azimuthal components are approximately equal to each other and larger than the axial component for $r/R_{\mathrm{cyl}} \leq 0.5$. The implications of this observation on local isotropy of Reynolds stress tensor are discussed later in Sec. 6.3.2.

Based on the preliminary characterization of the statistics of the mean velocity field, it may be concluded that the flow in the central region, i.e. $r/R_{\text{cyl}} \leq 0.5$ and $|z|/H \leq 0.2$ experiences a low enough mean velocity that the evolution of surfaces initiated in this region is primarily due to turbulent fluctuations.

6.3.2 Isotropy of the Reynolds stress tensor

The isotropy of the Reynolds stress tensor is investigated using the anisotropic stress tensor $b_{ij} = \overline{u_i' u_j'}/\overline{u_k' u_k'} - \delta_{ij}/3$ and its invariants. Here, δ_{ij} denotes the Kronecker delta function. The fluctuation of the j^{th} component of the velocity vector over its Reynolds mean is denoted with u_j'.

In constant density turbulent flows, the first invariant $\text{I}_b = b_{ii} = 0$. The second and third invariants are given by

$$\text{II}_b = b_{ij} b_{ji}/2 \tag{6.9}$$

$$\text{III}_b = b_{ij} b_{jk} b_{ki}/3. \tag{6.10}$$

Lumley [72] proposed six limits that the anisotropy tensor could take based on the values of the invariants, which also serve as the boundaries to a region realizable in turbulent flows.

Following the approach by Pope [93], the anisotropy invariant map is considered for the transformed invariants $\widetilde{\text{II}}_b = (-\text{II}_b/3)^{1/2}$ and $\widetilde{\text{III}}_b = (\text{III}_b/2)^{1/3}$. Figure 6.6 presents the pairs $(\widetilde{\text{II}}_b, \widetilde{\text{III}}_b)$ on the anisotropy invariant map, alternatively known as 'Lumley triangle' [102].

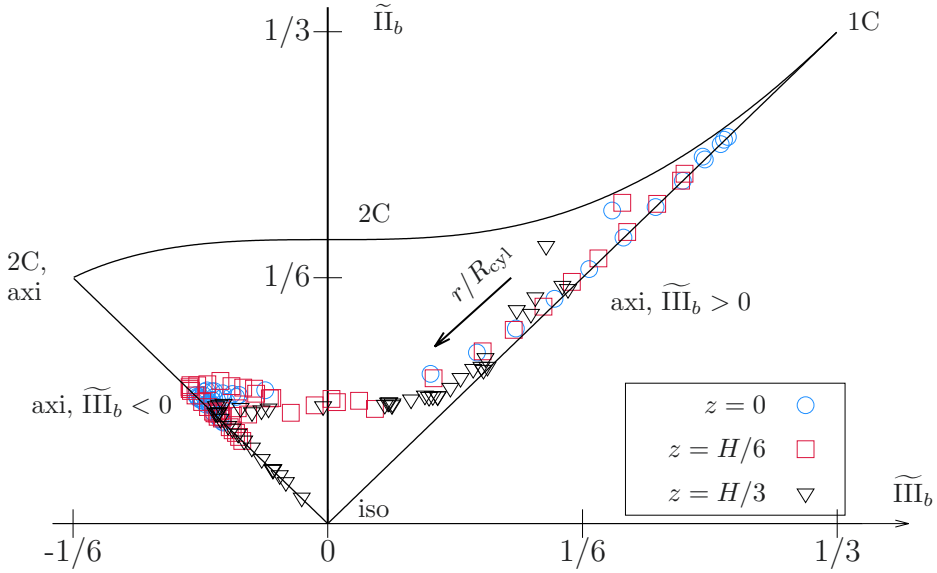

Figure 6.6: Lumley triangle on the plane of invariants $\zeta - \eta$ of the Reynolds stress anisotropy tensor for $\mathrm{Re}_\Omega = 8,000$ in three planes normal to the rotation axis. Arrow indicates the direction of increasing r/R_{cyl} from 0 to 1.

Briefly, an isotropic state corresponds to the point $\widetilde{\mathrm{II}}_b = \widetilde{\mathrm{III}}_b = 0$, where the anisotropy tensor is identically zero. The shape of Reynolds stress tensor for isotropic turbulence corresponds to a sphere. The two limits of interest here are the two axisymmetric regions marked as 'axi, $\widetilde{\mathrm{III}}_b < 0$' and 'axi, $\widetilde{\mathrm{III}}_b > 0$'. The former limit corresponds to two equal, positive eigenvalues and a third, negative eigenvalue greater than both. The shape of Reynolds stress tensor in this case is an ellipsoid or an 'prolate spheroid' [93]. Similarly, the latter limit of two negative eigenvalues and a third positive eigenvalue corresponds to an 'oblate spheroid' shape. Other limits of the anisotropy invariant map are not of relevance here and not discussed further. Interested reader may refer to the Refs. [72, 93, 102] for more information.

The data for $\mathrm{Re}_\Omega = 8000$ at three planes, $z = 0$, $H/6$ and $H/3$ is presented in Fig. 6.6 with the help of various symbols. Arrow marks the direction of increasing distance from the axis, $r/R_{\mathrm{cyl}} = 0$.

In the central region of the device, the Reynolds stress tensor is axisymmetric with a large positive eigenvalue. Moving outwards in the radial direction, the flow transitions between two axisymmetric shapes where the larger eigenvalue changes from positive to negative. The near-wall region displays characteristics of a single component turbulence (labeled '1C' at the top right corner), consistent with the presence of boundary layers near the walls of the enclosure. It is clear that turbulence at the center of the device is not isotropic and exhibits anisotropy similar to that found in turbulent boundary layers.

6.3.3 Reference turbulence scales

The characterization of turbulence-flame interaction in the swirling von Kármán flow device requires an estimation of reference scales of turbulent motion at the center of the device. An estimate of the smallest length scale of turbulence, i.e. the Kolmogorov scale will also help determine resolution requirement for the direct numerical simulations.

The Kolmogorov scale $\eta = (\nu^3/\epsilon)^{1/4}$, integral scale $l = u'^3/\epsilon$ and corresponding time scales provide a meaningful description of turbulent flow only for a homogeneous isotropic turbulence. However, as discussed in the earlier section, turbulence in the central region is neither homogeneous nor isotropic.

Code	Re_Ω	N_r	u'/S	l/δ_L	τ/τ_L	η/Δ	δ_L/Δ
S1	4 000	640	2.88	11.36	5.92	1.50	7.42
S2	8 000	896	4.06	16.11	5.95	1.25	7.35
S3	16 000	1280	5.75	22.40	5.84	1.06	7.57

Table 6.2: Dimensionless groups describing reactive von Kármán flow simulations based on estimates of turbulence scales at the center of the domain.

Yet, using these relations provides an order of magnitude estimate of large and small scales of turbulent coherent motion and may be used to determine the resolution requirements.

Keeping in mind this important distinction, estimates for Kolmogorov length scale, integral length scale and eddy turnover time are obtained as follows. The normalized RMS velocity fluctuation equals $u'/R\Omega \approx 0.2$, over a wide central region spanning $|z|/H < 0.3$ and $r/R_{\mathrm{cyl}} < 0.8$ (see Fig. 6.5). Similarly, it was observed that the mean rate of dissipation of the turbulent kinetic energy, $\epsilon/(R^2\Omega^3) \approx 0.03$.

Based on the observed values of $u'/R\Omega$ and $\epsilon/R^2\Omega^3$, all other scales are estimated using relations for homogeneous isotropic turbulence. Tab. 6.2 lists the pertinent dimensionless groups based on the estimates. Turbulence scales u', l, τ and η are estimated using isotropic turbulence relationships and may be regarded as order of magnitude estimates only.

Spatial resolution was determined so as to ensure $\eta/\Delta > 0.5$ and $\delta_L/\Delta > 7$. Adequacy of the chosen resolution of the velocity and scalar fields was confirmed by conducting a grid dependence study on configuration S1.

6.4 Evolution of reactive-diffusive surfaces

The reactive runs for von Kármán flow are initiated by introducing a laminar spherical kernel of radius $0.15R_{\text{cyl}}$, so that the ratio of integral scale to the kernel radius is of order unity and all scales of turbulent motion participate in wrinkling the surface. Similar to the analysis of the turbulent spherical flames, the reactive-diffusive front in a simulation is tracked with isosurface $C = c_m$, which corresponds to the location of peak reaction rate $\dot{\omega}_C$.

Figure 6.7 shows the isosurfaces when the embedded volume is four times that of the initial kernel. Similar to the behavior seen in Fig. 2.3 for spherical turbulent flames at different Reynolds number, the isosurface for configuration S3 features wrinkles of smaller size and has a higher surface area.

The temporal evolution of the surface area of the reactive-diffusive front and its dependence on Reynolds number is of particular interest. Figure 6.8(a) shows the surface area against the dimensionless time $ft = \Omega t/2\pi$. The surface area is normalized by that at the onset A_{ref}, which is equal for all three configurations, S1 through S3.

In general, configurations with a higher Reynolds number exhibits a faster growth of the surface area of the reactive-diffusive front as compared to that with a lower Reynolds number. The higher surface area is achieved through wrinkling at progressively finer scales, since the large structures of turbulent motion are a fixed proportion of the device radius.

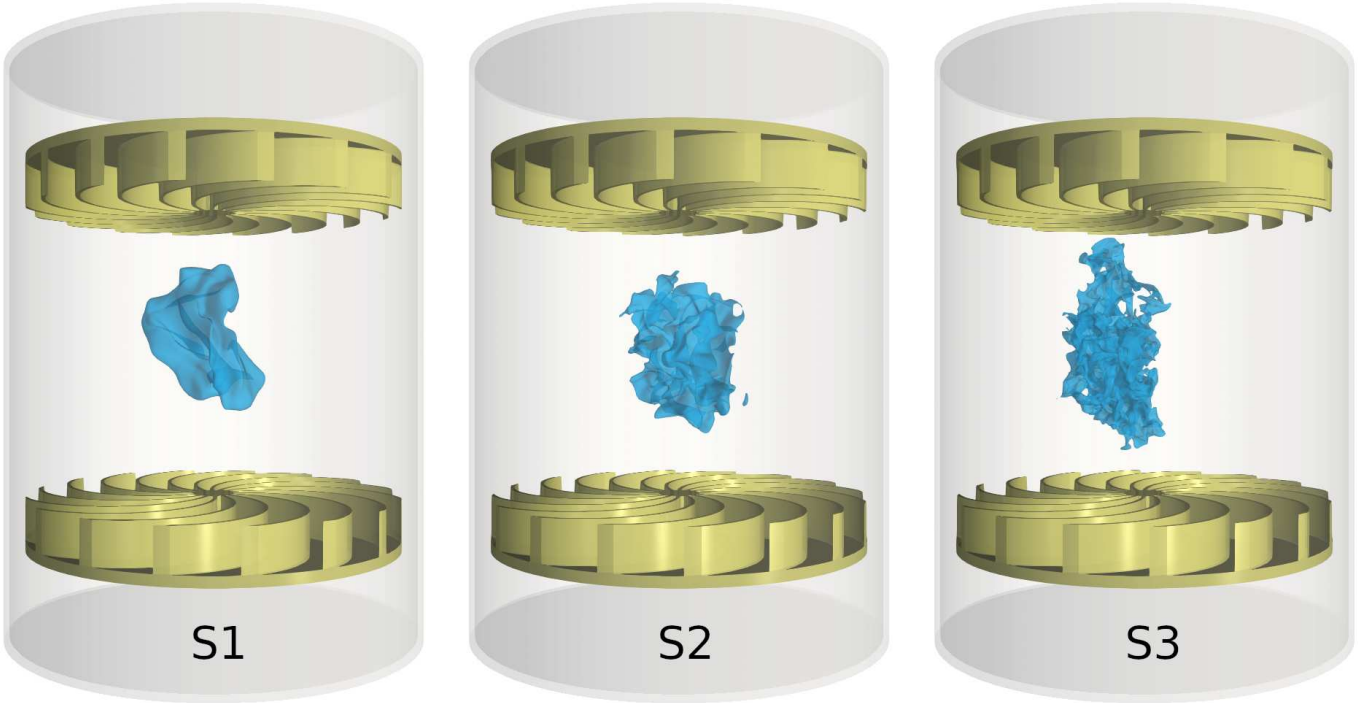

Figure 6.7: Snapshots of the evolving reactive-diffusive fronts for configurations S1 through S3. Snapshots are shown at the instance when volume enclosed by $C = c_m$ isosurface is four times that of the volume at the onset.

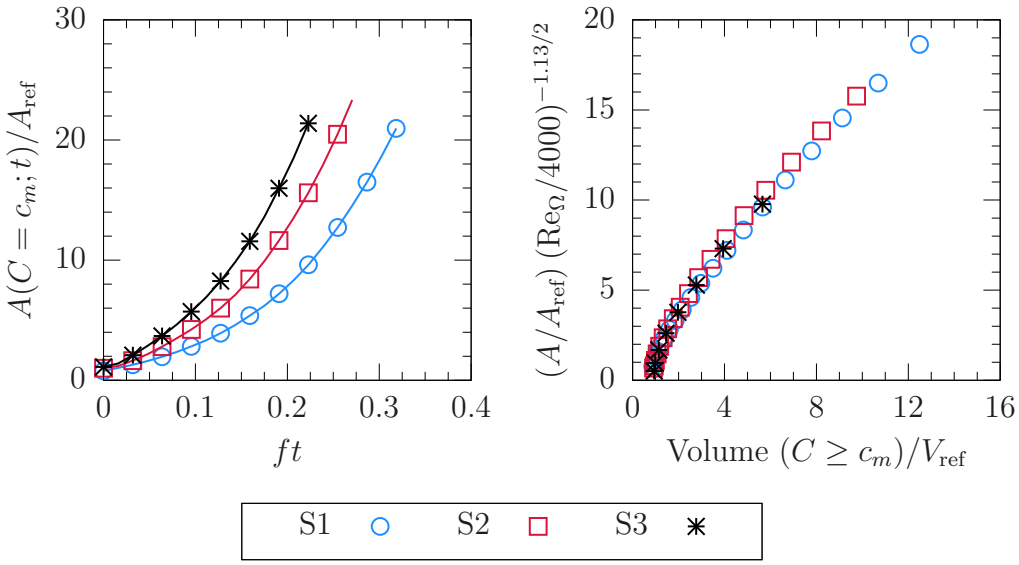

Figure 6.8: Surface area of iso-surface $C = c_m = 0.8$ against volume of region with $C \geq c_m$. Quantities on both axes are normalized by their respective values at the onset for a kernel of radius $0.15R_{\mathrm{cyl}}$.

However, to demonstrate the dependence of surface area and its growth rate, the configurations should not be compared against each other at the same time for the following reasons. First, the propagation speed S of the front decreases across configuration S1 to S3 by design, so that the flame surface wrinkling and propagation occurs on different time scales. Moreover, turbulent flow inside the device is neither homogeneous nor isotropic, thus the fronts experience different mean and rms velocity components in time. Instead, the comparison is made when different configurations have the same volume of the region $C > c_m$. This ensures that the linear extent of the three-dimensional front is approximately the same.

Figure 6.8(b) shows the the surface area of the iso-surface $C = c_m$ against the volume bounded by the surface. Upon normalizing with the postulated Reynolds scaling relation $A \sim \mathrm{Re}_\Omega^{1.13/2} \sim \mathrm{Re}_\lambda^{1.13}$, the a reasonable collapse across the three configurations is observed. Recall that the large scale Reynolds number and Taylor Reynolds numbers are related as $\mathrm{Re}_\lambda \sim \mathrm{Re}_\Omega^{1/2}$.

6.4.1 Deliberation on the observed Reynolds scaling

The Reynolds dependence of the front's surface area was originally postulated and examined for spherical turbulent flames in decaying isotropic turbulence with no externally imposed mean velocity field. Moreover, the analysis was conducted a non-unity density ratio. Yet, the evolution of the surface area in the turbulent von Kármán configurations is broadly consistent with the proposed Reynolds scaling, despite the differences.

The proposed Reynolds scaling of the surface area arises from scaling of turbulent flame brush thickness and the peak flame surface density function. As such, the scaling of turbulent flame brush thickness with integral scale l and that of the wrinkling length scale L^* as $L^* \sim l\mathrm{Re}_\lambda^{-1.13}$ need to be validated for turbulent von Kármán flow configurations. Since the turbulent flow in the von Kármán flow configurations feature two non-ergodic spatial directions, the investigation of both these quantities requires two-dimensional counterparts to their evolution equations, Eq. (3.12) and Eq. (4.19). The analysis of these equations are out of scope of this dissertation and the author's thoughts on their derivation are included in Sec. 7.4 on recommendations for future work.

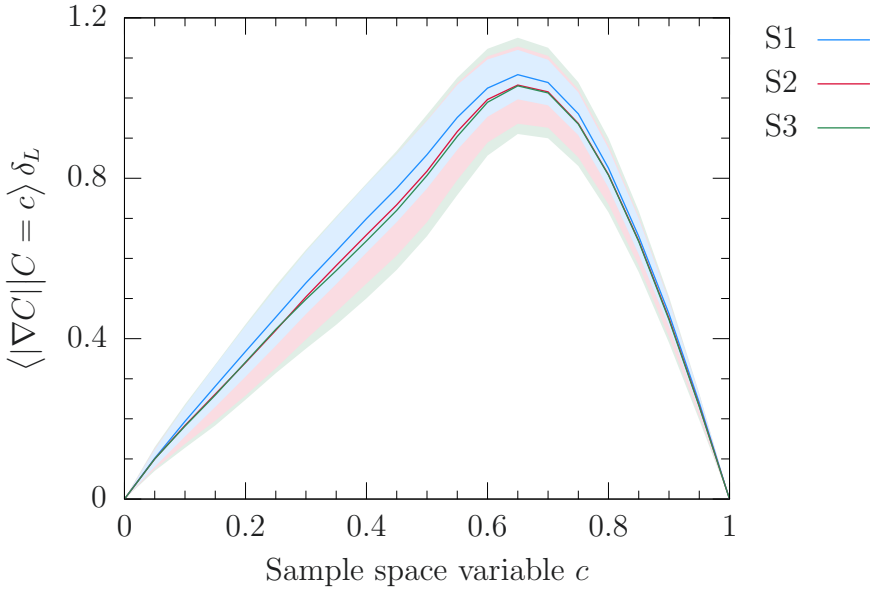

Figure 6.9: Conditional mean of the progress variable gradient magnitude. Shaded regions mark one standard deviation around the mean.

A qualitative discussion on scaling of the two quantities is included next.

Figure 6.9 shows the conditional mean and standard deviation of the magnitude of the progress variable gradient, conditioned on various sample space values. As with turbulent spherical flames, the conditional mean of the gradient remains close to its laminar value with a small variance. As a result, the surface density function is controlled by the PDF of progress variable and the wrinkling scale is governed by hydrodynamic processes. Since the mean and RMS fluctuations of velocity components show no Reynolds dependence while the Kolmogorov time scale $\tau_\eta \sim \mathrm{Re}_\lambda^{-1} \sim \mathrm{Re}_\Omega^{-1/2}$, a scaling of the wrinkling scale with Reynolds number is not surprising. The exact dependence of the wrinkling scale on the Reynolds number needs to be carefully investigated.

The evolution of flame brush thickness depends on the Lagrangian velocity auto-correlation function, which is expected to deviate significantly from the expression used for the analysis of spherical turbulent flames due to inhomogeneity and anisotropy. Nevertheless, the mean velocity field and normalized RMS fluctuations are independent of Reynolds number, so the growth of turbulent flame brush thickness may be expected to be similar across the three von Kármán configurations S1, S2 and S3.

In summary, the temporal development of the two quantities, the thickness of turbulent flame brush δ_T and the wrinkling length scale $L^* \sim \Sigma_{\max}^{-1}$ is complicated by mean shear and anisotropic turbulence. However, it may be argued that the turbulent flame brush evolves similarly across the three configurations, while the wrinkling scale would decrease as $\mathrm{Re}_\Omega^{-1.13/2}$. As a result, the same Reynolds scaling of surface area is observed when different configurations are compared against each other.

Chapter 7

Summary and Conclusions

The work presented in this dissertation is concerned with the evolution of reactive-diffusive surfaces in turbulent flows. First, a framework based on the popular surface density function formalism was developed to analyze the growth rate of surface area of reactive fronts. A canonical configuration of turbulent flames in decaying isotropic turbulence was investigated using a database of direct numerical simulations (DNS) with finite rate chemistry for lean premixed methane/air mixtures at elevated pressure and temperature. Subsequently, a more practical flow configuration of the swirling von Kármán flow was considered.

The primary contribution of this dissertation is the conceptualization of the probability density function of the radial distance $\mathcal{P}$, its association with the surface density function and the derivation and analysis of the evolution equations of the peak flame surface density and thickness of the turbulent flame brush.

A summary of prominent results is presented below. The discussion is grouped into sections according to different lines of inquiries on scaling of various quantities that control the growth of reactive surfaces. Limitations

of the present work and the author's recommendations for future work are included also.

7.1 Turbulent flame brush thickness

Taylor's theory of turbulent diffusion [109] is often employed to analyze the growth of turbulent flame brush in unsteady and spatially developing flows. Although the theory was originally developed for dispersion of material elements in isothermal turbulence, it is often argued that the turbulent flame brush evolves similar to the dispersion thickness of material elements in the limit of high turbulence intensity u'/S_L. In many practical flow configurations u'/S_L is not much larger than unity and decreases due to temporal or spatial decay downstream of the flame-holder. Under these conditions, several additional mechanisms play a role in the development of turbulent flame brush also. Incorporating these mechanisms in a modified theory based on turbulent diffusion theory of Taylor is complicated since the theory is Lagrangian while most turbulent modeling approaches are Eulerian.

The analysis in Chap. 3 presented an alternate approach based on the surface density function and is inherently Eulerian. It was shown that the turbulent transport term of the governing equation for the brush thickness is consistent with the turbulent diffusion theory and the limiting behavior of $u'/S_L \gg 1$ is recovered. The importance of two additional mechanisms was highlighted and their scaling with relevant quantities was discussed.

The first effect is due to the mean velocity field induced due to the

density difference across the propagating front. The flame surface in the trailing part (closer to the products) of the brush moves slower compared to the leading part (closer to the reactants), and further aids in the growth of the turbulent flame brush thickness.

Another important effect is due to response of flame propagation to local surface curvature. Since flame is predominantly curved towards reactants in the trailing part and towards products in the leading part, flame stretch shows a strong variation across the flame brush. As a result, flame stretch acts as a sink of the flame surface area in the trailing part and as a source in the leading part of the brush and acts to reduce the thickness of the flame brush.

A balance between these three mechanisms leads to an asymptotic value of the flame brush thickness, contrary to the theoretical predictions of a continuous growth of the flame brush thickness based on Taylor's theory alone. Since the evolution of flame brush thickness directly affects that of the flame surface area and turbulent burning rates, inclusion of these terms in modeling is essential.

The success of the proposed theory was demonstrated by considering experimental observations of the evolution of turbulent flame brush thickness in various flame configurations. Specifically, the role of thermo-chemical parameters such as laminar flame speed, pressure and equivalence ratio of the growth of the flame brush was explained qualitatively.

7.2 The wrinkling scale

The surface of a turbulent premixed flame is wrinkled by a wide range of scales of turbulent motion. Coherent structures in turbulence create folds of the order of their linear extent on the order of their characteristic time scale. The interaction of the surface with large, energy containing coherent motions is slow, while the fast, dissipative scales of the order of Kolmogorov scale do not contain sufficient energy to significantly wrinkle the flame surface. The wrinkling scale, which is proportional to the inverse of the peak flame surface density function is thus smaller than the integral scale but larger than the Kolmogorov length scale.

Inspired by the Bray-Moss-Libby approach [14, 13], an expression for the surface density function based on flamelet crossing frequency was derived for the thin reaction zone regime. The analysis presented in Chap. 4 shows that the BML theory can be extended to the thin reaction zone regime by inclusion of a correction factor Υ, which is a function of conditional moments of the gradient of progress variable. Leveraging the BML theory and associated experimental data, it was argued that the wrinkling scale is a characteristic scale of turbulence in the reactants.

An evolution equation for the peak flame surface density was derived by estimating the location of the peak based on a Gaussian model for the probability density function $\mathcal{P}$ and subsequently evaluating the terms of the surface density transport equation at the peak. As with the evolution of the flame brush thickness, the peak flame surface density is controlled by a balance

of transport terms due to turbulent diffusion and mean velocity field and flame stretch.

Scaling of the three mechanisms with relevant scales was discussed and compared against the DNS data. The turbulent transport term is proportional to the RMS velocity fluctuation u' and inversely proportional to the turbulent flame brush thickness. The mean transport term is governed by the fuel burning rate and scales as a reference scale for thermodynamic pressure rise and the domain size. A good agreement between flame stretch with stretch rate of infinitesimal material elements in isotropic turbulence for the same range of Reynolds number was observed. The flame stretch components scale with instantaneous Kolmogorov time scale τ_η, but a residual temporal variation is observed for propagation-curvature component also.

The combined effect of the three mechanisms on the peak flame surface density is such that the ratio of integral scale l to the wrinkling scale L^* increases with Reynolds number as $l/L^* \sim \mathrm{Re}_\lambda^{1.13}$, characteristic of a hydrodynamic length scale.

7.3 Scaling of flame surface area and burning rates

Scaling of turbulent burning rates of premixed flames was investigated using direct numerical simulations of spherical flames in decaying isotropic turbulence. It was shown that the burning rates are enhanced primarily through the increase in the flame's surface area, which is in turn shown to be proportional to the product of the thickness of turbulent flame brush and the peak

of the surface density function within. Analysis of the two quantities suggest that large, energy containing motions of turbulent motion control the evolution of the flame brush thickness, while small, dissipative motions of the order of Taylor length scale control the peak surface density function. As a result, the area ratio and turbulent burning rates increase with Taylor Reynolds number as $\mathrm{Re}_\lambda^{1.13}$.

A similar scaling of the surface area of the reactive-diffusive fronts was observed in swirling von Kármán flow also. Despite the turbulent flow being inhomogeneous, anisotopic and in the absence of density change across the moving front, the broad scaling relation $A \sim \mathrm{Re}_\lambda^{1.13} \sim \mathrm{Re}_\Omega^{1.13/2}$ was observed, when surface area was compared across the three configurations at instances when volume enclosed by the surface was equal. A detailed analysis of scaling of flame brush thickness and wrinkling scale requires extending the framework to incorporate effects of mean shear, anisotropic turbulence, and multiple non-ergodic spatial directions and was left for a future work.

7.4 Recommendations for future work

The work presented in this dissertation may be extended along the following lines of inquiry to further the understanding of evolution of reactive surfaces in turbulence.

1. **A generalized theory for the growth of turbulent flame brush:**

   The formalism based on the probability density function of the radial

distance may be generalized to other turbulent flame configurations as follows. For a given turbulent flame configuration, the mean location of the flame surface may be obtained by averaging over an ensemble of repeated runs. For thin flames, the mean location often coincides with the location where Reynolds-averaged progress variable $\overline{C} = 0.5$. A distance function may be defined on the instantaneous isosurface representing the flame from the mean location, which is a random variable whose standard deviation is proportional to the brush thickness. If the distance function is related to the flame surface density function, an evolution equation for the brush thickness can be derived as demonstrated in the context of spherical turbulent flames.

A general analysis of various mechanisms that affect the evolution of flame brush thickness will reveal its dependence on various dimensionless groups and on evolution of surface area of turbulent flames.

2. **Role of other dimensionless groups in flame stretch term T_4:**

   Modeling of the two additional mechanisms apart from turbulent diffusion, namely the gradient of mean velocity field across the brush and the differential flame stretch, requires targeted work to identify how various relevant dimensionless groups affect burning rates and evolution of flame curvature. The differential flame stretch term is sensitive to hydrodynamic and diffusional-thermal instabilities through its dependence on the curvature and may be control by a number of dimensionless group such as Karlovitz number, Damköhler number and the Peclet number.

3. **Reynolds scaling of wrinkling scale:**

   The analysis of mechanisms that affect the wrinkling scale demonstrated that the balance of these terms leads to the Reynolds scaling, $l/L^* \sim \mathrm{Re}_\lambda^{1.13}$. The scaling of mean transport term is geometry dependent, leading to a different exponent across different flow configurations. On the other hand the scaling of turbulent transport term with turbulence intensity u' and that of the flame stretch term with Kolmogorov time scale τ_η may more be general. As a result, the wrinkling scale may depend on configuration and other dimensionless group, but may approximately be equal to the Taylor scale $\lambda \sim u'\tau_\eta$. This hypothesis can only be validated by analyzing the peak flame surface density for a variety of conditions.

4. **A wider Reynolds number range:**

   The Reynolds number range investigated in the numerical simulations of spherical turbulent flames and of the evolution of reactive surfaces in the von Kármán flow device was rather limited. For turbulent spherical flames, the use of finite rate chemistry increased the cost by about a factor of five, while for the von Kármán flow device a large number of repetitions drive the cost higher, although a single simulation run is fairly inexpensive.

   As a result, the Taylor Reynolds number range investigated in the two geometries is in the range $\mathrm{Re}_\lambda \sim 30 - 100$, which is fairly low to see an asymptotic limit if one exists. Repeating the experiments at much

higher Reynolds numbers is desired and recommended.

5. **Influence of density ratio and pressure rise in reaction von Kármán device:**

   The reactive-diffusive fronts examined in the numerical experiments of reactive von Kármán flow considered an ideal front that introduces no density change. For premixed turbulent flames the density ratio across the front is typically between 2-7 and its effect on the Reynolds scaling needs to be investigated.

   The author recommends the following approach to incorporate effects of variable density and pressure within the framework of a single equation for the progress variable and immersed boundary method.

   The variation of density across the front may be modeled as

$$\rho(\mathbf{x},t) = \rho(C(\mathbf{x},t)) = \rho_u \left\{1 + (\zeta - 1)C\right\}^{-1}, \tag{7.1}$$

   where $\rho_u = \rho_u(t)$ is the reactants' density and ζ the ratio of densities of reactants and products. This expression mimics the effect of temperature on density in isobaric flow, $\rho \sim T^{-1}$.

   The dependence of reactant density on thermodynamic pressure may be modeled with an isentropic compression

$$\rho_u/\rho_{u,0} = (p(t)/p_0)^{1/\gamma}, \tag{7.2}$$

   where γ is the ratio of specific heats and the thermodynamic pressure $p = p(t)$ increases in time.

Consistently with the conservation of mass inside the domain enclosed by the immersed boundaries, the following condition must be enforced

$$m = \int_V \mathbb{I}\rho(\mathbf{x}, t = 0)\ dV = \int_V \mathbb{I}\rho(\mathbf{x}, t)\ dV, \tag{7.3}$$

where $\mathbb{I}$ denotes an indicator function that equals unity inside the enclosed domain and zero outside. Substituting the expression for density in the equation above, a model for thermodynamic pressure rise may be obtained as

$$p(t)/p_0 = m^\gamma \left(\int_V \rho_{u,0}\, \mathbb{I}(\mathbf{x})\ \{1 + (\zeta - 1)C(\mathbf{x}, t)\}^{-1}\ dV \right)^{-\gamma}. \tag{7.4}$$

Similarly, the change in the dynamic viscosity and diffusivity may be modeled with a Sutherland expression

$$\mu/\mu_{u,0} = \mathcal{D}_C/\mathcal{D}_{C,0} = \frac{1 + a}{M + a} M^{3/2}, \tag{7.5}$$

where

$$M = (p/p_0)^{\gamma - 1/\gamma}\, (1 + (\zeta - 1)C) \tag{7.6}$$

and a is a modeling constant.

This approach was investigated briefly, but led to convergence issues with the iterative solver for the Poisson equation for the hydrodynamic pressure $\pi(\mathbf{x}, t)$. The simplified model with no density or viscosity change across the front was adopted in the interest of time.

Appendices

Appendix A

Statistical convergence from a single simulation run

All statistics presented for turbulent spherical flames were gathered from a single simulation run. For convergence of reported statistics, ensemble averaging over multiple independent runs with same nominal initial turbulence is desired, but computationally prohibitive due to high cost of finite rate chemistry calculations. This appendix discusses the statistical convergence using a simulation run, which was ensured by designing the spherical flame configurations so that multiple independent realization of underlying turbulence-flame interaction process exist in any simulation run.

Consider that an ensemble of $\mathcal{N}$ simulations is available. Define the flame surface area as a random process $\tilde{A}(t)$ with $\tilde{A}^n(t)$ denoting repetition n of $\mathcal{N}$. Then, the mean of the flame surface area is

$$A(t) = \left\langle \tilde{A}(t) \right\rangle = \left\langle \left\langle \tilde{A}(t) \right\rangle_{\mathcal{N}} \right\rangle = \left\langle \frac{1}{\mathcal{N}} \sum_{n=1}^{\mathcal{N}} \tilde{A}^n(t) \right\rangle \tag{A.1}$$

where $\langle . \rangle$ here denotes statistical expectation and $\langle . \rangle_{\mathcal{N}}$ indicates ensemble averaging over $\mathcal{N}$ repetitions [94]. The two are identical in the limit of $\mathcal{N} \to \infty$.

The random process $\tilde{A}(t)$ is functionally related to the progress variable

random field $C(\mathbf{x}, t)$ [77],

$$\tilde{A}(t) = \int_V |\nabla C(\mathbf{x}, t)| \delta[C(\mathbf{x}, t) - c^*] \, dV, \tag{A.2}$$

where δ is the Dirac-delta function and $C(\mathbf{x}, t) = c^*$ is the isosurface taken to represent the flame, so that

$$A(t) \equiv \left\langle \left\langle \tilde{A}(t) \right\rangle_{\mathcal{N}} \right\rangle = \left\langle \left\langle \int_V |\nabla C| \delta(C - c^*) \right\rangle_{\mathcal{N}} \right\rangle. \tag{A.3}$$

Rearranging the order by which the statistical expectation, ensemble average and volumetric integral are taken, it follows that

$$A(t) = \int_V \langle \langle |\nabla C| \delta(C - c^*) \rangle_{\mathcal{N}} \rangle \, dV = \int_V \langle \langle \tilde{\Sigma} \rangle_{\mathcal{N}} \rangle \, dV, \tag{A.4}$$

where the $\tilde{\Sigma}$ is defined as the expectation of the spherically random field $\tilde{\Sigma}(\mathbf{x}, t) \equiv |\nabla C| \delta(C - c^*)$. The random field $\tilde{\Sigma}$ is commonly referred to as the 'fine grained surface density function' in the literature [117].

For each repetition n of $\mathcal{N}$, spherical averaging of $\tilde{\Sigma}$,

$$\left\langle \tilde{\Sigma} \right\rangle_{\Theta\Phi} = \frac{1}{4\pi r^2} \int_0^{2\pi} \int_0^{\pi} \tilde{\Sigma}(r, \Theta, \Phi, t) r^2 \sin\theta \, d\Theta \, d\Phi, \tag{A.5}$$

where Θ and Φ denote the polar and azimuthal angle of the spherical coordinate system, is an estimate for $\left\langle \tilde{\Sigma} \right\rangle$ consistent with the statistical symmetry of the random field.

Based on Eq. (A.5), Eq. (A.3) can be written as

$$A(t) \equiv \left\langle \tilde{A}(t) \right\rangle \approx \int_V \left\langle \left\langle \tilde{\Sigma}_{\Theta\Phi} \right\rangle_{\mathcal{N}} \right\rangle \, dV = 4\pi \int_0^{\infty} r^2 \left\langle \left\langle \tilde{\Sigma}_{\Theta\Phi} \right\rangle \right\rangle \, dr. \tag{A.6}$$

In the last step $\left\langle \tilde{\Sigma} \right\rangle_{\Theta\Phi}$ depends on (r,t) only, since the dependence of $\tilde{\Sigma}$ on Θ and Φ has been averaged out.

The mean of the flame surface area is the volumetric integral of the flame surface density function Σ,

$$A(t) = \int_V \Sigma \, dV = 4\pi \int_0^\infty r^2 \Sigma(r,t) \, dr, \tag{A.7}$$

since $\Sigma = \Sigma(r,t)$ only for the unsteady spherically symmetric flame configuration. Equating Eq. (A.7) and Eq. (A.6) brings

$$A(t) = 4\pi \int_0^\infty r^2 \Sigma(r,t) \, dr \approx 4\pi \int_0^\infty r^2 \left\langle \left\langle \tilde{\Sigma} \right\rangle_{\Theta\Phi} \right\rangle_{\mathcal{N}} dr, \tag{A.8}$$

which implies, as expected, that $\left\langle \left\langle \tilde{\Sigma} \right\rangle_{\Theta\Phi} \right\rangle_{\mathcal{N}}$ is an approximation to Σ and that the statistical error inherent in the estimation of $A(t)$ depends on the number of repetitions $\mathcal{N}$ and the variance of the spherical average $\left\langle \tilde{\Sigma} \right\rangle_{\Theta\Phi}$.

The central limit theorem may be applied to spherical averages of spatially discrete solutions noting that surface averages are approximated by summations so that $\mathrm{var}\left[\left\langle \tilde{\Sigma} \right\rangle_{\Theta\Phi}\right] = \mathrm{var}[\tilde{\Sigma}]/\mathcal{M}_r$, where $\mathrm{var}[U]$ indicates the variance of a random variable U and $\mathcal{M}_r$ the number of independent and identically distributed (i.i.d.) samples gathered on the surface of radius r.

The present flame configurations were designed to have large R/l ratios, i.e. the flame radius is large compared to the integral scale of velocity, leading to very many i.i.d. samples of $\tilde{\Sigma}$. Consequently, $\mathrm{var}[\left\langle \tilde{\Sigma} \right\rangle_{\Theta\Phi}]$ is small and one repetition ($\mathcal{N} = 1$) is sufficient to obtain a close estimate of the flame surface density function and associated statistical measures.

For example, similar considerations apply to $R(t) = \left\langle \tilde{R}(t) \right\rangle$ by defining the random process

$$\tilde{R}(t) \equiv \frac{1}{A(t)} \int_V ||\mathbf{x}|| |\nabla C(\mathbf{x}, t)| \delta[C(\mathbf{x}, t) - c^*] \, dV, \tag{A.9}$$

which is the instantaneous surface averaged Euclidean (radial) distance $r(\mathbf{x}) = ||\mathbf{x}||$ of the flame surface from the origin located at the center of the computational domain. Then it follows that

$$R(t) \equiv \left\langle \tilde{R}(t) \right\rangle = \left\langle \left\langle \tilde{R}(t) \right\rangle_{\mathcal{N}} \right\rangle \approx \frac{4\pi}{A(t)} \int_0^\infty r^3 \left\langle \left\langle \tilde{\Sigma} \right\rangle_{\Theta\Phi} \right\rangle_{\mathcal{N}} dr. \tag{A.10}$$

Appendix B

Data regularization

The flame surface statistics for turbulent spherical flames are gathered from a single simulation run. Although the statistics of the radial distance are well converged due to a large number of independent samples in a single run, those involving spatial and temporal derivatives require a larger number of samples and may possess residual noise.

In particular, the statistics of the flame curvature and the flame stretch rate suffer from poor statistical convergence, since they involve conditional means of second order derivatives of the progress variable field. This in turn affects term the differential flame stretch term T_4 in the evolution equation for the turbulent flame brush thickness (Eq. (3.12)). On the other hand, the turbulent diffusion and the mean velocity terms are smooth and do not require any regularization.

The convergence may be improved by running multiple realizations starting from statistically the same initial conditions and averaging over all such simulation runs. However, this approach is computationally prohibitive for the three dimensional simulations featuring 1-5 Billion grid points and detailed finite rate chemistry calculations. Yet, within the limits of the present

database, useful qualitative and quantitative trends may be drawn for the scaling of the terms affecting the evolution of the flame brush thickness, once appropriate smoothing operations are performed. This appendix briefly describes the regularization operations conducted on the database of spherical turbulent flames.

Statistics that suffer with residual noise due to inadequate convergence are regularized in space and in time with the Tikhonov regularization procedure [60, 111]. The procedure evaluates a numerical derivative $\mathbf{u}$ of noisy data $\mathbf{y}$ by minimizing the functional

$$E(\alpha; \mathbf{u}) = ||A\mathbf{u} - \mathbf{y}||^2 + \alpha\Delta^k ||D_k\mathbf{u}||^2, \tag{B.1}$$

where Δ is the distance between the coordinate at which statistics are available, and α is the regularization parameter. The finite difference operator for k^{th} order is denoted as D_k, whereas A denotes the anti-derivative (integral) operator and has the same order of accuracy as that of D_k.

The user-controlled regularization parameter α controls the relative importance of the data fidelity between the anti-derivative of u and the noisy data y (the first term) and smoothness in the solution u, quantified as the magnitude of its k-th order derivative (second term). For each α , there exists a unique solution $\mathbf{u}$ which minimizes the functional E, given by

$$\mathbf{u} = \left(A^T A + \alpha\Delta^k D_k^T D\right)^{-1} A^T \mathbf{y}. \tag{B.2}$$

This procedure provides an estimate of the derivative $\mathbf{u}$ of noisy data y. Subsequently, the regularized field $\tilde{\mathbf{y}} = A\mathbf{u}$ is obtained from $\mathbf{u}$.

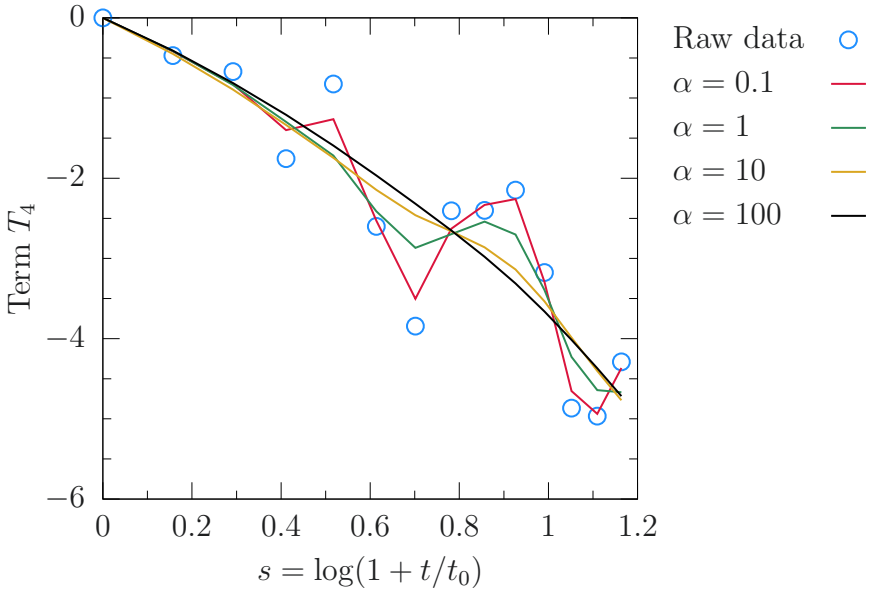

Figure B.1: Regularization of term T_4 from Eq. (3.12) with different values of the regularization parameter α for simulation R4K1.

Figure B.1 presents the raw data and smoothed approximation of term T_4 for flame R4K1 at various values of α. It can be seen that the data gets smoother with increasing values of α without losing the underlying temporal variation. The qualitative and quantitative conclusions of Sec. 3.2.3 are unaffected by the choice of α.

Appendix C

von Kármán device geometry

The design of the von Kármán device is reproduced from the configuration 'TM60' used by Ravelet *et. al.* [95]. More details on the geometry can be found in the work by Cortet *et. al.* [26].

Figure C.1 shows a schematic diagram of the geometry. A description of symbols, their values and references for the value are listed in Tab. C.1 below.

Symbol	Description	TM60 [mm]	Normalized by R	Source
R	Radius of cylinder	100	1	Ref. [95]
R_b	Radius of blades	92.5	0.925	Ref. [95]
H	Distance between impellers	180	1.8	Ref. [95]
H_R	Height of re-circulation zone	40	0.4	Ref. [53]
T	Thickness of impeller disks	20	0.2	Ref. [26]
R_h	Radius of the hub	10	0.1	Ref. [53]
h_b	Height of the blades	20	0.2	Ref. [95]
t_b	Thickness of the blades	2	0.02	Ref. [53]
R_c	Radius of curvature of blades	46.25	0.4625	Ref. [26]
		50	0.5	Ref. [95]
α	Exit angle of blades	72°	-	Ref. [53]

Table C.1: Geometrical dimensions of TM60. Ref. [53] refers to dimensions received from personal communication.

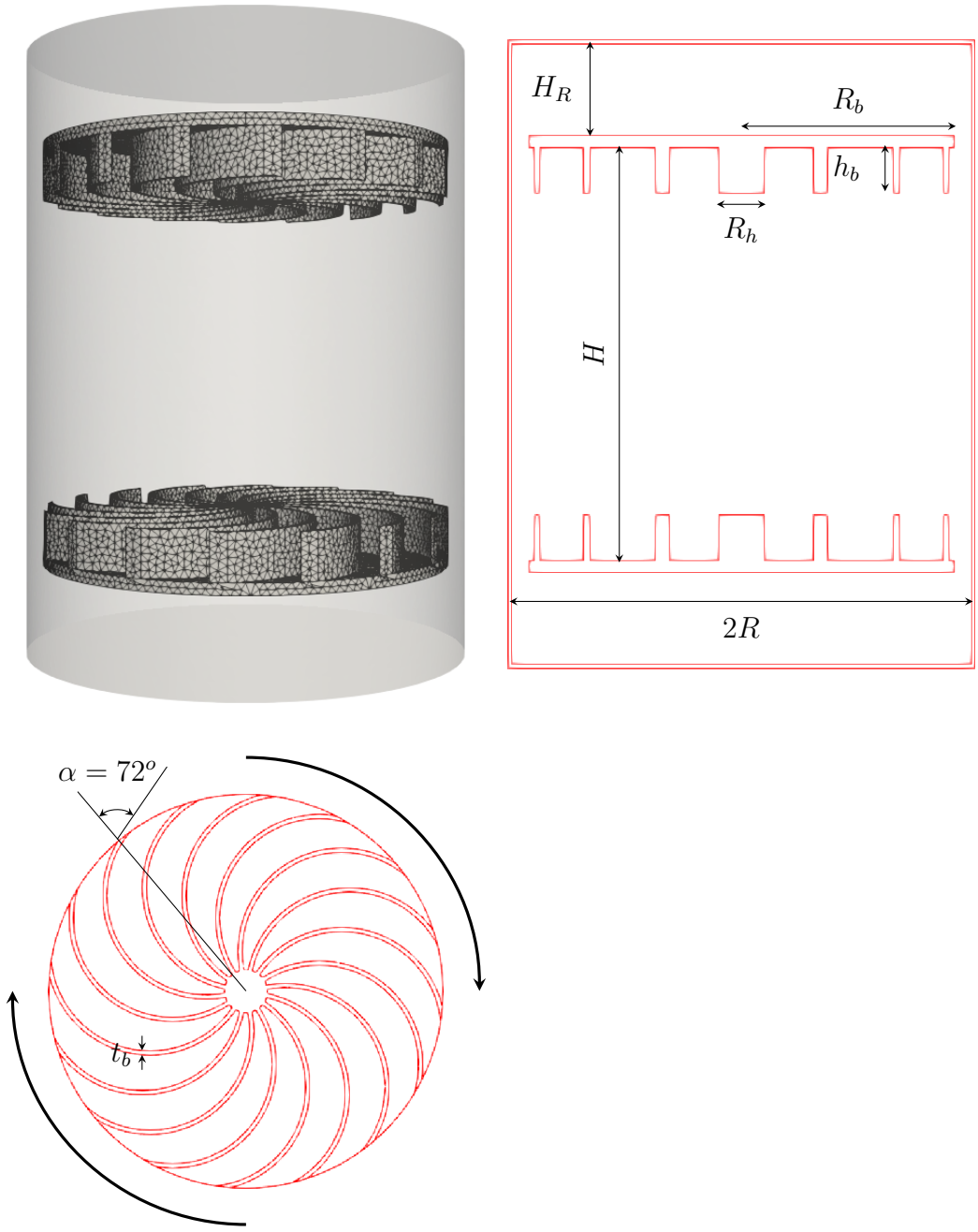

Figure C.1: Details of the von Kármán device geometry. Blades rotate in the same direction as the curvature of the blades.

Bibliography

[1] R. G. Abdel-Gayed and D. Bradley. Dependence of turbulent burning velocity on turbulent reynolds number and ratio of flaminar burning velocity to r.m.s. turbulent velocity. *Symp. (Int.) Combust.*, 16(1):1725 – 1735, 1977.

[2] R. G. Abdel-Gayed, D. Bradley, and P. Gray. A two-eddy theory of premixed turbulent flame propagation. *Phil. Trans. R. Soc. London, Ser. A*, 301(1457):1–25, 1981.

[3] I. Ahmed and N. Swaminathan. Simulation of spherically expanding turbulent premixed flames. *Combust. Sci. Technol.*, 185(10):1509–1540, 2013.

[4] G. E. Andrews, D. Bradley, and S. B. Lwakabamba. Measurement of turbulent burning velocity for large turbulent reynolds numbers. *Symp. (Int.) Combust.*, 15(1):655 – 664, 1975.

[5] W. T. Ashurst, A. R. Kerstein, R. M. Kerr, and C. H. Gibson. Alignment of vorticity and scalar gradient with strain rate in simulated Navier – Stokes turbulence. *Phys. Fluids*, 30(8):2343–2353, 1987.

[6] A. Attili and F. Bisetti. Statistics of scalar dissipation and strain / vorticity / scalar gradient alignment in turbulent nonpremixed jet flames.

103(3):625–642, Sep 2019.

[7] W. D. Baines and E. G. Peterson. An investigation of flow through screens. *Trans. Am. Soc. Mech. Engrs.*, 73, 1951.

[8] G. K. Batchelor. The effect of homogeneous turbulence on material lines and surfaces. *Proc. R. Soc. London, Ser. A*, 213(1114):349–366, 1952.

[9] G. K. Batchelor and A. A. Townsend. Decay of isotropic turbulence in the initial period. *Proc. R. Soc. London, Ser. A*, 193(1035):539–558, 1948.

[10] G. K. Batchelor and A. A. Townsend. Decay of turbulence in the final period. *Proc. R. Soc. London, Ser. A*, 194(1039):527–543, 1948.

[11] R. B. Bird, W. E. Stewart, and E. N. Lightfoot. *Transport phenomena*. John Wiley & Sons, Hoboken, New Jersey, 2 edition, 2006.

[12] R. Borghi. *On the Structure and Morphology of Turbulent Premixed Flames*, pages 117–138. Springer US, 1985.

[13] K. N. C Bray and P. A. Libby. Passage times and flamelet crossing frequencies in premixed turbulent combustion. *Combust. Sci. Technol.*, 47(5-6):253–274, 1986.

[14] K. N. C. Bray, P. A. Libby, and J. B. Moss. Flamelet crossing frequencies and mean reaction rates in premixed turbulent combustion. *Combust. Sci. Technol.*, 41(3-4):143–172, 1984.

[15] K. N. C. Bray and J. B. Moss. A unified statistical model of the premixed turbulent flame. *Acta Astronaut.*, 4(3-4):291–319, 1977.

[16] K.N.C. Bray, Paul A. Libby, and J.B. Moss. Unified modeling approach for premixed turbulent combustion—part i: General formulation. *Combust. Flame*, 61(1):87–102, 1985.

[17] S. M. Candel and T. Poinsot. Flame stretch and the balance equation for the flame area. *Combust. Sci. Technol.*, 70:1–15, 1990.

[18] R. S. Cant and K. N. C. Bray. Strained laminar flamelet calculations of premixed turbulent combustion in a closed vessel. *Symp. (Int.) Combust.*, 22(1):791–799, 1989.

[19] N. Chakraborty and R. S. Cant. Effects of strain rate and curvature on surface density function transport in turbulent premixed flames in the thin reaction zones regime. *Phys. Fluids*, 17(6):065108, 2005.

[20] S. Chaudhuri, V. Akkerman, and C. K. Law. Spectral formulation of turbulent flame speed with consideration of hydrodynamic instability. *Phys. Rev. E*, 84(2):026322, 2011.

[21] S. Chaudhuri, F. Wu, D. Zhu, and C. K. Law. Flame speed and self-similar propagation of expanding turbulent premixed flames. *Phys. Rev. Lett.*, 108(4):044503, 2012.

[22] A. J. Chorin. Numerical solution of the Navier-Stokes equations. *Math. Comput.*, 22:745–762, 1968.

[23] L. Cifuentes, C. Dopazo, J. Martin, and C. Jimenez. Local flow topologies and scalar structures in a turbulent premixed flame. *Phys. Fluids*, 26(6):065108, 2014.

[24] W. J. Cocke. Turbulent hydrodynamic line stretching: Consequences of isotropy. *Phys. Fluids*, 12(12):2488–2492, 1969.

[25] G. Comte-Bellot and S. Corrsin. Simple Eulerian time correlation of full- and narrow-band velocity signals in grid-generated, isotropic turbulence. *J. Fluid Mech.*, 48(2):273–337, 1971.

[26] P.-P. Cortet, A. Chiffaudel, F. Daviaud, and B. Dubrulle. Experimental evidence of a phase transition in a closed turbulent flow. *Phys. Rev. Lett.*, 105:214501, Nov 2010.

[27] F. Creta, R. Lamioni, P. E. Lapenna, and G. Troiani. Interplay of Darrieus - Landau instability and weak turbulence in premixed flame propagation. *Phys. Rev. E*, 94(5-1):053102, 2016.

[28] G. Damköhler. Der einflußder turbulenz auf die flammengeschwidigkeit in gasgemischen. *Z. Elektrochem. 46, 601–652, 1947, English translation NASA Tech. Mem*, 1112, 1940.

[29] G. Darrieus. Propagation d'un front de flamme. *La Technique Moderne*, 30:18, 1938.

[30] C. M. de Silva, J. Philip, K. Chauhan, C. Meneveau, and I. Marusic. Multiscale geometry and scaling of the turbulent-nonturbulent in-

terface in high Reynolds number boundary layers. *Phys. Rev. Lett.*, 111(4):044501, 2013.

[31] B. Deschamps, A. Boukhalfa, C. Chauveau, I. Gökalp, I. G. Shepherd, and R. K. Cheng. An experimental estimation of flame surface density and mean reaction rate in turbulent premixed flames. *Symp. (Int.) Combust.*, 24(1):469–475, 1992.

[32] O. Desjardins, G. Blanquart, G. Balarac, and H. Pitsch. High order conservative finite difference scheme for variable density low Mach number turbulent flows. *J. Comput. Phys.*, 227(15):7125–7159, 2008.

[33] J. F. Driscoll. Turbulent premixed combustion: Flamelet structure and its effect on turbulent burning velocities. *Prog. Energ. Combust. Sci.*, 34(1):91–134, 2008.

[34] I. T. Drummond. Stretching and bending of line elements in random flows. *J. Fluid Mech.*, 252:479–498, 1993.

[35] I. T. Drummond and W. Münsch. Turbulent stretching of line and surface elements. *J. Fluid Mech.*, 215:45–59, 1990.

[36] M. Fairweather, M.P. Ormsby, C.G.W. Sheppard, and R. Woolley. Turbulent burning rates of methane and methane–hydrogen mixtures. *Combust. Flame*, 156(4):780–790, 2009.

[37] R. D. Falgout, J. E. Jones, and U. M. Yang. The design and implementation of Hypre, a library of parallel high performance preconditioners.

In *Numerical solution of partial differential equations on parallel computers*, pages 267–294. Springer, 2006.

[38] R. A. Fisher. The wave of advance of advantageous genes. *Annals of Eugenics*, 7(4):355–369, 1937.

[39] N. Fogla, F. Creta, and M. Matalon. Influence of the darrieus-landau instability on the propagation of planar turbulent flames. *Proc. Combust. Inst.*, 34(1):1509 – 1517, 2013.

[40] D. Fries, B. Ochs, A. Saha, D. Ranjan, and S. Menon. Flame speed characteristics of turbulent expanding flames in a rectangular channel. *Combust. Flame*, 199:1–13, 2019.

[41] U. Frisch. *Turbulence: the legacy of AN Kolmogorov*. Cambridge University Press, 1995.

[42] S. S. Girimaji. Asymptotic behavior of curvature of surface elements in isotropic turbulence. *Phys. Fluids*, 3(7):1772–1777, 1991.

[43] S. S. Girimaji and S. B. Pope. Material-element deformation in isotropic turbulence. *J. Fluid Mech.*, 220:427–458, 1990.

[44] S. S. Girimaji and S. B. Pope. Propagating surfaces in isotropic turbulence. *J. Fluid Mech.*, 234:247–277, 1992.

[45] A. C. Hindmarsh, P. N. Brown, K. E. Grant, S. L. Lee, R. Serban, D. E. Shumaker, and C. S. Woodward. SUNDIALS: suite of nonlinear and

differential/algebraic equation solvers. *ACM Trans. Math. Software*, 31:363–396, 2005.

[46] J. O. Hinze. *Turbulence*. McGraw-Hill, New York, 1975.

[47] J. Hirschfelder, C. Curtiss, R. Bird, and M. Mayer. *Molecular theory of gases and liquids*. Wiley New York, 1954.

[48] M. J. Huang and A. Leonard. Velocity autocorrelations of decaying isotropic homogeneous turbulence. *Phys. Fluids*, 7(10):2455–2464, 1995.

[49] K. Y. Huh, J. Kwon, and D. Lee. Relationships for maximum flame surface density and brush thickness through conditional analysis in turbulent premixed combustion. *Phys. Fluids*, 25(7):075108, 2013.

[50] K. W. Jenkins, M. Klein, N. Chakraborty, and R. S. Cant. Effects of strain rate and curvature on the propagation of a spherical flame kernel in the thin-reaction-zones regime. *Combust. Flame*, 145(1):415–434, 2006.

[51] L. J. Jiang, S. S. Shy, W. Y. Li, H. M. Huang, and M. T. Nguyen. High-temperature, high-pressure burning velocities of expanding turbulent premixed flames and their comparison with bunsen-type flames. *Combust. Flame*, 172:173–182, 2016.

[52] B. Karlovitz. Open turbulent flames. *Symp. (Int.) Combust.*, 4(1):60–67, 1953. Fourth Symposium (International) on Combustion.

[53] M. H. Kasbaoui, T. Kulkarni, and F. Bisetti. Direct numerical simulations of the swirling von kármán flow using a semi-implicit moving immersed boundary method. *Comput. Fluids*.

[54] S. Kheirkhah and Ö. L. Gülder. Topology and brush thickness of turbulent premixed V-shaped flames. 93(3):439–459, 2014.

[55] J. Kim and P. Moin. Application of a fractional-step method to incompressible navier-stokes equations. *J. Comput. Phys.*, 59(2):308–323, 1985.

[56] H. Kobayashi, K. Seyama, H. Hagiwara, and Y. Ogami. Burning velocity correlation of methane/air turbulent premixed flames at high pressure and high temperature. *Proc. Combust. Inst.*, 30(1):827–834, 2005.

[57] H. Kobayashi, T. Tamura, K. Maruta, T. Niioka, and F. A. Williams. Burning velocity of turbulent premixed flames in a high-pressure environment. *Symp. (Int.) Combust.*, 26(1):389–396, 1996.

[58] W. Kollmann and J.H. Chen. Dynamics of the flame surface area in turbulent non-premixed combustion. *Symp. (Int.) Combust.*, 25(1):1091–1098, 1994.

[59] A. Kolmogoroff, I. Petrovsky, and .N Piscounoff. Study of the diffusion equation with growth of the quantity of matter and its application to a biology problem. In *Dynamics of Curved Fronts*, pages 105–130. Elsevier, 1988.

[60] R. Kress. *Numerical Analysis*, chapter Tikhonov Regularization, pages 86–90. Springer, 1981.

[61] L. D. Landau. On the theory of slow combustion. *Acta Physicochim.*, 19:77–85, 1944.

[62] C. J. Lawn and R. W. Schefer. Scaling of premixed turbulent flames in the corrugated regime. *Combust. Flame*, 146:180–199, 2006.

[63] P. A. Libby and K. N. C. Bray. Implications of the laminar flamelet model in premixed turbulent combustion. *Combust. Flame*, 39(1):33–41, 1980.

[64] A. Lipatnikov. *Fundamentals of premixed turbulent combustion*, chapter 4. CRC Press, 2012.

[65] A. N. Lipatnikov and J. Chomiak. Turbulent flame speed and thickness: phenomenology, evaluation, and application in multi-dimensional simulations. *Prog. Energ. Combust. Sci.*, 28(1):1–74, 2002.

[66] A. N. Lipatnikov, W. Y. Li, L. J. Jiang, and S. S. Shy. Does density ratio significantly affect turbulent flame speed? 98:1153–1172, 2017.

[67] C. C. Liu, S. S. Shy, M. W. Peng, C. W. Chiu, and Y. C. Dong. High-pressure burning velocities measurements for centrally-ignited premixed methane/air flames interacting with intense near-isotropic turbulence at constant Reynolds numbers. *Combust. Flame*, 159:2608–2619, 2012.

[68] X. D. Liu, S. Osher, and T. Chan. Weighted Essentially Non-oscillatory Schemes. *J. Comput. Phys.*, 115:200–212, 1994.

[69] S. Luca, A. N. Al-Khateeb, A. Attili, and F. Bisetti. Comprehensive validation of skeletal mechanism for turbulent premixed methane–air flame simulations. *J. Propul. Power*, 34:153–160, 2018.

[70] S. Luca, A. Attili, E. Lo Schiavo, F. Creta, and F. Bisetti. On the statistics of flame stretch in turbulent premixed jet flames in the thin reaction zone regime at varying Reynolds number. *Proc. Combust. Inst.*, 37(2):2451–2459, 2018.

[71] S. Luca, A. Attili, E. L. Schiavo, F. Creta, and F. Bisetti. On the statistics of flame stretch in turbulent premixed jet flames in the thin reaction zone regime at varying reynolds number. *Proc. Combust. Inst.*, 37(2):2451–2459, 2019.

[72] J. L. Lumley. Computational modeling of turbulent flows. volume 18 of *Advances in Applied Mechanics*, pages 123–176. Elsevier, 1979.

[73] B. B. Mandelbrot. On the geometry of homogeneous turbulence, with stress on the fractal dimension of the iso-surfaces of scalars. *J. Fluid Mech.*, 72(3):401–416, 1975.

[74] F. E. Marble and J. E. Broadwell. The coherent flame model for turbulent chemical reactions. Technical report, Purdue Univ Lafayette in Project Squid Headquarters, 1977.

[75] M. Matalon and B. J. Matkowsky. Flames as gasdynamic discontinuities. *J. Fluid Mech.*, 124:239–259, 1982.

[76] S. Mathur, P. K. Tondon, and S. C. Saxena. Thermal conductivity of binary, ternary and quaternary mixtures of rare gases. *Mol. Phys.*, 12:569–579, 1967.

[77] V. Maz'ya. *Sobolev spaces*, chapter 1.2.4, page 37. Springer, 1985.

[78] B. J. McBride, S. Gordon, and M. A. Reno. Coefficients for calculating thermodynamic and transport properties of individual species. Technical report, National Aeronautics and Space Administration, 1993. Technical Memorandum 4513.

[79] M. S. Mohamed and J.C. Larue. The decay power law in grid-generated turbulence. *J. Fluid Mech.*, 219:195–214, 1990.

[80] B. Mueller. Low Mach number asymptotics of the Navier-Stokes equations and numerical implications. In *Lecture Series, von Kármán Institute for Fluid Dynamics*, 1999.

[81] Y. Nie, J. Wang, W. Zhang, M. Chang, M. Zhang, and Z. Huang. Flame brush thickness of lean turbulent premixed bunsen flame and the memory effect on its development. 242:607 – 616, 2019.

[82] G. Nivarti and S. Cant. Direct numerical simulation of the bending effect in turbulent premixed flames. *Proc. Combust. Inst.*, 36(2):1903–1910, 2017.

[83] D. W. Peaceman and H. H. Rachford. The numerical solution of parabolic and elliptic differential equations. *J. Soc. Indust. Appl. Math.*, 3:28–41, 1955.

[84] P. Pelce and P. Clavin. Influence of hydrodynamics and diffusion upon the stability limits of laminar premixed flames. *J. Fluid Mech.*, 124:219–237, 1982.

[85] N. Peters. A spectral closure for premixed turbulent combustion in the flamelet regime. *J. Fluid Mech.*, 242:611–629, 1992.

[86] N. Peters. The turbulent burning velocity for large-scale and small-scale turbulence. *J. Fluid Mech.*, 384:107–132, 1999.

[87] N. Peters. *Turbulent Combustion*. Cambridge University Press, 2000.

[88] N. Peters. *Turbulent combustion*. IOP Publishing, 2001.

[89] C. D. Pierce. *Progress-variable approach for large-eddy simulation of turbulent combustion*. PhD thesis, Stanford University, 2001.

[90] A. Pocheau. Front propagation in a turbulent medium. *Europhys. Lett.*, 20(5):401–406, 1992.

[91] T. Poinsot and D. Veynante. *Theoretical and numerical combustion*. Centre Européen de Recherche et de Formation Avancée en Calcul Scientifique, Toulouse, France, 3 edition, 2012.

[92] S. B. Pope. The evolution of surfaces in turbulence. *Int. J. Eng. Sci.*, 26(5):445–469, 1988.

[93] S. B. Pope. *Reynolds-stress and related models*, pages 387–462. Cambridge University Press, 2000.

[94] S. B. Pope. *Turbulent flows*. Cambridge University Press, Cambridge, United Kingdom, 2000.

[95] F. Ravelet, A. Chiffaudel, and F. Daviaud. Supercritical transition to turbulence in an inertially driven von Kármán closed flow. *J. Fluid Mech.*, 601:339–364, 2008.

[96] B. Renou, A. Mura, E. Samson, and A. Boukhalfa. Characterization of the local flame structure and the flame surface density for freely propagating premixed flames at various lewis numbers. *Combust. Sci. Technol.*, 174(4):143–179, 2002.

[97] C. Rosales and C. Meneveau. Linear forcing in numerical simulations of isotropic turbulence: Physical space implementations and convergence properties. *Phys. Fluids*, 17(9):095106, 2005.

[98] Z. S. She, E. Jackson, S. A. Orszag, J. C. R. Hunt, O. M. Phillips, and D. Williams. Structure and dynamics of homogeneous turbulence: models and simulations. *Proc. R. Soc. London, Ser. A*, 434(1890):101–124, 1991.

[99] K. I. Shelkin. On combustion in a turbulent flow. 13(9 - 10):520 – 530, 1943. NASA Tech. Mem. 1110.

[100] S. S. Shy, W. K. I, E. I. Lee, and T. S. Yang. Experimental analysis of flame surface density modeling for premixed turbulent combustion using aqueous autocatalytic reactions. *Combust. Flame*, 118(4):606–618, 1999.

[101] S. S. Shy, E. I. Lee, N. W. Chang, and S. I. Yang. Direct and indirect measurements of flame surface density, orientation, and curvature for premixed turbulent combustion modeling in a cruciform burner. *Proc. Combust. Inst.*, 28(1):383–390, 2000.

[102] A. J. Simonsen and P.-Å. Krogstad. Turbulent stress invariant analysis: Clarification of existing terminology. *Phys. Fluids*, 17(8):088103, 2005.

[103] M. Sinhuber, E. Bodenschatz, and G. P. Bewley. Decay of turbulence at high Reynolds numbers. *Phys. Rev. Lett.*, 114:034501, 2015.

[104] G. P. Smith, D. M. Golden, M. Frenklach, N. W. Moriarty, B. Eiteneer, M. Goldenberg, C. T. Bowman, R. K Hanson, S. Song, W. C. Gardiner Jr, et al. Gri-mech version 3.0, 1999.

[105] K. R. Sreenivasan. Fractals and multifractals in fluid turbulence. *Annu. Rev. Fluid Mech.*, 23(1):539–604, 1991.

[106] K. R. Sreenivasan and C. Meneveau. The fractal facets of turbulence. *J. Fluid Mech.*, 173:357–386, 1986.

[107] M. Tabor and I. Klapper. Stretching and alignment in chaotic and turbulent flows. *Chaos Solitons Fract.*, 4:1031–1055, 1994.

[108] P. Tamadonfar and Ö. Gülder. Flame brush characteristics and burning velocities of premixed turbulent methane/air bunsen flames. *Combust. Flame*, 161(12):3154–3165, 2014.

[109] G. I. Taylor. Diffusion by continuous movements. *Proc. R. Soc. London, Ser. A*, 2(1):196–212, 1922.

[110] G. I. Taylor. Statistical theory of turbulence. *Proc. R. Soc. London, Ser. A*, 151(873):421–444, 1935.

[111] A. N. Tikhonov. On solving ill-posed problem and method of regularization. *Doklady Akademii Nauk USSR*, 153:501–504, 1963.

[112] A. G. Tomboulides, J. C. Y. Lee, and S. A. Orszag. Numerical simulation of low Mach number reactive flows. *J. Sci. Comput.*, 12(2):139–167, 1997.

[113] A. Trouvé and T. Poinsot. The evolution equation for the flame surface density in turbulent premixed combustion. *J. Fluid Mech.*, 278:1–31, 1994.

[114] A. Tsinober. *An informal conceptual introduction to turbulence*, volume 483. Springer, 2009.

[115] A. Tsinober, E. Kit, and T. Dracos. Experimental investigation of the field of velocity gradients in turbulent flows. *J. Fluid Mech.*, 242:169–192, 1992.

[116] M. Uhlmann. An immersed boundary method with direct forcing for the simulation of particulate flows. *J. Comput. Phys.*, 209(2):448–476, November 2005.

[117] L. Vervisch, E. Bidaux, K. Bray, and W. Kollmann. Surface density function in premixed turbulent combustion modeling, similarities between probability density function and flame surface approaches. *Phys. Fluids*, 7(10):2496–2503, 1995.

[118] D. Veynante, J. M. Duclos, and J. Piana. Experimental analysis of flamelet models for premixed turbulent combustion. *Symp. (Int.) Combust.*, 25(1):1249–1256, 1994.

[119] D. Veynante and L. Vervisch. Turbulent combustion modeling. *Prog. Energ. Combust. Sci.*, 28:193–266, 2002.

[120] A. Vincent and M. Meneguzzi. The dynamics of vorticity tubes in homogeneous turbulence. *J. Fluid Mech.*, 258:245–254, 1994.

[121] C. R. Wilke. A viscosity equation for gas mixtures. *J. Chem. Phys.*, 18:517–519, 1950.

[122] F. A. Williams. Turbulent combustion. In *The mathematics of combustion*, pages 97–131. SIAM, 1985.

[123] F. A. Williams. *Combustion Theory*. Westview Press, 2 edition, 1994.

[124] S. Yang, A. Saha, Z. Liu, and C. K. Law. Role of Darrieus–Landau instability in propagation of expanding turbulent flames. *J. Fluid Mech.*, 850:784–802, 2018.

[125] Y. B. Zeldovich, G. I. Barenblatt, V. B. Librovich, and G. M. Makhviladze. *The Mathematical Theory of Combustion and Explosions*. Consultants Bureau, New York, 1985.

[126] T. Zheng, J. You, and Y. Yang. Principal curvatures and area ratio of propagating surfaces in isotropic turbulence. *Phys. Rev. Fluids*, 2(10):103201, 2017.